Ultralight EMI shielding aerogels based on V_2O_5 nanowires

Thesis Submitted to
the University of Kerala for the Award of the Degree of
Doctor of Philosophy in Physics
under the
Faculty of Science

By

Aparna P. N.

Under the guidance of

Dr. K. P. Surendran

Materials Science and Technology Division
CSIR-National Institute for Interdisciplinary
Science and Technology (CSIR-NIIST)

Research Centre, University of Kerala
Thiruvananthapuram-695 019
Kerala, India

2022

DECLARATION

I hereby declare that the Ph.D. thesis entitled "***Ultralight EMI shielding aerogels based on V_2O_5 nanowires***" is an independent work carried out by me at the Materials Science and Technology Division of CSIR-National Institute for Interdisciplinary Science and Technology (NIIST), Thiruvananthapuram, under the supervision of Dr. K. P. Surendran, vouching that there is no plagiarism using the software approved by the UGC/University, and it has not been submitted anywhere else for any other degree, diploma or title.

Aparna P. N.

Thiruvananthapuram

July, 2022

राष्ट्रीय अंतर्विषयी विज्ञान तथा प्रौद्योगिकी संस्थान
NATIONAL INSTITUTE FOR INTERDISCIPLINARY SCIENCE AND TECHNOLOGY
वैज्ञानिक तथा औद्योगिक अनुसंधान परिषद् | Council of Scientific & Industrial Research
औद्योगिक एस्टेट पोस्ट, तिरुवनंतपुरम, भारत - 695 019 | Industrial Estate P.O., Thiruvananthapuram, India – 695 019

CERTIFICATE

This is to certify that the work embodied in the thesis entitled, **"*Ultralight EMI shielding aerogels based on V_2O_5 nanowires*"** has been carried out by **Ms Aparna P. N.** under my supervision at the Materials Science and Technology Division of CSIR-National Institute for Interdisciplinary Science and Technology (NIIST), Thiruvananthapuram, vouching that there is no plagiarism using the software approved by the UGC/University and the same has not been submitted elsewhere for any other degree, diploma or title.

Dr. K. P. Surendran (Supervisor)

Thiruvananthapuram

July, 2022

ACKNOWLEDGMENTS

With great pleasure, I extend my indebtedness and deep sense of gratitude to **Dr. K. P. Surendran**, my thesis supervisor, for suggesting me the research problem. His valuable support, encouragement, and guidance throughout the research period have led to the successful completion of this work. I would like to express my sincere thanks to **Dr. Narayanan Unni**, for his guidance and support during the research work, especially in the initial stage. I am grateful to **Dr. A. Ajayaghosh**, Director, CSIR-NIIST, for providing the facilities for research. I am deeply indebted to Dr. S. Savithri (Head, MSTD, NIIST), Dr. P. Prabhakar Rao, and Dr. K. Harikrishna Bhat, Former Heads, MSTD, NIIST. I would like to express my heartfelt thanks to Dr. E. Bhoje Gowd for his insightful suggestions and creative discussions, which helped me immensely during my work. I would like to thank Dr. Manoj Raama Varma, Dr. Satyajith Shukla, Dr. Senoy Thomas, Dr. U. S. Hareesh, Dr. T. P. D. Rajan, Dr. Saju Pillai and Dr. Sreejith Sanker, for their valuable course work lectures. The support of all the other scientists of NIIST is greatly acknowledged. It is indeed my pleasure to thank Dr. K. S. Sibi, Head, Department of Physics, Kariavattom Campus, University of Kerala, Dr. G. Subodh, former Head, Department of Physics, Kariavattom Campus, University of Kerala, and Dr. V. Biju, Professor, Department of Physics, Kariavattom Campus, University of Kerala, for their timely help and valuable suggestions. I am also grateful to the NIIST administration for extending all the timely help. I would like to acknowledge and express my most profound sense of gratitude to the Kerala State Council for Science, Technology, and Environment (KSCSTE) for providing the research fellowships to carry out this work. Apart from that, I also wish to acknowledge the funding agencies such as DST, CSIR, and ISRO for financial support during the various stages of my research work.

The valuable advice and help from the senior research scholars; Dr. P. Abhilash, Dr. Angel Mary Joseph, Dr. K. S. Dijith, Dr. R. Aiswarya, Dr. D. R. Lekshmi, Dr. Kanakangi S Nair and Dr. Revathi R. are acknowledged with gratitude. I am greatly indebted to my colleagues.; Ms. Bhavya A. S., and Mr. Adarsh Siva, for their love and support. My special thanks to my friends who stood with me during the goods and bads of my research life; Ms. Sabitha Ann Jose, Ms. Roshima K., Ms. Jinu Joji, and Mr. Dileep N.P. I would like to thank all my colleagues and friends at NIIST; especially Mr. Vipin G Krishnan, Mr. Gandu Virat, Ms. Praveena, Mr. Krishanakumar, Ms. Shisina, Ms. Suja, Ms.

Hasna, Ms, Renjana, Ms. Remya, Ms. Sneha, Mr. Anoop, Mr. Alan, Mr. Bineesh, Ms. Aparna S., Ms. Shyamili, Mr. Sumith, Mr. Shafeeq, Ms. B. S. Athira, Mr. T. K. Abhilash, Mr. Harris, and Ms. Shyamini. My heartfelt thanks to Vidya Lalan and Athira for their help during characterization works at Kariavattom Campus.

I am very thankful to my plus-two teacher, C. S. Radhakrishnan, who made physics enjoyable and motivated me towards physics. I would also like to thank my teachers at Sree Krishna College, Guruvayur, and St. Thomas' college, Thrissur, for the learning opportunities they provided. I am incredibly grateful to Dr. K. M. Manu and Dr. Johns Naduvath for paving the way to the field of research.

Words cannot express my gratitude to my parents and sister, Savithri, Narayanan, and Aryadevi, who supported and motivated me in every step of this incredible journey. I owe this thesis to their love and understanding. I would also like to acknowledge the unconditional love and encouragement from my in-laws and all other relatives. A special thanks to Sudha chechi, who took care of our baby, Mizhi, during my lab time. Mizhi, your mere presence made my days better. Finally, Mr. Prasad, here is my heartfelt gratitude for your patience and understanding. Your support during the rough times was a great comfort and relief. How you handled my frustration, cared for our family, and tried to fill happiness is highly appreciated; love you.

Aparna P. N.

CONTENTS

Chapter 1

Chapter 3

Chapter 4

LIST OF TABLES

LIST OF FIGURES

ABBREVIATIONS

1D	One dimensional
2D	Two dimensional
3D	Three dimensional
5G	Fifth generation
A	Absorption
ATR	Attenuated total reflection
BET	Brunauer-Emmett-Teller
BJH	Barrett-Joyner-Halenda
CNF	Cellulose nanofiber
CNT	Carbon nanotubes
CPC	Conductive polymer composites
DC	Direct current
DI	Deionized
E	Electric field
EDS	Energy dispersive X-ray spectroscopy
EM	Electromagnetic
EMC	Electromagnetic compatibility
EMI	Electromagnetic Interference
FESEM	Field emission scanning electron microscope
FTIR	Fourier transform infrared spectroscopy
GA	Graphene aerogel
GO	Graphene oxide
GPS	Global positioning system
g_s	Green index
H	Magnetic field
HRTEM	High-resolution transmission electron microscopy

IoT	Internet of things
LED	Light emitting diode
M	Multiple reflections
MWCNT	Multi-walled carbon nanotube
NW	Nanowire
OA	Oriented attachment
PANI	Polyaniline
PCB	Printed Circuit Board
PVA	Polyvinyl alcohol composite
R	Reflection
RF	Radio frequency
rGO	Reduced graphene oxide
SE	Shielding effectiveness
SE_{Abs}	Absorption shielding effectiveness
SEM	Scanning electron microscopy
SE_{Ref}	Reflection shielding effectiveness
SE_{Total}	Total EMI shielding effectiveness
SSE	Specific shielding effectiveness
TEM	Transmission electron microscopy
TGA	Thermogravimetric analysis
VNA	Vector network analyzer
WAXD	Wide-angle X-ray diffraction
XPS	X-ray Photoelectron Spectroscopy
Z	Impedance

PREFACE

Communication gadgets like smartphones, laptops, WiFi rooters, etc., are ubiquitous today. Electromagnetic (EM) waves generated from the densely packed electronics in these devices can largely interfere with the functioning of electronic devices, often causing pernicious consequences like data losses, information insecurity, and critical system failures. This detrimental phenomenon is called electromagnetic interference (EMI). The harmful effect of EMI also includes health issues for users, ranging from insomnia, headache, fertility problems, and even cancer as well. So, it is imperative to develop efficient electromagnetic shields to solve electromagnetic interference. Although the conventional metallic solutions give excellent shielding, their high density and corrosive nature make them unsuitable for portable devices and avionic applications. Properly designed, low-dense, eco-friendly EMI shields with high absorption shielding are highly preferred for handheld devices. Aerogels, foams, and sponges are feather-light and can effectively attenuate EM radiations through multiple internal reflections inside their pores and interfaces. However, imparting high conductivity and hence good shielding efficiency (SE) in three-dimensional porous structures without compromising mechanical strength is challenging. The present research aims to develop a new class of efficient and green microwave attenuating aerogels through a series of facile and cost-effective strategies. The valuable results of our research are outlined in this thesis, organized into six chapters, with the take-home messages and future directions included in the last chapter.

Chapter 1 presents a general introduction on the basic principles and concerns about EMI and various solutions to mitigate it. Different shielding mechanisms evolved over time, and the necessity of green shields is also highlighted. Further, a detailed literature survey on porous EMI shielding materials, especially microwave absorbing aerogels, is presented. Significant challenges and the possible solutions, including choice of materials, synthesis protocols, etc., are also outlined. This chapter broadly justifies the rationale behind the choice of the doctoral research problem and our solutions to address it systematically.

The first working chapter (**Chapter 2**) describes our efforts to realize 3D nano-architectured carbonized aerogels using the layered oxide V_2O_5. Herein, a simple one-pot hydrothermal preparation protocol is meticulously designed and implemented as a cost-

effective strategy for making robust aerogels. The low dense aerogels with 3 mm thickness have high shielding (>25 dB) in X (8.2-12.4 GHz), Ku (12.4-18 GHz), and K (18-26.5 GHz) bands, with maximum EMI shielding efficiency (EMI SE) reaching 43 dB at 26.5 GHz. Green index (g_s) is found to be >1 in the measured frequency span.

Chapter 3 reports that the realization of conducting polymer composite (CPC) aerogels consists of inorganic V_2O_5 nanowires and polyaniline (PANI), with exceptional EMI shielding performance. The eco-friendly, lightweight aerogels effectively attenuate EMI through multiple internal reflections inside the layered structure of V_2O_5. The structure, morphology, formation of gel, and the EMI shielding properties of V_2O_5- PANI composite aerogel were investigated and discussed in detail. The mesoporous aerogel has a very low density of ~0.02 g/cc with maximum EMI shielding efficiency (EMI SE) of 34 dB in the X band, with an impressive specific shielding efficiency of 1662.2 dB cm^3 g^{-1}. The green index (g_s) is found to be one of the highest so far in literature (~2.91).

With a slight modification of the strategy in chapter 3, a chemically engineered 3-dimensional array of PANI reinforced V_2O_5 aerogels were prepared, as described in **Chapter 4**. Surprisingly, these acid polymerized aerogels showed exceptional shielding efficiency of 68.1 dB in X-band, with steady bandwidth. Even in the K band, a stunning shielding performance with a maximum of 86.1 dB is shown, translated to a record-breaking specific shielding efficiency of 2777.4 dB cm^3/g. These results demonstrate that hierarchically porous 3D architecture realized through a meticulous control of acid polymerization can lead to impressively high shielding performance, even without employing costly metallic, carbonaceous, or MAX phase fillers.

In chapter 2 and 3, the synthesis takes nearly one month to complete and yield good shielding efficiency above 99.9 %. Hence the method was further modified wherein V_2O_5 hydrogel was synthesized via a simple one-pot hydrothermal route, outlined in **Chapter 5**. The V_2O_5 nanowire network constructing the gel was effectively reinforced by cross-linking aniline. The aerogels thus obtained after freeze-drying exhibit excellent shielding performance (71.2 dB), superior specific shielding efficiency (1338.8 dB cm^3/g), and a good green index (1.02). Various characterization tools confirmed the porous structure of the materials and the successful incorporation of polyaniline. Interestingly, V_2O_5-polyaniline aerogels prepared in the acidic medium has high conductivity, ample

mechanical strength, and absorption dominant shielding efficiency in the entire X, Ku, and K band frequency.

Overall, this doctoral thesis has generated significant results that can push the knowledge boundary on ultra-high shielding aerogels for exciting aeronautic applications. **Chapter 6** summarizes the significant findings and conclusions drawn from this research, which also accommodates the scope for future work.

Chapter 1

Electromagnetic interference shielding- An overview

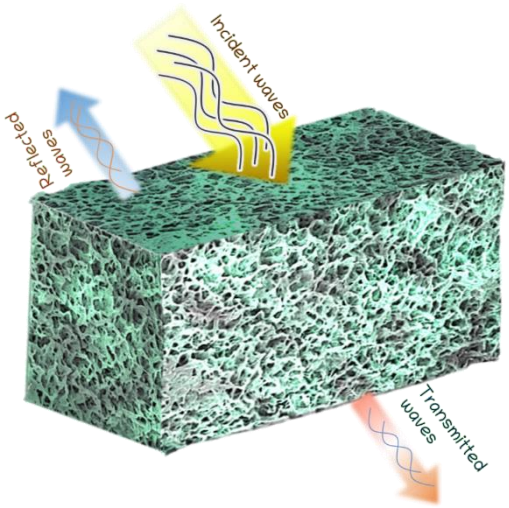

The spurious electromagnetic (EM) waves generated from electronic devices can largely interfere with each other, resulting in electromagnetic interference (EMI) pollution. The chapter outlines the concept and mechanisms of EMI shielding. As the thesis mainly focuses on lightweight shields, a brief introduction to the available porous shielding structures is discussed. The objectives of the thesis and the rationale behind the choice of materials are also outlined.

1.1 Introduction

Inventions and innovations have transformed our lives dramatically. Modern man is perpetually surrounded by communication gadgets, including mobile phones, laptops, global positioning systems (GPS), Bluetooth, Wi-Fi routers, etc. Densely packed electronics in these devices generate spurious electromagnetic (EM) waves. These harmful EM waves often detrimentally interfere with the functioning of electronic devices, resulting in issues like data losses, information insecurity, and critical system failures (Pandey *et al.*, 2019). This disruptive phenomenon caused by the EM waves is called electromagnetic interference (Agnihotri *et al.*, 2015; H. Zhao *et al.*, 2017). The blooming growth of fifth-generation (5G) communication technology enables data transfer to occur at breathtaking speeds with extended connectivity. When more devices are involved in communication, more is EMI pollution.

Besides data interference and loss, electromagnetic interference can also cause health issues ranging from insomnia, headache, fertility problems, and even cancer as well (Lewczuk *et al.*, 2014). Earlier, EMI pollution was mainly confined to specific customer groups like offices, banks, and R&D institutes. However, after the mobile phone revolution in the new millennium, electronic devices became handy and ubiquitous, resulting in EMI proliferating almost everywhere. Recently, some sociological issues of the present world also catalyzed electromagnetic pollution. For example, the recent outbreak of the Covid-19 pandemic further catalyzed the wide use of communication gadgets at an unprecedented speed. In this scenario, the concerns about EMI also increased to higher levels. EMI shielding is the best way to protect a specific biological or electronic system from undesirable radiations. So, it is imperative to develop efficient electromagnetic shields to solve the menaces of electromagnetic interference.

1.2 EMI- Why the concern?

As hinted, EMI's consequences range from minor communication interruptions to potential system failures, security breaches, and lethal accidents. Some of the significant reasons behind electromagnetic interference becoming a global concern are as follows (Tong, 2008):

- The potential risks of EMI arise from a multitude of sources such as cellular telephones, TV broadcasting, digital assistance, wireless communication devices, etc. The burgeoning demand for smaller and smart gadgets added more sources as well as susceptors of EMI. Also, the wide use of digital circuitries generates more EMI than analog ones.
- Dense packing as part of miniaturization brought short-distance interference between various components on board.
- Manufacturers try to improve devices' reliability and information security that demand EMI elimination.
- Medical equipment experiences more exposure to EMI and is thus prone to detrimental impacts on its user.
- Military security systems need camouflaging from enemies' EM waves.
- People are more aware of the environmental pollution and health risks caused by EMI.

Electromagnetic radiation is generated along with an alternating current and radiated in the vicinity of the source. The distance up to which the effect of this electromagnetic field is felt depends on conducting parts associated with the EM source (Paperman *et al.*, 2004). Any system that has electronic circuitry is a source as well as a victim of EMI. A prevalent example of EM interference from daily life is that use of cellular phones is prohibited in petrol pumps because of the possible interference with the readings of pump meters. Similar worries exist in aviation and flight control systems. Electromagnetic interference from mobile phones and laptops used by passengers, with aircraft systems can cause rumblings in communication and anomalies in navigation. In a classic example, the root cause of five crashes of US Army Black Hawk Helicopters in 1987 was reported as a consequence of the coupling of high-intensity radio frequency energy to helicopters' fly-by-wire system (Majid, 2018). At times, EMI is even dubbed as a 'silent killer' in the medical sector. Sophisticated medical devices can resist EMI only up to a certain level, beyond which they become abnormal or non-functional. The safety of patients who depend on life-supporting electronic implants like pacemakers was always a primary concern. Electronic circuits of cardiac pacemakers are prone to EMI, and their usual mode of operation will alter when the magnitude of the surrounding electromagnetic field exceeds immunity level of the device (Tan & Hinberg, 2004).

1.3 EMI- concepts and mechanisms

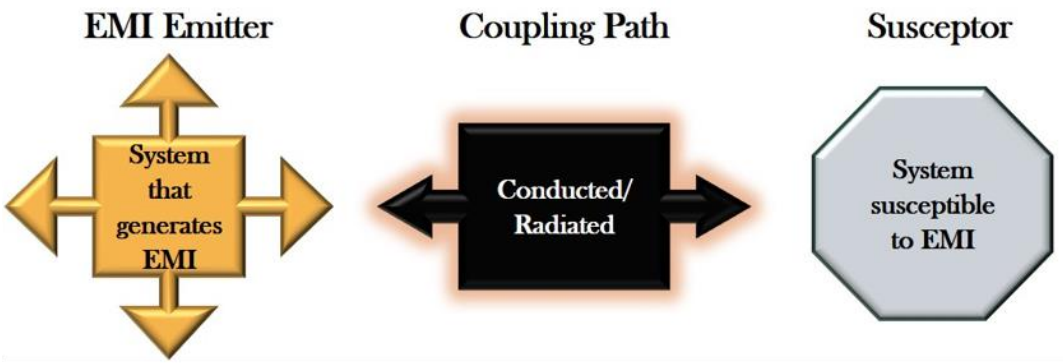

*Figure **1.1** Coupling modes of EMI*

Electromagnetic energy from the source travels in all directions and causes interference issues to another system (susceptor) through either radiated or conducted pathways. That means three interactive elements (as shown in figure 1.1) are involved in an EMI problem; (1) an emitter or source (culprit) of EM waves of particular energy, (2) a susceptor that is vulnerable to this EM energy, and (3) a coupling path between these two components; source and the susceptor. The conducted EMI is propagating *via* connecting wires and signal cables. In radiated mode, undesired EM emission from a source is transferred through the space and reaches any of the surrounding devices without any connectors. The intensity of the radiated EMI depends on the source, distance to susceptors, and the media surrounding the source. To limit the issues brought about by EMI, international electromagnetic compatibility (EMC) standards were imposed by nations (Tong, 2008). Electromagnetic compatibility is the ability of an electronic system to operate satisfactorily within an intended electromagnetic environment without any damage due to EMI. Another aspect of EMC is that a device is expected to work without interfering with other equipment. In general, EMI can be controlled by suppressing EMI emissions from the source, redirecting the electromagnetic radiations, and boosting the susceptor immunity (Tong, 2008). There are limitations in minimizing EM energy from the source beyond a level, and for the protection of portable devices and aircraft, it is practically impossible to control the emissions from various sources. Diverting the EM waves in random directions generates secondary interference issues causing environmental pollution. As the redirected waves can reach the source detectors, the method of path modification can not be used in military aircraft and security systems. In summary, using EMI shields to protect desired

devices from unwanted EM waves is the most desirable way to secure sensitive information and reduce radiation bourne health hazards.

The shielding performance of a material is generally quantified by a parameter called shielding effectiveness (SE). EMI SE tells the degree of attenuation caused by the insertion of a shield at a specific area and is the ratio of the EM energies at a given point, with and without the shield. The ability of a material to block microwaves is usually expressed in terms of decibel loss (dB), defined as:

$$\mathrm{SE} = 20 \log \left(\frac{\text{Incident EM intensity}}{\text{Outgoing EM intensity}} \right) \tag{1.1}$$

At a specified frequency, shielding effectiveness varies with the shield thickness, the distance between the source, and the shielding material.

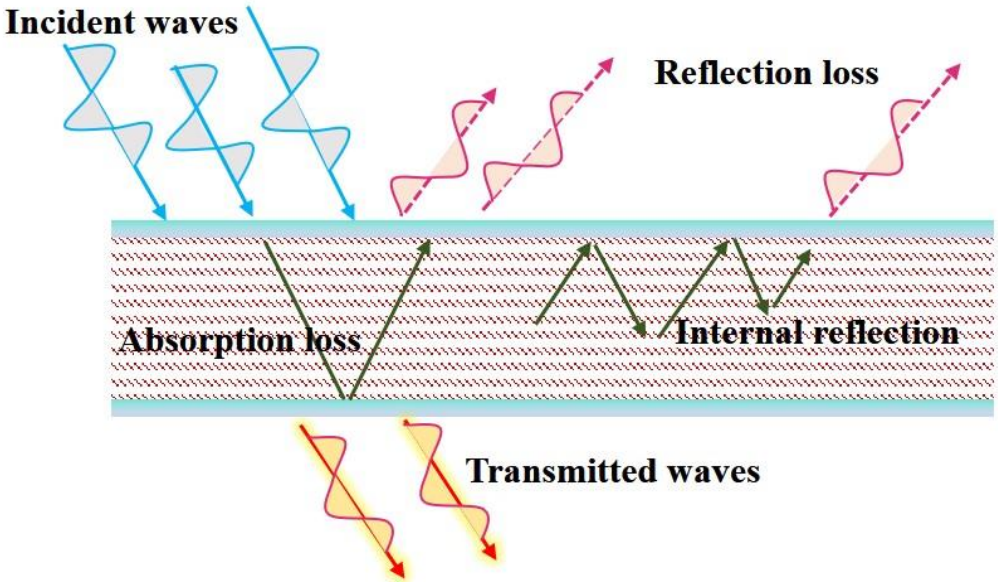

*Figure **1.2** Shielding mechanisms in a material*

When an EM wave is incident on a surface, it is partially reflected, the material absorbs a little, and the rest is transmitted. According to Schelkunoff's theory, a shield reduces the transmission by enhancing absorption, reflection, and multiple reflections within the shielding material (Figure 1.2) (Gonschorek & Vick, 2010). The total EMI shielding efficiency is the sum of all the three attenuating mechanisms; absorption (A), reflection (R), and multiple reflections (M).

$$SE = R + A + M \quad (1.2)$$

Reflection occurs when EM waves travel through two media with different impedances. Hence, it is related to the relative impedance mismatch between the medium of the incident wave and the shielding (Celozzi *et al*., 2008; Tong, 2008). The wave impedance (Z) can be expressed as the ratio of the magnitude of the electric field (E) to the magnetic field (H). Here, Z (=E/H) in a medium depends on the nature of the wave source and the distance from the source. The wave impedance equals the impedance of the medium in the far-field. For air, Z_0= 377Ω. Shields with good conductivity show strong reflection. This is due to the interaction of mobile charge carriers (electrons or holes) in the shield with the incoming EM waves. As reflection is the primary shielding mechanism in metals and homogeneous conductive shields, these materials lead to secondary EM wave pollution. The second important mechanism, absorption, is associated with the thickness and physical characteristics of the shield. The intensity of radiations exponentially declines during the propagation of EM waves through the shield. Skin depth (δ) is the distance through which the initial electric field drops to (1/e) of the incident strength (Tong, 2008).

$$\delta = \frac{1}{\sqrt{\pi f \mu \sigma}} \quad (1.3)$$

where f is the wave frequency, μ is the magnetic permeability, and σ is the electrical conductivity. Attenuation by absorption happens through dielectric loss, ohmic loss, and magnetic loss. The third shielding mechanism is the repeated internal reflections within the shielding material. Multiple reflections are essential for low-frequency measurements and samples thinner than their skin depth (Tong, 2008). For thick and porous samples, instead of transmitting out, the energy of internally reflected signals will be absorbed within the material, leading to a substantial reduction in EMI.

We all know that electromagnetic waves consist of periodically changing electric (E) and magnetic (H) fields perpendicular to each other and the direction of propagation. Let us see how a shielding material behaves in these two fields.

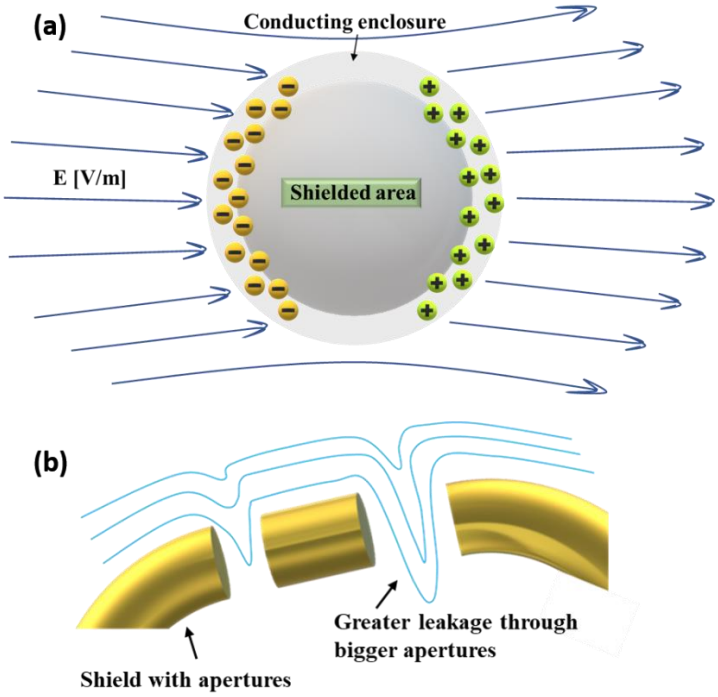

*Figure **1.3 (a)** Shielding provided by a spherical conducting shell placed in an electric field and (**b**) effect of apertures on shielding.*

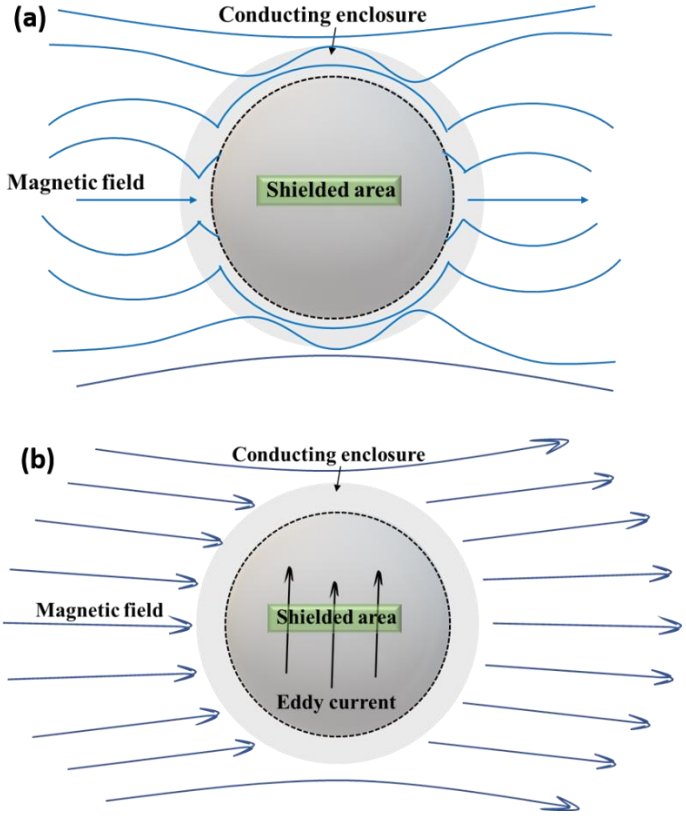

*Figure **1.4** (**a**) Shielding by a spherical magnet shell with good permeability and (**b**) shielding by a thin conductive shell with mild permeability and good conductivity.*

Consider a conductive enclosure placed in an electric field. The external field will cause electric charges to align along the conductor's surface. The field developed by these charges opposes the original field inside the enclosure. The electromagnetic current prefers the least resistance path around the exterior surface of the conductive compartment. So, anything placed inside the chamber will be perfectly shielded from the electric field (see figure 1.3a). An important point is to be noted here; if there is any gap or hole in the conductor, the EM waves will certainly leak through it and limit the shielding effectiveness (figure 1.3b) (Tong, 2008).

Now, let us use a soft magnetic material with high permeability or a thin conductive shield with mild permeability to shield our system from a magnetic field. In the first case, the magnetic enclosure offers a low-reluctance path, and the incoming magnetic field will remain in the magnetic layer. The magnetic field will eventually get attenuated inside the sheath if it has sufficient thickness (see figure 1.4a). On the other hand, an alternating magnetic field will induce Eddy currents in the low permeable, conductive shield, generating an H-field in the opposite direction of the applied field and thus attenuating the external magnetic field (see figure 1.4b) (Tong, 2008). This kind of shielding does not require expensive and thick magnetic materials. However, conductive shielding is ineffective for low-frequency magnetic fields.

We will briefly elaborate on the impacts of various parameters on EMI shielding.

1.3.1 Distance between source and shield

Based on the distance between the EMI source and the shield, r, radiative space is divided into near- and far-field regions (Tong, 2008). The $r < \lambda/2\pi$ (near field) region is predominantly magnetic if the source has high current and low voltage, and the near field is electric field dominant if the source has high voltage and low current. In the magnetic-dominated region, the magnetic field decays at a rate of $(1/r^3)$, and the electric field diminishes at a rate of $(1/r^2)$. The variation is vice versa in the case of an electrically dominated field. As the distance from the source increases, $r > \lambda/2\pi$ (far-field), both the electric and magnetic fields attenuate at the same rate (1/r), becoming plane waves (Koo *et al.*, 2021).

1.3.2 Electrical conductivity

Electrical conductivity directly determines the EMI shielding capability of any material. Higher the conductivity, the higher the EMI SE. Higher electrical conductivity promotes a reflection-dominant EMI shielding mechanism. High conductivity and high permeability are also beneficial for increasing absorption loss (A) (Tong, 2008).

$$A = 131\, t\sqrt{f\mu\sigma} \tag{1.4}$$

where f is frequency, t is thickness, μ is permeability, and σ is the electrical conductivity of shielding material.

1.3.3 Frequency of the incident waves

As the shield's impedance increases with increasing frequency, the reflection shielding efficiency decreases with frequency. On the other hand, absorption shielding efficiency is directly proportional to the frequency, as evident from equation 1.4.

1.3.4 Thickness of shield

Absorption shielding increases with the thickness of the shield as thickness elongates the propagation path of EM waves. Reflection shielding, in contrast, is independent of thickness.

1.3.5 Dielectric losses

The electromagnetic absorption is directly related to the material's complex permittivity, i.e., $\varepsilon_r = \varepsilon' - j\varepsilon''$. The real part ($\varepsilon'$) accounts for the capacitive energy storage potential, and the imaginary part (ε'') is related to the energy dissipation. The dielectric loss consists of ohmic loss, resonance loss, dielectric relaxation loss, etc. (Koo *et al*., 2021).

1.3.5.1 Ohmic loss

Conductance current generated due to the applied electric field in a lossy dielectric dissipates incident EM energy in the form of heat. This is called ohmic loss and is related to its electrical conductivity (Tong, 2008).

1.3.5.2 Dielectric relaxation loss

Under an applied electromagnetic field, a material's dipoles are polarized and will orient according to the field, resulting in relaxation loss. Polarization can be in any form, say, electronic, ionic, thermal ion, or interfacial polarization. Ionic and electronic polarization occurs at high frequencies, $\sim 10^{14}$ to 10^{15} Hz. Dipolar, interfacial, and thermal ion displacement polarizations occur at radio to microwave frequencies (Huo *et al*., 2009).

1.3.5.3 Resonance loss

An applied electric field vibrates the atoms, electrons, or ions inside the shielding material. Resonance loss induced by this motion usually takes place in the infrared to the ultraviolet frequency range (Huo *et al*., 2009).

1.3.6 Magnetic losses

Similar to dielectric loss, magnetic losses are represented by the complex permeability ($\mu' - j\mu''$). Magnetic loss covers the following losses:

1.3.6.1 Eddy current loss

Eddy current is the current induced in a magnetic material when subjected to a varying magnetic field. They dissipate the incoming EM field in the form of heat. The Eddy current loss depends on the material's thickness, permeability, and electrical conductivity. Morphology, grain size, surface roughness, domain orientation, etc., also affect Eddy current loss. The loss is higher for thicker and conducting samples (Dhawan *et al*., 2011).

1.3.6.2 Magnetic hysteresis loss

Rotation of magnetic moment and irreversible domain movement cause magnetic hysteresis loss, and it depends strongly on the magnetic properties of the shielding material (Dhawan *et al*., 2011).

1.3.6.3 Residual loss

Magnetic losses caused by the factors like thermal fluctuation, ferromagnetic and domain wall resonance, etc., are called residual loss (Koo *et al*., 2021).

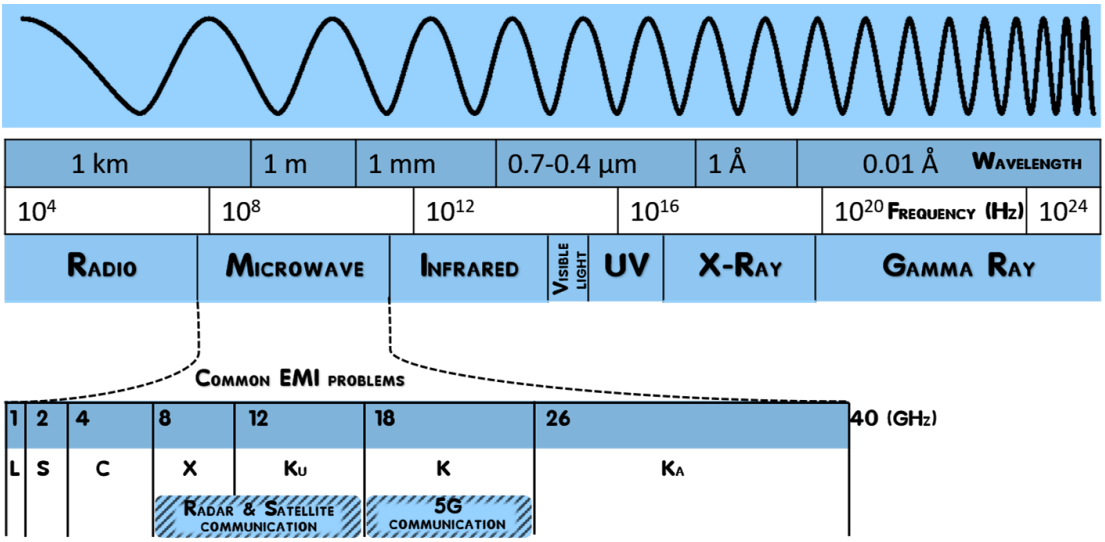

*Figure **1.5** Electromagnetic spectrum showing an overview of EMI susceptible frequency ranges. The present thesis examines EMI problems in X, Ku, and K bands; the applications in these bands are highlighted.*

In general, issues of EMI arise anywhere in the electromagnetic spectrum. The electromagnetic spectrum has been increasingly inhabited by countless devices and services (figure 1.5). The radio and microwave frequency range (100 kHz to 40 GHz) is considered as the typical shielding range because most problems happen there. In the present thesis, we concentrate mainly on shielding waves in three bands of the microwave frequency range, namely the X (8-12 GHz), Ku (12-18 GHz), and K (18-27 GHz) bands. The X and Ku band is utilized for radar, satellite communication, and wireless computer networks. K band is proposed for the future 5G communications (Lalan & Ganesanpotti, 2022).

1.4 Measurement of EMI shielding effectiveness

There are a variety of techniques used to characterize the shielding ability of a material. Most of the standard methods necessitate tailor-designed samples with specific shapes and dimensions. Each measurement test produces a performance parameter that can be converted to shielding efficiency in decibels using proper calculation. Usually, the values obtained by different methods are hard to correlate; hence, each result needs to be analyzed individually. Some of the standard techniques are briefly outlined here:

1. Open field/ Free space method
2. Shielded box method

3. Shielded room method
4. Coaxial transmission line method

1.4.1 Open field method

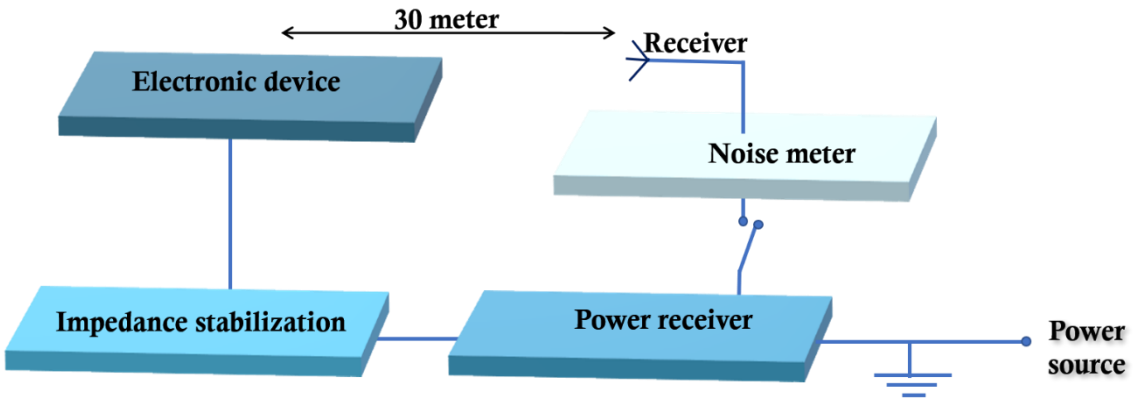

*Figure **1.6** Open field measurement setup*

The open-field method measures the EMI SE of a complete electronic assembly by assessing the radiated emission from the whole product (Geetha *et al*., 2009). Hence, the method does not give details about the performance of a specific material. The measurement setup is shown in figure 1.6. A receiver antenna placed at a 30 m distance from the device records the transmission intensity.

1.4.2 Shielded box method

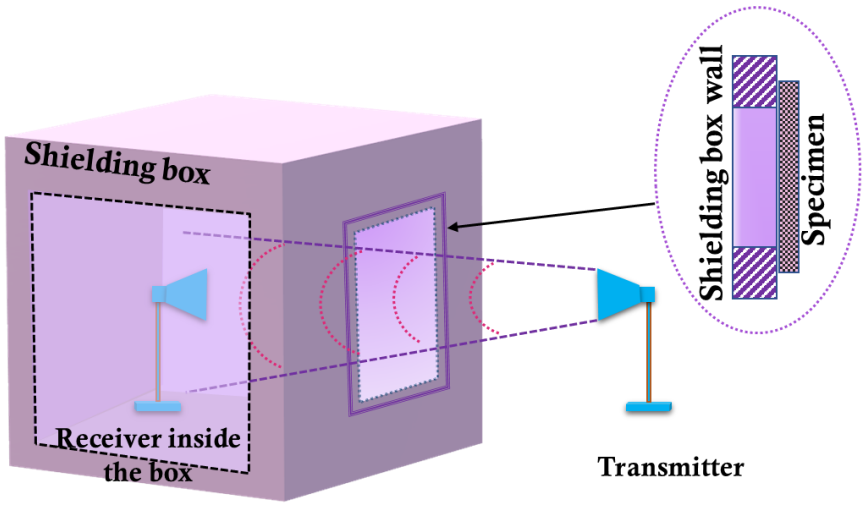

*Figure **1.7** Shielded box method of EMI SE measurement*

The shielded box method compares the EMI SE of different shielding specimens. The test setup is illustrated in figure 1.7. A receiver antenna is fitted inside a shielded enclosure, usually a metal box. The test sample seals the small opening in the box. The receiver antenna records the transmitted signal strength from an outside antenna before and after placing the test sample (Geetha *et al*., 2009; Tong, 2008). The measurement is limited to a frequency of 500 MHz only. Issues like difficulty in getting adequate electrical contact between test specimens and the enclosure, dependence of attenuation on the antenna's position, and internal reflections inside the box make the results less reproducible.

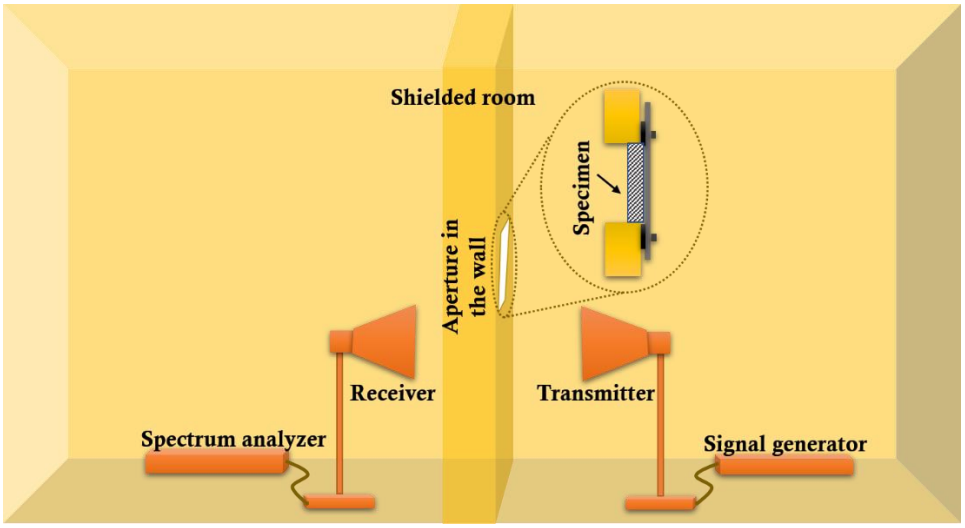

*Figure **1.8** Shielded room method*

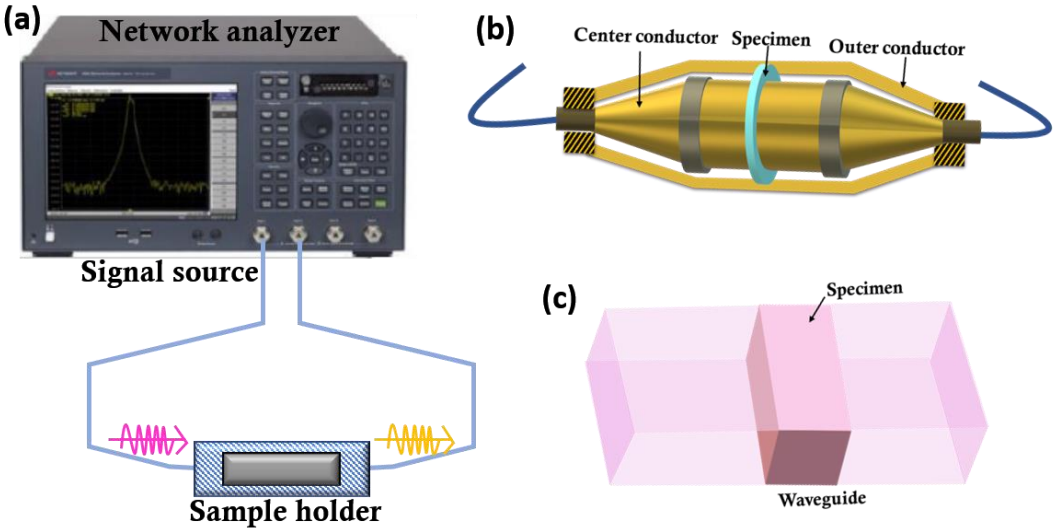

*Figure **1.9** (**a**) Experimental set up of transmission line method, sample holders of (**b**) coaxial line, and (**c**) waveguide methods*

1.4.3 Shielded room method

The shielded room method is an improved version of the box method; in particular, the measurement frequency range is significantly improved. In this method, all the components for the measurement are isolated from each other in separate rooms. The transmitter and receiver antennas are placed at a fixed separation distance in two rooms with a common wall (Singh *et al*., 2018). The test specimen can be placed in the aperture of the common wall, as shown in figure 1.8. The receiver records the transmitted power with and without mounting the sample, and the difference is taken as the shielding effectiveness of the test sample.

1.4.4 Transmission line method

The transmission line method is the popular method used for shielding measurement in most laboratories. The main advantages of this method are the high reproducibility and better insight into the detailed shielding mechanism by resolving data into reflected, absorbed, and transmitted components (Geetha *et al*., 2009; Singh *et al*., 2018). The experimental setup consists of a vector network analyzer, transmitting and receiving coaxial cables, and a metal sample holder, as shown in figure 1.9a. There are two configurations for transmission line testing, *viz.* (i) coaxial line and (ii) waveguide methods. The coaxial line method introduces a toroid-shaped sample between the inner and outer conductors (figure 1.9b). A single sample can be used to measure in a broad frequency range. For example, a sample with inner and outer diameters of 3 mm and 7 mm is used to measure EMI SE in a frequency range of 0.5 to 18 GHz. On the other hand, a precisely machined sample in the shape of a rectangular block is used in the waveguide method; hence, the sample preparation is comparatively easy (figure 1.10c). However, the dimensions of the sample vary with the waveguide used for the measurement, which in turn depends on the measurement frequency range. For example, in the X band frequency range, the sample dimension is 22.8 mm × 10.1 mm; the Ku band is 15.79 mm × 7.89 mm, while the K band is 10.67 mm × 4.32. So, several waveguides are needed to measure at wide-frequency ranges. The present thesis uses the rectangular waveguide method for all the EMI SE measurements.

*Figure **1.10** Vector network analyzer coupled X band transmission waveguide.*

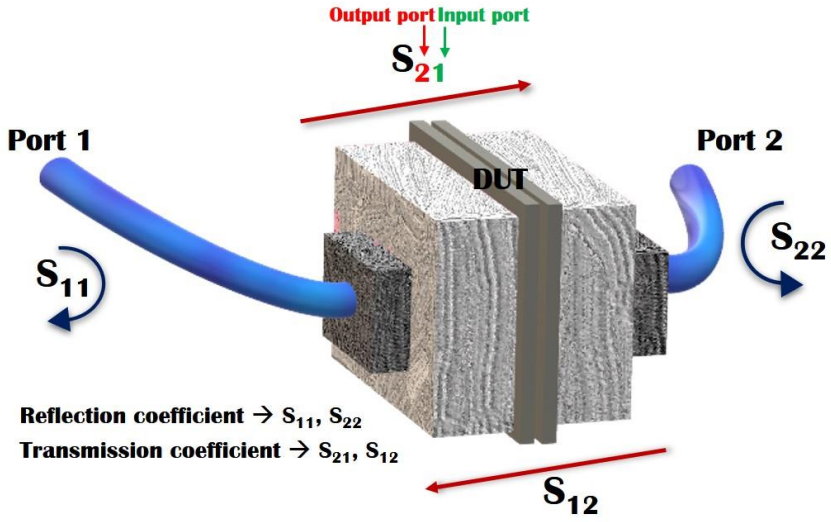

*Figure **1.11** Vector network analyzer coupled X band transmission waveguide.*

1.4.5 Measurement using the vector network analyzer

Among several techniques used to estimate the EMI shielding of materials, the rectangular transmission waveguide technique is ideal for machinable bulk materials like aerogels (Batrakov *et al.*, 2016; Geetha *et al.*, 2009; Tong, 2008). In the present investigation, the electromagnetic characterization of all the aerogels was performed in the X band (8.2-12.4 GHz), Ku (12.4-18 GHz), and K band (18-26.5 GHz) of the microwave

frequency range. For this, the samples were machined into a rectangular block to fit into the waveguide's sample holder coupled to a vector network analyzer (VNA). Agilent E5071C Network analyzer, Santa Clara, CA, USA, was employed for X and Ku band measurements, and a Keysight PNA-L network analyzer N5234B was used for the K band. A photograph of the X band measurement setup is shown in figure 1.10. Appropriate calibrations were done before the measurement to eliminate errors due to directivity, source match, load match, isolation, etc. Before measurement, the aerogel samples were carefully machined with the exact size of the slot cross-section of the waveguide. The inner slot dimensions of the waveguide sample holders are 22.8 mm × 10.1 mm for X, 15.79 mm × 7.89 mm for Ku, and 10.67 mm × 4.32 mm for K bands.

Once the aerogel was loaded inside the sample holder, the scattering parameters (S-parameters) of reflection coefficient data S_{11}, $S_{22,}$ and transmission data S_{21} and S_{12} were recorded from the vector network analyzer. The format of the S-parameter notation is as follows: In S_{ab}, 'S' represents S-parameter, 'a' and 'b' stands for response port number and stimulus port number, respectively. Figure 1.11 gives a good idea about the notation of S-parameters. Using the apparent scattering parameters, the absorption shielding effectiveness (SE_{Abs}), reflection shielding effectiveness (SE_{Ref}), and the total EMI shielding effectiveness (SE_{Total} = SE_{Abs}+ SE_{Ref}) were calculated using Equations (1.5) and (1.6) (Dijith *et al*., 2018).

$$SE_{Abs}(dB) = 10\log\left(\frac{1-{S_{11}}^2}{{S_{21}}^2}\right) \quad (1.5)$$

$$SE_{Ref}(dB) = 10\log\left(\frac{1}{1-{S_{11}}^2}\right) \quad (1.6)$$

1.5 Applications of light EMI shields

As electrical device use increases, the competition in the electronics industry mandates radiation immunity and smooth functioning of devices in any electromagnetic environment. Electromagnetic interference malfunction electronics on the ground as well as to aircrafts flying 30,000 feet up in the sky. Legal requirements also demand proper shielding of devices from printed circuit board (PCB) level. EMI problems are usually addressed in the early developmental stages of new products. However in some places, external shielding is an easy solution in which the whole equipment and associated cables

are shielded. In such cases, we need light and effective shields with adequate strength and long service life, which is broadly addressed in the present thesis. Uniquely designed EMI shielding gaskets are used in healthcare systems, communication devices, military equipment, automotive, etc. (Bass, 2017; Cybershield, 2017). Modern times demand the gadgets to be as light as possible, which necessitates more R&D efforts on porous shields and other conductive aerogel structures. Given below are some of the vital applications of lightweight EMI shielding solutions.

1.5.1 Shielding in avionics

The consequences of electromagnetic interference in avionic equipment include deteriorated performance or malfunction. Effective EMI management is very important in an avionic system with many frequency-generating systems (digital circuits, switching power supplies, and frequency synthesizers etc.) which control the power levels and signal rates. Unintentional EMI disruptions generated from mobile phones, laptops, or any other electronic gadgets can cause problems in the important and sensitive parts like digital communications and GPS. Intentional threats from jamming equipment, electronic counter measures, and other electronic weapons can even lead to potential failure of the entire system. As mentioned earlier, basically, there are two approaches; PCB level shielding by proper designing and use of shielding enclosures. To combat EMI, various line replaceable units should be completely surrounded by EMI shielding material. Here, the weight of the shield, susceptibility to corrosion, and wear are crucial. The shields should be as light as possible for such requirements.

1.5.2 Shielding in mobile electronics

The critical way to estimate the usefulness of an electronic equipment to interfere with aircraft communication systems is to test the electronic equipment under test at all modes of operation during take-off, flying and landing. For android mobile phone users of modern times, this procedure is impractical. So the practical solutions involve the following methods (Vanguard Products, 2022).

(i) Design improvement by introducing PCB level shielding: The use of shielding cans and covers will serve this purpose, but their weight has to be reduced and hence non-metallic solutions have to be developed.

(ii) Employing EMI shielding gaskets: Conductive elastomers with Ag or Ni plated fillers are used for such applications. Lightweight foam based gaskets including conductive fabric, wire mesh on soft foam substrates etc. are also popular choices employed in consumer electronics.

1.5.3 Shielding in defence systems

EMI shielding has become a necessity in defence vehicles & equipments including armoured trucks, tanks, drones, helicopters, and control panels, since it enables protection to the sensitive equipments against signal interference from within and outside. Some of the main systems where lightweight EMI protection is solicited are as follows;

Battle Tanks: EMI shields fitted in the body of tanks act as a physical barrier between the static energy from outside and the delicate electrical and electronic components inside.

Helicopters: EMI shielding in defence flight systems including helicopters helps in avoiding the emergency shutdown of engines and scrambling of delicate military digital instruments.

Drones: A lightweight EMI shielding system can isolate communication gadgets from fault-making signals (emitting and receiving).

Armoured Car: Military armoured cars create an electromagnetic environment around them automobile due to the electronic circuits in them. Proper EMI shielding systems helps to prevent this menace.

Control Panel: Unwanted signal interference affects the accuracy, reliability and performance of military base control systems. Suitable EMI shielding manages communication delays prevents device misreads, avoid equipment damages.

Mainly EMI shielding gaskets and coatings are used for the shielding purpose. In any sector, low-dense materials are preferred over heavy metallic enclosures. Coatings are effective in this direction as they will not much contribute to the overall weight of a system. However, they are vulnerable to delamination and scratching, which limits their applications. Hence, industries are searching for cost-effective and light EMI solutions like foams, thin films, and porous composites.

1.6 Shielding materials and methods

Conventionally, metals with high electrical conductivity, such as silver, aluminium, and copper, were used for effective EMI shielding. Abundant free electrons in these materials promote shielding with high reflection loss, which is one of the main disadvantages. Reflected EM waves again cause secondary pollution in the environment. Although metals provide excellent SE, their bulky-corrosive nature and poor acid-alkali resistance retards their shielding performance over time and delimit their applications (H. Zhao *et al.*, 2017). Specific spacecraft, aircraft, and portable electronics require the shields to be as light as possible. Hence, ceramics and polymer composite gradually took over the metallic shields. However, most of the mechanically stable and processable polymers are of low loss and non-conductive and hence are unsuitable for shielding applications. The efficient strategies adopted in order to make conductive composites are (i) incorporating conducive fillers like metallic nanostructures, carbon nanotubes, graphene, carbon fibers, etc., (ii) introducing conductive capping such as conductive ink coating, and (iii) using intrinsically conducting polymers. Several studies thus focus on developing lightweight shields with conductive polymer composites (CPCs). For example, polymer composite prepared with expanded graphite and linear low-density polyethylene particles exhibited 52.4 dB shielding effectiveness (B. Wei *et al*., 2021). Poly (lactic acid)/carbon nanotubes (CNTs) composites were found to be promising for shielding applications with shielding of 31.1 dB. Recently, Wang *et al* used Pickering emulsion templating and melt blending techniques to nicely disperse CNTs in the polymer matrix (Y. Wang *et al.,* 2022). In addition to weight reduction and chemical stability, the machinability and design flexibility of CPCs are attractive, too (Y. Li *et al.*, 2019). CPCs loaded with various noble metallic micro/nanoparticles, conducting carbon fillers (reduced graphene oxide, carbon nanotubes, foams, powders, and fibers), and magnetic nanoparticles exhibit promising shielding efficiency (Lalan *et al*., 2019).

Since EMI shielding effectiveness is proportional to the electrical conductivity, higher EMI SE demands a higher weight percentage of the conducting filler. However, the conductive addition, in most cases, negatively affects the cost-effectiveness and processability of the shielding material. Also, higher filler loading may reduce the specific shielding value due to increased density and reduction in porosity. Literature reports

suggest that CPCs with multiple structures as porous three-dimensional conductive networks could achieve high shielding values at low filler loadings (W. Yu *et al*., 2018).

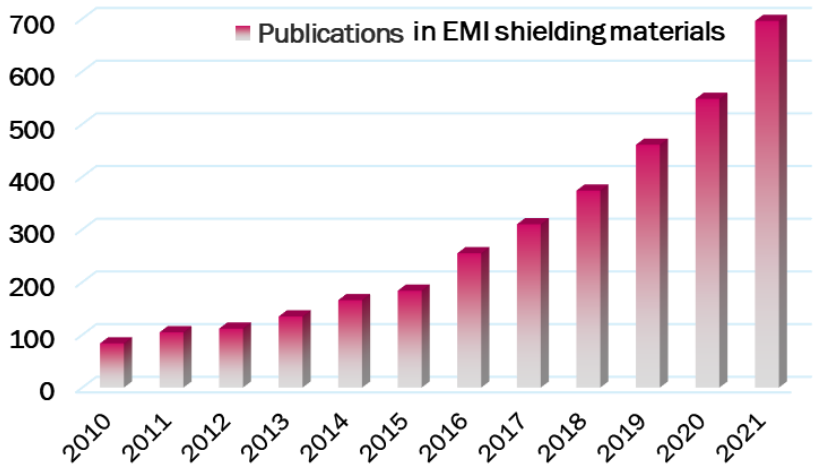

*Figure **1.12** The growth of publications in the domain of EMI shielding in the last 11 years* (Clarivate, 2022)

Another concern is that high conductivity causes strong secondary reflection, which harms the environment and living systems (X. Wang *et al.*, 2019). Thus, the shields should ideally show an absorption dominant shielding mechanism in addition to good EMI SE. EMI shields with superior absorption shielding efficiency can be conveniently realized using ultra-porous structures, which provide more room for multiple internal reflections, thereby absorbing more EM energy. So far, considerable studies have happened related to health hazards of EMI and various means of material manifestations for EM wave attenuation in the desired frequency range (Abbasi *et al*., 2019; Lewczuk *et al*., 2014; Y. Wang & Jing, 2005). Figure 1.12 shows the number of publications in the past decade (2010 onwards), mainly on EMI shielding, which depicts the uptrend of literature each year (as per the data available in Clarivate web of science, till 20-04-2022). Since the prime emphasis of the present doctoral research is centered on light shields, let us restrict the following discussion to porous shields alone.

In the case of lightweight shields, specific shielding effectiveness (SSE), i.e., the shielding effectiveness divided by the mass density of shielding material, is also an important parameter. High SSE is accomplished in intelligently designed porous aerogels and foams (Sreedeviamma Dijith *et al.*, 2019). Porous shields have peculiar advantages by virtue of their absorption dominant shielding mechanism. Primarily, low secondary

reflections make them green and environment friendly. Secondly, the meso-, micro-, and macroporous structure and the shield's bulk electrical/magnetic properties can contribute significantly to their overall shielding efficiency (Singh *et al.*, 2018; Zeng *et al.*, 2018). In fact, the broad scope of porosity engineering makes it easier to tune the shielding properties for specific lightweight applications. Finally, the tailor-made porous architecture significantly reduces the weight and cost, and multiple internal reflections inside the pores help increase absorption shielding over reflection shielding (Zeng *et al.*, 2018). Therefore, developing novel synthesis protocols to generate tailor-made porosity yet retain mechanical strength has become an area of hot research in composites. Several innovative approaches are reported to create porous architectures. Some of the usual methods for the construction of porous composites are listed as follows:

1.6.1 Template method

This method uses materials such as polyurethane sponge, nickel foam, anodized alumina, etc. as templates within which the fillers are either incorporated or grown by immersion/ chemical reactions (Z. Chen *et al*., 2013a; Y.-J. Wan *et al*., 2018). The method offers simple preparation conditions and high flexibility. Also, biomaterials derived from wood, cotton, tissue, paper, etc., are excellent templates with the advantages of easy availability, biodegradability, and non-toxicity. However, the preparation involves detailed pre-treatments and high-temperature heat-treatment to improve the performance.

1.6.2 Drying method

The drying process is crucial in the preparation of conductive networks inside a porous material, especially in the case of aerogels. Ambient pressure drying, freeze-drying, and supercritical drying are the widely used drying strategies, among which freeze-drying is the most popular (L. Wang *et al*., 2021). In the freeze-drying method, the solvent in the precursor suspension is frozen to ice crystals and then sublimated at a low temperature and pressure. Pores replace the ice crystals, and the pore size largely depends on the freezing conditions. The beauty of this method lies in the easiness of producing a well-maintained porous network, the same as in the original dispersion.

1.6.3 Solvothermal/ Hydrothermal method

Solvothermal and hydrothermal methods form a 3D conductive network under high temperature and pressure inside an autoclave. Different nanostructures can be synthesized by this simple and easy method (Huangfu *et al*., 2019b; X. Yang *et al*., 2020). The difference between hydrothermal and solvothermal methods is that in the latter, the processing temperature should be above the critical temperature of the solvent, which is non-aqueous. Therefore the pressure is relatively higher than hydrothermal (Gadea *et al*., 2018).

1.6.4 Foaming method

In the foaming method, foaming agents such as phenylsulfonyl hydrazine, azodicarbonamide, etc., introduce gaseous pores inside a continuous matrix. Reports suggest that the cellular structure in foams would help multiple reflections, decline the dielectric constant, and bring electrical conductivity to match with good shielding properties (L. Wang *et al*., 2021). Despite the mechanical property provided by the foam, some of the polymer foams, like expanded polystyrene foams, possess lower porosity and higher density and hence may not be apt for making light EMI shield. 3D printing is another blooming strategy for realizing well-designed foam structures.

1.7 Porous shielding solutions

Figure 1.13 gives an idea about the emergent role of porous composites in the EMI shielding domain in the past five years. The pie chart clearly indicates that only <30% of the total publications report porous materials (Data taken from Clarivate web of science on 20-04-2022). So, there is vast space for exploring more, among which aerogels are ultralight porous materials containing high volume gas phase fractions (H.-D. Huang *et al*., 2015). In particular, conductive aerogels have a wide range of potential applications in fuel cells, batteries, chemical sensors, and supercapacitors (H. B. Zhao *et al*., 2016). Aerogels are much explored among various porous materials due to their low density, open porous structure, and high internal surface area. They thus can be excellent candidates for lightweight EMI shields. Next, we will discuss some of the porous shielding materials reported so far and the major challenges faced in this area.

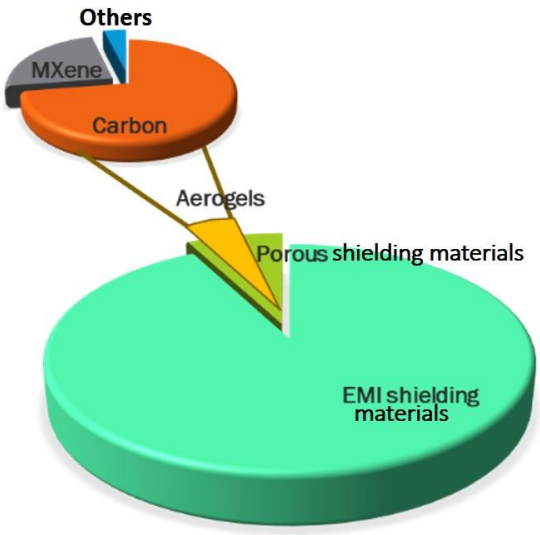

*Figure **1.13** Pie diagram showing the percentage of publications related to various porous shielding solutions in the last five years* (Clarivate, 2022).

1.7.1 Carbon-based aerogels

Various functional materials of different nano-morphologies have been integrated into the porous skeletons of aerogels to improve the microwave attenuation of the latter. Mostly 2D materials like graphene, MXene, etc., and other carbonaceous fillers (like CNT, graphite powder, etc.) are used to make high shielding composite gels. Carbon-based aerogel composites are highly competitive as excellent shields because of their potential chemical and electrical properties. For instance, Li *et al.* fabricated cellulose nanofibril/reduced graphene oxide (rGO) carbon aerogel with ultra-low density (~0.0058 g/cm^3) and high EMI SE (~33 dB) (M. Li *et al.,* 2021). The method they adopted for the preparation involved unidirectional freezing using a copper plate and liquid nitrogen, followed by freeze-drying. Then the aerogels were carbonized under a nitrogen atmosphere at 700 ºC. Another carbon-based cellulose fiber/graphene aerogel with a density as low as 2.83 mg/cm^3 exhibited ~47.8 dB EMI shielding effectiveness (Y.-J. Wan *et al.*, 2017). The aerogel's remarkable mechanical resilience and excellent cycling stability make it ideal for light shielding applications. The shielding performance of rGO@ high-density polyethylene aerogel coated natural rubber latex foam is only moderate, with 24 dB at 4 mm thickness (Y. Sun *et al.,* 2021). However, this work's striking features like superoleophilicity, superhydrophobicity, and high electrical conductivity make the foams attractive as multifunctional material. Hu *et al.* presented a similar multifunctional aerogel film made of carbon nanotubes, aramid nanofibers, and fluorocarbon resin (Hu *et al.*, 2020).

The hydrophobic aerogel film with superior electrical conductivity (230 S/m) and huge specific surface area (232.8 m^2/g) exhibited excellent shielding effectiveness (SE) of 54.4 dB at a meager thickness of 568 μm. Aramid fibers offer proper mechanical strength, and fluorocarbon provides water-repellent features and thus long-term stability. Though the fabrication process was a bit laborious and time-consuming, its self-cleaning property and Joule heating performance made this aerogel unique and promising for multifunctional applications.

Yet another interesting aerogel composition is the one derived from Ni foam/graphene oxide (GO)/polyvinyl alcohol composite (PVA), which has a low density of 189 mg/cm^3 that showed 87 dB SE at 2 mm thickness (D. Sen Li *et al.*, 2022). Its good compression strength (172.2 kPa) and hydrophobicity are also noticeable. There, GO and PVA was mixed, heat-treated, poured over the Ni foam, and freeze-dried to obtain the hybrid gels. A gentle coating with 1H,1H,2H,2H-Perfluorodecyltriethoxysilane gave the aerogel water repellent nature. In 2021, epoxy/Ag nanowire/thermally annealed graphene aerogel composites with a high compressive strength of 173.54 MPa was reported, showing a SE of 84.01 dB in X-band with an absorption-dominate shielding mechanism (Gao *et al.*, 2021). The preparation involved hydrothermal reduction, vacuum-assisted impregnation, and thermal annealing. Lightweight carbon aerogels fabricated by Liao *et al*, showed a promising shielding capacity of 36.75 dB only at a thickness of 4 mm (Liao *et al.*, 2021). However, impressive elasticity, excellent compressive strain, and specific shielding effectiveness/thickness reaching a high value of 73500 dB cm^3/g make the aerogel promising. Due to its exceptional mechanical performance and strain/pressure sensitivity, the material was also found to be a potential candidate for a wearable pressure sensor. The preparation of this multifunctional shield uses pickering emulsion gel strategy, and it involves several steps like mixing, emulsification, gelation, freeze-drying, etc. This aerogel is also claimed to be suitable for light EMI shielding applications and flexible pressure sensing.

All the above-reported light materials showed excellent shielding performance. In principle, a porous conductive shield of a specific thickness can improve its SE value by raising the conductivity of the filler or by increasing the amount of conducting filler (Zeng *et al.*, 2016). However, higher filler loading will rupture the conductive network inside the porous structure and increase the overall density. It should be noted that porous

architectures employing carbonaceous fillers can improve the conductivity but result in a high dielectric loss in the polymer matrix, thereby detrimentally affecting their EM wave attenuation. Further, due to their poor dispersion, carbonaceous gels demand complex synthetic procedures that solicit functionalization, auxiliary treatment, and purification (Kumar *et al.,* 2020).

1.7.2 MXene-based aerogels

Let us cherry-pick a few promising aerogels involving layered 2D materials outside the carbon family, say MXene-based aerogels. $Ti_3C_2T_x$ MXene/aramid nanofiber (ANF) anisotropic aerogel prepared by Du *et al,* displayed outstanding conductivity reaching up to 854.9 S/m and a corresponding EMI SE of 65.5 dB (Du *et al.*, 2022). Superelastic and highly compressible aerogels also exhibit flame retardant properties. Cellulose nanofiber (CNF)/ammonium polyphosphate/$Ti_3C_2T_x$ composite aerogels prepared by simple solution mixing of exfoliated MXene and freeze-drying demonstrated average shielding effectiveness of 55 dB with an 8 mm thick sample (Y. Zhang *et al*., 2021). High specific shielding effectiveness/thickness was ~5729 dB cm^2/g, and good electrical conductivity of 12 S/m was also reported. The peculiarity with this aerogel is that, unlike other MXene composites, it had an absorption dominant shielding mechanism and was fire-resistant too. MXene aerogel/wood-derived porous carbon composites prepared by Gu's group had almost the same shielding performance (71.3 dB) at a density of 0.197 g/cm^3 (C. B. Li *et al.,* 2020). In this work, the natural wood template carbonized at high temperature displayed hydrophobic nature along with a high EMI SE of 61.3 dB. The introduction of MXene into the ordered honeycomb-like wooden skeleton acted as a "mortar-brick" structure, improving the shielding further. The composite also showed flame retardant and thermal insulation properties. Mechanically tough and robust MXene/aramid nanofibers hybrid aerogel fabricated by Lu *et al.*, shown ~56.8 dB EMI SE at 1.9 mm thickness and SSE/thickness reached 3645.7 dB cm^2/g in X band (Lu *et al.,* 2021). In that work, aramid nanofibers provide reversible compressibility and oxidation resistance while the MXene boosts the electrical conductivity. Apart from good conduction loss, multiple reflections in the microporous structure and high dielectric loss are pronounceable. $Ti_3C_2T_x$/carbon nanotube hybrid aerogel developed through bidirectional freeze-drying displayed shielding effectiveness of 103.9 dB (3 mm thickness) in the X band (Sambyal *et al.,* 2019). The hybrid gel has a high electrical conductivity of 9.43 S/cm and possesses better mechanical

strength than the pristine MXene aerogel. Silicone-coated MXene/ cellulose nanofiber aerogel film displayed an EMI SE of 39.4 dB (Xin *et al.,* 2021). The aerogel possessed hydrophobicity due to the silicon coating, excellent photothermal performances, and Joule heating property. Here, the procedure was relatively more straightforward and took less time. The outstanding specific shielding effectiveness per thickness (17586 dB cm^2/g) and EMI SE (54.3 dB at 26 µm) of $Ti_3C_2T_x$/calcium alginate aerogel films is one of the best results reported by Prof. Canhui Lu's group, among the reported works (Z. Zhou *et al.,* 2019). Their synthesis protocol was tricky where $Ti_3C_2T_x$/sodium alginate mixture was air sprayed to $CaCl_2$, and after vacuum-assisted infiltration and freeze drying, ultra-thin $Ti_3C_2T_x$/calcium alginate aerogel films were formed. Very recently, Li *et al,* prepared lignocellulose nanofibril/gelatin/MXene composite aerogel with a maximum EMI SE of 62.1 dB for a 2 mm thick sample (Y. Li *et al.,* 2022). The excellent fire-retardancy properties of these gels make them unique. The synthesis method involves chemical pre-treatment of eucalyptus powders and then mechanical defibration. Thus-formed phosphated lignocellulose nanofibrils was combined with chemically delaminated $Ti_3C_2T_x$ (MXene) and gelatine taken in fixed ratios and finally the mixture was freeze-dried to obtain the final aerogels.

From the preceding discussion, it is evident that it is impossible to question the central position of MXenes in EMI shielding. However, the difficulties with MXene composites include complex procedures, relatively high cost of the materials, harsh acid environment involved in the careful etching process of MAX phases, etc.

1.7.3 Other interesting aerogels

An intelligent attempt by Liu *et al.* is really noteworthy (X. Liu *et al*., 2021). They synthesized low-dense, wood-derived carbon aerogels (54 mg/cm^3) that could switch from non-shielding to shielding material upon simple compression. Here, the initial procedure of wood sponge preparation involves laborious chemical and thermal pre-treatments. Then, these sponges were carbonized with CNT and graphene oxide. Nevertheless, the aerogel with 6.9 mm thickness showed only a meager EMI SE <2 dB. However, when the gel was subjected to 75% strain, the carbon nanoparticle connectivity established good electrical conductivity and thus improved shielding performance to a maximum of 27.6 dB in the X band. Hence, the aerogel acts as an on/off switchable EMI shield.

Graphene aerogel prepared by an intermediate hydrogel compression step also shows tuneable EMI shielding properties (C. B. Li *et al.,* 2020). With compression to 5% and 40% of the original height of aerogel, EMI shielding values were 43.29 dB and 31.44 dB, respectively, at 2.5 mm thickness. Upon compression, the cellular microstructure of hydrogel was changed to a layered configuration, and the aerogel's density was also increased. As both these morphologies well support multiple reflections and shielding, Li *et al.* propose that a more significant number of rGO layers and uniform microstructure due to compressive strain might be the reason for improved EM wave attenuation.

Another wood-derived nanocomposite material, MXene@Wood aerogel with 0.108 g/cm^3 density, possessed anisotropic EMI shielding property with a maximum SE of 72 dB at parallel growth direction (Zhu *et al.,* 2021). Many researchers focus on combining electrically conducting and magnetic components together to improve shielding capacity. Also, the presence of magnetic material offers good impedance match and thereby reduces secondary reflection pollution. In a similar attempt, Chen *et al.* fabricated absorption-dominant cellulose/reduced graphene oxide /Fe_3O_4 aerogels exhibiting ~52.4 dB shielding effectiveness with 2 mm thickness (Y. Chen *et al.,* 2020).

Noticeable is the fact that, although these materials show excellent EMI shielding properties, the construction of such lightweight composites involves complex synthesis steps with various chemicals that disgorge a considerable amount of hazardous waste to the environment.

1.8 Motivation and objectives

The inference from the above brief literature survey given in section 1.7 clearly points out that developing ultra-porous architecture with good electrical conductivity and thus superior EMI SE while maintaining low density is highly challenging. Some ambitious advances have been made on carbonaceous and MXene-based gels. Yet, developing a cost-effective, lightweight, green, and efficient EMI shielding aerogel devoid of carbonaceous fillers (like CNT, graphene, graphite, etc.) and MXene is still challenging.

Hence, in the present thesis work, we are trying to explore light, green, and promising shields using suitably modified layered inorganic oxide material through simple and affordable strategies. We are focusing on aerogel-based shields to ensure high

absorption and low density. One of the relatively cheaper layered oxide materials, V_2O_5, was qualified as the principal filler component of the aerogels.

1.9 The choice of V_2O_5

The nanostructured transition metal oxide V_2O_5 has gained remarkable attention in various fields such as gas sensors, lithium-ion batteries, supercapacitors actuators, and electrochromic devices due to their peculiar properties (K. Chen *et al.,* 2021; Dhoundiyal *et al.,* 2021; Purushothaman *et al.,* 2017). These properties include layered structure, non-toxicity, low-cost and easy synthesis, abundant resources, high charging capacity, long cycle life, high energy density, good conductivity, and multivalent oxidation states (Jiang *et al.,* 2019; Purushothaman *et al.,* 2017; W. Sun *et al.,* 2018; N. Wang *et al.,* 2015). For example, hydrated vanadium pentoxide ($V_2O_5.nH_2O$) exhibits fine intercalation characteristics owing to its layered texture and ion-exchange abilities. Several materials, including polymers, are intercalated into the lamellar structure of a hydrated V_2O_5 and studied for photoactive, organic dye removal, and supercapacitor applications (Powders *et al.,* 2016; K. Zhou *et al.,* 2018). Nevertheless, this fabulous property of V_2O_5 remains under-explored in the field of EMI shielding. Only a few reports are found in the literature presenting V_2O_5-based microwave absorbers. CdSe/V_2O_5 core-shell quantum dots with reduced graphene oxide nanocomposite had average shielding effectiveness of 38 dB for a 1 mm thick sample (Singh *et al.,* 2019). It is reported that hydrated vanadium pentoxide exhibits semiconducting properties due to small polaron hopping of unpaired electrons between the V^{4+} and V^{5+} sites. Hence, V_2O_5 alone cannot provide sufficient shielding due to poor electrical conductivity. But the expanded interlayer spacing with a transition metal ion in the high oxidation state can accommodate other conducting structures in between these layers and improve the conductivity. Depending on the oxidation-reduction potentials of the reactants involved, layer reduction occurs. Further, increase in the percentage of V^{4+} sites result in more charge carriers in the inorganic layers and hence it is expected to significantly increase the conductivity and change the magnetic properties. So, by intercalating suitable materials into stacked layers, we can combine high electrical conductivity with the high redox activity of a transition metal oxide and synergistically enhance the overall electrical properties. Here we will establish strategies to accomplish good electrical conductivity and thus promising shielding effectiveness in V_2O_5-based composite aerogels.

Chapter 2

Carbonized V_2O_5 Aerogels with Excellent Green EMI Shielding

- A novel, ultralight aerogel was prepared by simple hydrothermal carbonization of V_2O_5 nanowires.
- The low-dense aerogels exhibit high shielding efficiency (SE) in X, Ku, and K bands with a maximum EMI SE of 43.24 dB at 26.5 GHz.
- Exceptional specific shielding efficiency of 5147.6 dB cm^2/g is achieved in the K band.
- Aerogels possess a high green index of 1.58.

2.1 Introduction

Being lightweight, conductive, and corrosion resistant, EMI shields using carbonaceous materials, including carbon nanotubes (CNTs), carbon fibers, graphene, and reduced graphene oxide composites, are actively investigated. However, a burning issue associated with highly conducting shielding materials is that they generate a kind of pollution through secondary reflections that damage the surrounding environment. So, modern times demand 'greener' shielding materials. A green shield can be defined as an excellent EM wave attenuator with practically no or shallow reflection (X. Wang *et al*., 2019). They are expected to have a good impedance match with incident waves and possess absorption dominant shielding mechanism with broad bandwidth (D. Zhang *et al*., 2019).

Porous structures like foams, aerogels, and sponges are apt solutions as efficient microwave absorbers. While preserving the low density, the numerous pores on them help EM wave to attenuate by providing enormous specific surface area for multi-reflections (Puthiyedath Narayanan *et al*., 2021). Carbon-based aerogels are promising shielding materials since they are constructed by a unique three-dimensional network of conductive carbon (Liang *et al*., 2019). Recently Yu *et al*. fabricated anisotropic polyimide/graphene composite aerogels by unidirectional freezing, lyophilization, and thermal imidization. The composite aerogels exhibited excellent EMI SE of 26.1−28.8 dB in the X band, and the specific shielding value ranged between 1373− 1518 dB·cm^2/g (Z. Yu et al., 2020a). In another attempt, low dense carbon aerogel films derived from aramid nanofiber through blade-coating, solvent-exchange, freeze-drying, and subsequent pyrolysis under high temperature showed excellent shielding performance of 41.4 dB (B. Zhou *et al*., 2021).

Literature survey suggests that, despite holding fairly good shielding performance, the majority of the carbonaceous gels have their synthesis involves either expensive chemical precursors or needs a laborious synthesis procedure. Hence, making a good shielding porous structure through a facile and cost-saving method will be fascinating. In 2015, Li *et al*. suggested that carbon-like aerogels could be synthesized by hydrothermal carbonization followed by pyrolysis of sugarcane (Y. Q. Li *et al*., 2015). They had a maximum EMI SE of 51.0 dB in the X band with a 10 mm thick sample. However, they displayed an inappropriate variance in shielding efficiency in the measured frequency

range. This chapter presents a carbonized V_2O_5 composite aerogel made through a facile hydrothermal route with appreciable shielding efficiency and broad bandwidth.

Hydrothermal carbonization of saccharides is a well-established procedure to produce different carbonaceous structures for numerous applications like fluorescence emission, drug delivery, adsorbents, porous ceramics, and catalysis (X. Sun & Li, 2004; Z. C. Yang *et al*., 2011). The size and shape of carbon structures are tuned for specific applications. This is possible by varying the hydrothermal conditions such as reaction time, reactant concentration, and reaction temperature. Several articles have already reported that hybrid carbon composites with beautiful nanoarchitectures can be prepared by hydrothermal carbonization of sugars in the presence of inorganic salts. Zhang *et al*. succeeded in converting $(NH_4)_2V_3O_8$/carbon composites to porous V_2O_5 nanoparticles through a one-pot hydrothermal route using D-glucose as carbon source (Y. Zhang *et al*., 2017). The porous V_2O_5 nanoparticles with a BET surface area of 10.6 m^2/g displayed excellent electrochemical properties. High surface area is a primary need for a 'green shield' to increase the EM wave absorption. Also, the charge transport inside the material will be smoother if a one-dimensional V_2O_5 nanowire network is established within a porous composite instead of one with nanoparticles.

In the present work, our primary goal is to develop a robust aerogel having a highly connected, three-dimensional conductive network and good surface area with V_2O_5. Herein, we put forward a facile hydrothermal synthetic route to make an EMI shielding aerogel using carbonized V_2O_5 nanowire architecture using a cheap carbon source, glucose. Chemical structure, microstructure, and EMI properties were investigated in detail, and a simple shielding mechanism is also proposed.

2.2 Experimental

2.2.1 Materials

Ammonium metavanadate (99%) was purchased from Sigma-Aldrich Co. USA. Hydrochloric acid (HCl 37%) and D-Glucose anhydrous were obtained from Merck Life Science Private Limited, Mumbai, and NICE chemicals Private Limited, Kerala, respectively. All the chemicals were used as received without any further purification.

2.2.2 Synthesis of carbonized V_2O_5 aerogels

In this work, carbonized V_2O_5 hydrogels were fabricated through a simple one-step hydrothermal method. First, the V_2O_5 nanowire dispersion was prepared following a reported procedure (K. Zhou *et al*., 2018). A few drops of deionized (DI) water were added into ammonium metavanadate taken in a mortar, and ground well. The resulted paste was oven-dried at 110 ºC. About 1g of this ground powder was then mixed with 10 mL of 1 M HCl with rigorous stirring. Afterward, 10 mL of DI water was added as the suspension became red. After sedimentation, the resulting red precipitate was dispersed in hot water (80−90 °C), and the supernatant was removed. The dispersed red solution was vigorously stirred, and the top solution was removed; the process was repeated until a uniform dispersion was achieved. 0.2 g dextrose was mixed with 30 mL of thus prepared vanadium dispersion. The mixture was transferred to a Teflon-lined stainless-steel autoclave and kept at 140 °C for 24 h. The resulting hydrogel was washed using DI water and freeze-dried for 24 h to obtain carbonized vanadium aerogels. The aerogel product thus obtained is coded hereafter as CVO. For the sake of comparison, pure vanadium nanostructures without carbon were also prepared by the same procedure, and shielding performance was investigated (coded as VO). A schematic diagram of the preparation method is shown in figure 2.1a.

2.2.3 Characterization

The hydrogels were freeze-dried at -110ºC by Scanvac Cool Safe Pro 110-4, M/s. Labogene, Denmark. Fourier transform infrared spectroscopy (FTIR) was performed to compare the chemical structure of the pure and composite aerogels on a Perkin Elmer Series FT-IR spectrum-2 instrument using the ATR (Attenuated Total Reflectance) method. Raman spectra (confocal Raman microscope α-300R WITec, Inc., Germany) and wide-angle X-ray diffractogram (WAXD, XEUSS SAXS/WAXS system using a Genixmicro-source from Xenocs operated at 50 kV and 0.6 mA) were recorded to confirm the formation of composites. X-ray photoelectron spectroscopy (XPS, PHI 500 Versa Probe 2 with Al Kα radiation) was used to evaluate the surface chemical composition of the aerogels. Scanning electron microscopy (SEM, JEOL- JSM 5600LV) and high-resolution transmission electron microscopy (HRTEM, FEI Tecnai G2 30S-TWIN) observed the microstructure and morphologies FEI Co., Hillsboro, OR, USA). Thermogravimetric analysis (TGA) was

done by using STA 7300, Hitachi, Japan. For this, the samples were heated from 25ºC to 650ºC at a rate of 10ºC/min in the air atmosphere. The Brunauer–Emmett–Teller (BET) surface area and pore size were measured after degassing the samples at 150ºC for 12 hours, using a nitrogen adsorption-desorption isotherm (Gemini 2375, Micromeritics, Norcross, USA). The pore size distributions of the aerogels were measured using the Barrett–Joyner–Halenda (BJH) method. The DC conductivity of the samples was measured using the four-probe method using Keithley 2450 source meter. A Keysight PNA-L N5234B network analyzer was used in the X, Ku, and K bands to investigate the EMI shielding performance of the aerogels. The samples were precisely machined into a rectangular shape with dimensions 22.28 mm × 10.1 mm in X, 15.79 mm × 7.89 mm in Ku, and 10.67 mm × 4.32 mm in K band. Samples with a thickness of 3 mm were inserted one after one into a sample holder connected between the waveguide flanges of a network analyzer. The shielding efficiency was calculated by the scattering parameters (S-parameters, S_{11}, S_{12}, S_{21}, and S_{22}) obtained from the vector network analyzer.

2.3 Results and discussion

The crystal structure of the samples was investigated by wide-angle X-ray diffraction (WAXD), and their diffractograms are shown in figure 2.1b. Only a few Bragg reflections are visible in the WAXD spectrum, pointing to the quasi-crystalline nature of the samples. The peaks of the V_2O_5 precursor seem to be a mix of two phases; say, (001) at 8.9º corresponds to layered V_2O_5 and (110), (301), and (011) at 26.3º, 30.7º, and 32.1º matches with the orthorhombic phase of hydrated vanadium pentoxide (Kundu *et al*., 2017; Q. Wei *et al*., 2015). Partial reduction of vanadium during hydrothermal treatment might be responsible for the mixed phases (Ronquillo *et al*., 2016). Anyway, the significant part of reflections belongs to the orthorhombic phase. As reported in earlier publications, carbonization ends up in a little more amorphous material (Y. Zhang *et al*., 2017). The symmetry of spectra of VO and CVO aerogels indicates that the layered structure of V_2O_5 is well maintained even after composite formation.

Raman spectrum of aerogels was taken at room temperature in the wavenumber range of 100-2000 cm^{-1}(figure 2.1c). The peaks in CVO composite gel and VO aerogel are identical, and the spectrum is symmetric with the reported Raman modes for V_2O_5 nH_2O (Abd-Alghafour *et al*., 2020; Londoño-Calderón *et al*., 2010). The dominant peak at 142

cm^{-1} corresponds to the V-O-V chain. The two peaks at 284 and 408 cm^{-1} are associated with the bending vibration of the V=O bonds, and 991 cm^{-1} is assigned to the V=O stretching vibrations (Londoño-Calderón *et al*., 2010). The peaks located at 484 and 685 cm^{-1} are assigned to V-O-V bending and stretching modes, respectively (Abd-alghafour *et al*., 2016).

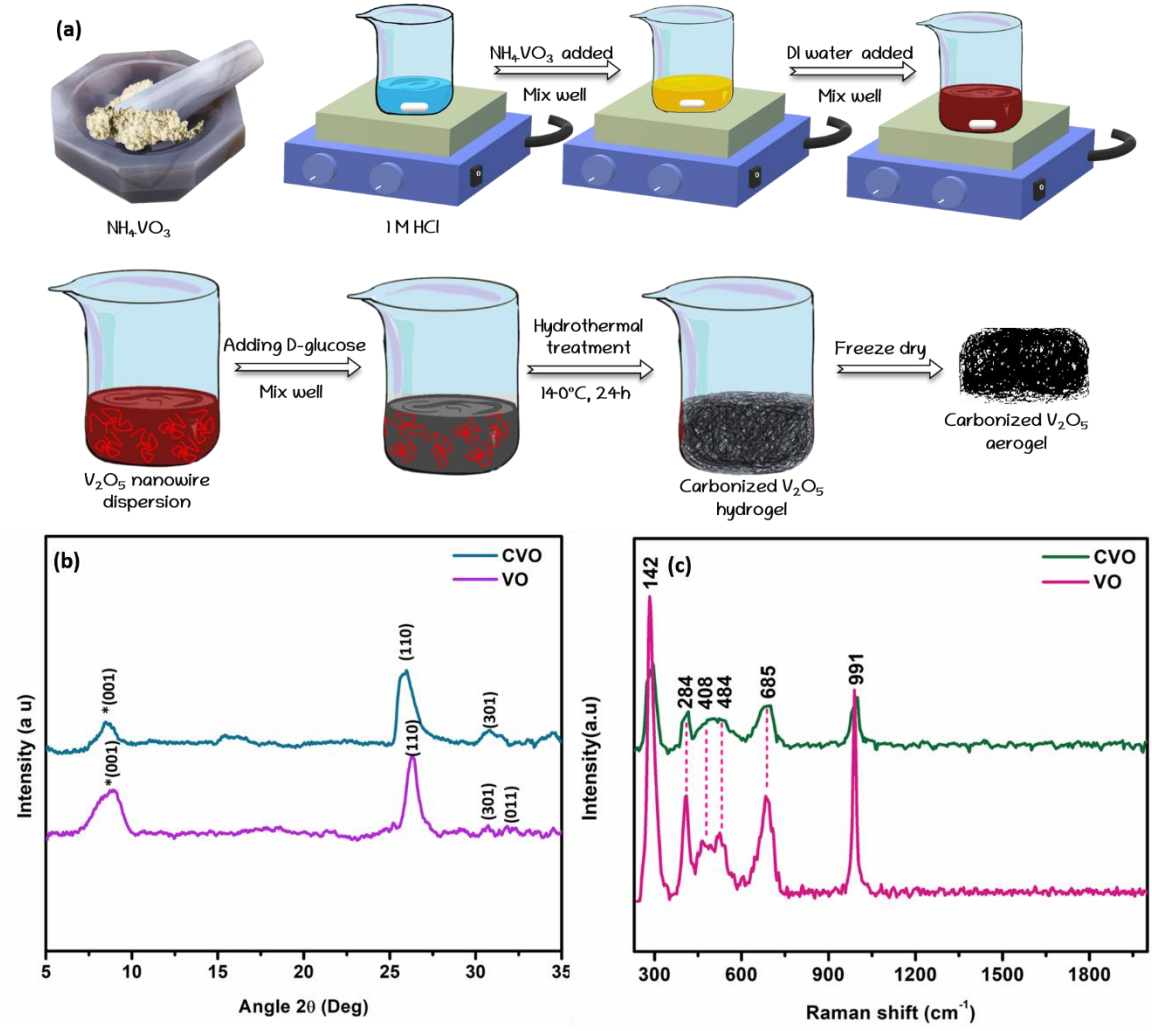

Figure ***2.1*** *(**a**)Schematic illustration of the synthesis of carbonized V_2O_5 aerogel, (**b**) WAXD pattern, and (**c**) Raman spectra of pristine V_2O_5 and carbonized V_2O_5 aerogels*

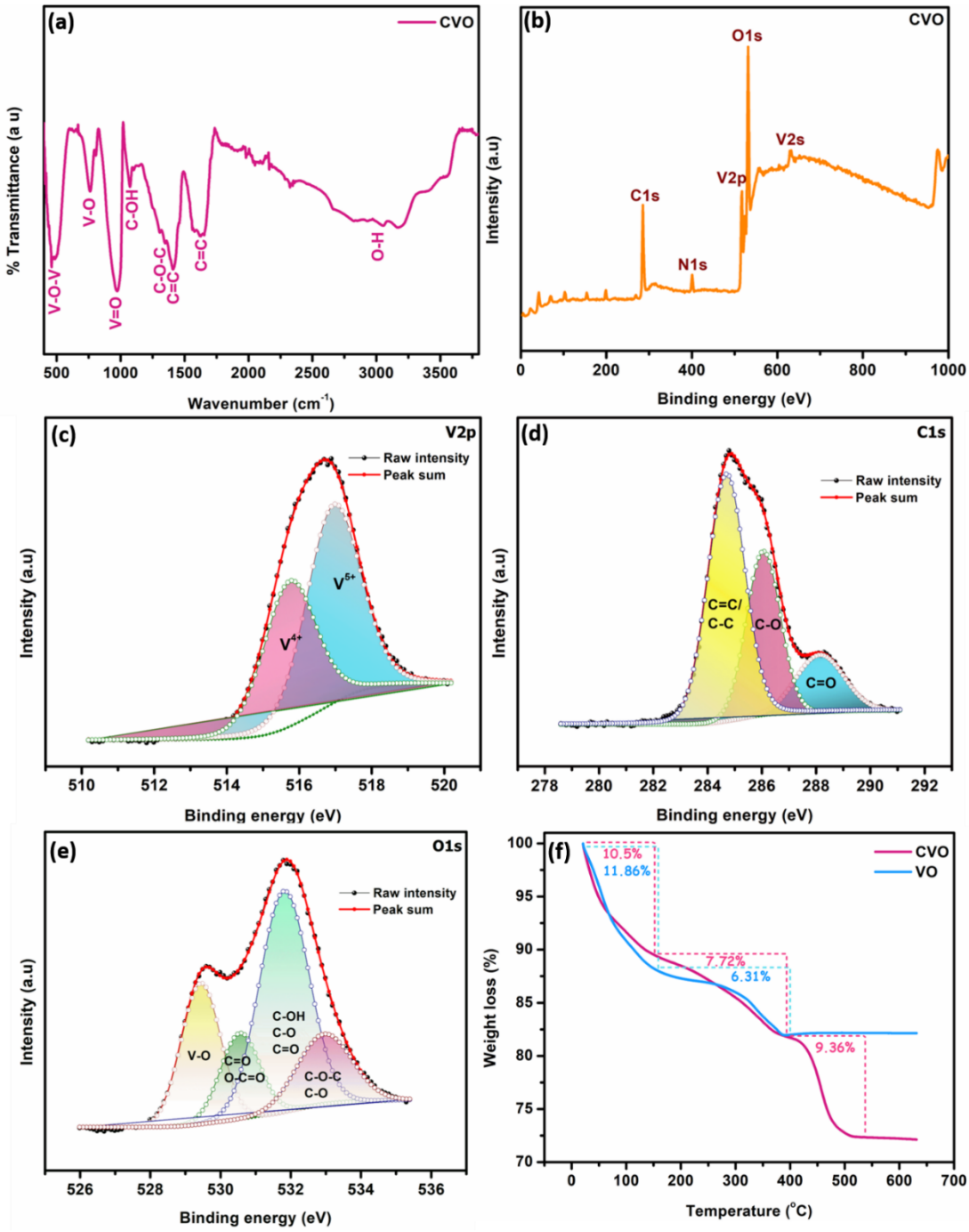

*Figure **2.2** (**a**) FTIR-ATR spectrum and (**b**) XPS survey spectrum of carbonized V_2O_5 aerogels, high-resolution XPS spectra of (**c**) V2p, (**d**) C1s, and (**e**) O1s; (**f**) TGA of aerogels.*

The composite aerogel's chemical structure and functional groups were investigated using Fourier transform infrared (FTIR) spectroscopy (figure 2.2a). The peaks around 460 and 761 cm^{-1} correspond to the V-O-V stretching mode, and the strong peak at 974 cm^{-1} is assigned to the stretching band of oxygen in the V=O bond (Mukhtar *et al*., 2017). The narrowband at 1606 cm^{-1} and broadband near 3200 cm^{-1} are vibration bands of -OH (Cao *et al*., 2013). The bands at 1072, 1302, and 1343 cm^{-1} are attributed to C-OH and C-O-C,

respectively. C=C bands at 1406 and 1618 cm^{-1} and the C=O band at 1573 cm^{-1} support glucose's aromatization (X. Sun & Li, 2004; Y. Zhang *et al*., 2017). The absence of any of the characteristic bands of glucose is also consistent with the concept of the carbonization of glucose under hydrothermal conditions (Z. C. Yang *et al*., 2011). As reported in the literature, the surface functionalization by hydrophilic groups is due to the oxidation of -OH groups in glucose under hydrothermal conditions (X. Sun & Li, 2004; Z. C. Yang *et al*., 2011). Other functional groups like epoxy (C-O-C) and carbonyl (C=O) groups in the composite aerogel might also be due to the partial oxidation during the heat treatment.

The X-ray photoelectron spectroscopy (XPS) survey spectrum in figure 2.2b shows the presence of three elements, namely vanadium, oxygen, and carbon, existing on the surface. It is worth noting that a soft peak of N1s may be derived from the unreacted vanadium precursor, NH_4VO_3. The intense peak around 516.6 eV corresponding to V2p can be deconvoluted into two different electronic states of V^{5+} and V^{4+} (figure 2.2c). The high-resolution XPS of C1s can be fitted by three peaks at 284.7, 286.1, and 288.1 eV attributed to C=C/C-C, C-O, and C=O, respectively (figure 2.2d). The other intense peak of O1s is marked at 530.10 eV, which can be deconvoluted to four peaks, namely, V-O (530.0 eV), C=O, O-C=O (531.4 eV), C-OH, C-O, C=O (532.5 eV) and C-O-C, C-O (532.9 eV) (figure 2.2e) (G.-C. Chen *et al*., 2009; Dong *et al*., 2016; Y. Zhang *et al*., 2018). As evident from FTIR and deconvoluted XPS, many functional groups are induced into the hydrated V_2O_5 nanowire template during the hydrothermal process. These residual functional groups are believed to be beneficial for EMI shielding because they contribute to polarisation and dielectric loss. In fact, the asymmetrical charge distribution in these oxygen-containing dangling bonds polarizes them. As an electromagnetic wave passes through the composite aerogel, these dipoles oscillate under the alternating EM field and cause relaxation loss (Lalan *et al*., 2019; D. Zhang *et al*., 2019).

Thermal decomposition studies were done by thermogravimetric analysis (TGA), and the results are depicted in figure 2.2f. The TGA profile of pure $V_2O_5.nH_2O$ shows two-step weight loss as a function of temperature. The initial weight loss below 150 ºC (11.86%) is attributed to the evaporation of physisorbed water and the other volatile matter retained in the aerogels. In the temperature range of 150-400 ºC, 6.31% weight loss due to the elimination of strongly bound water molecules is recorded (Huguenin *et al*., 2000). A similar weight loss pattern is observed in carbonized aerogels with an additional loss step

at 400 ºC. This extra loss of 9.36% can be attributed to the decomposition of unstable carbon compounds.

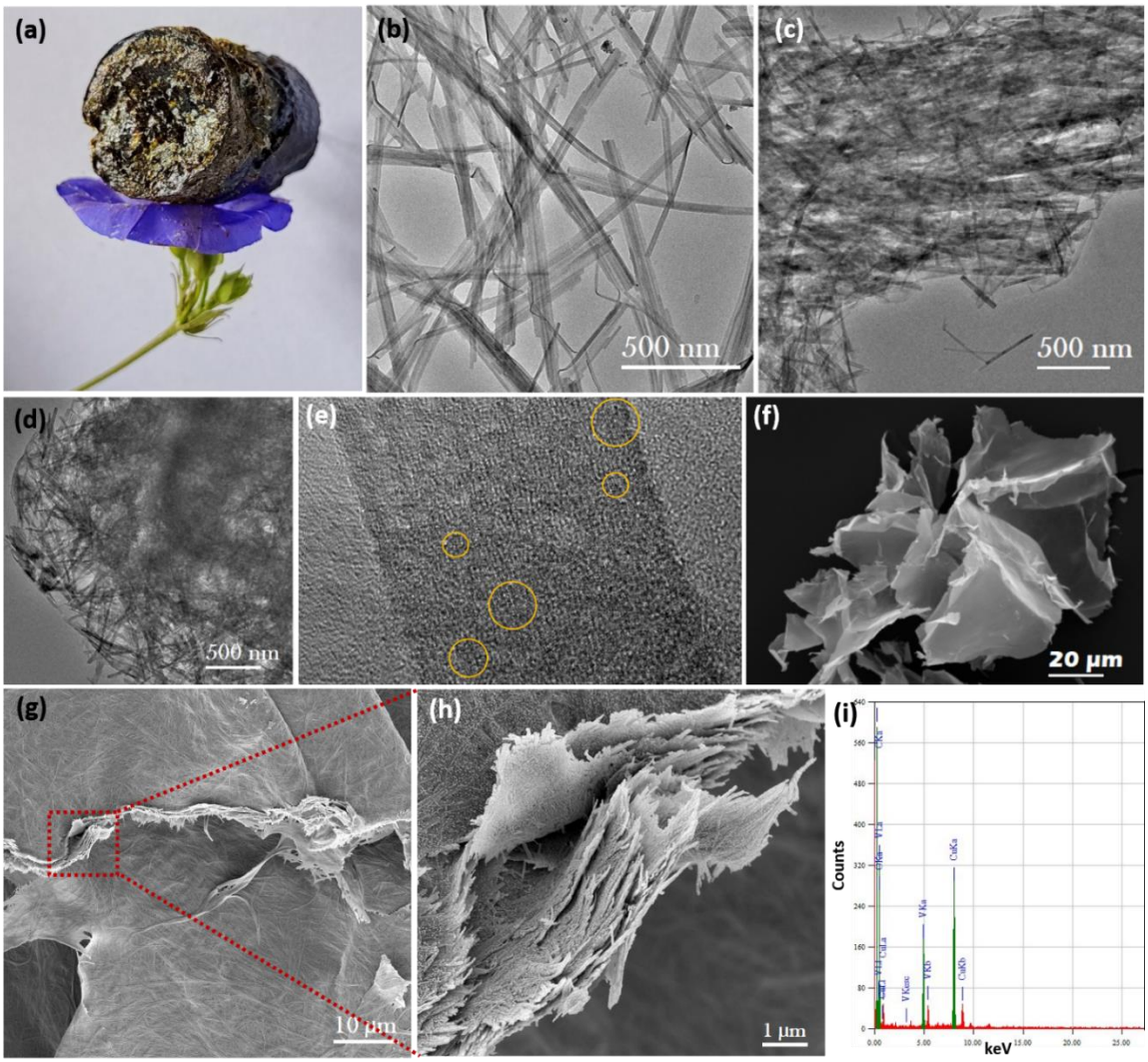

*Figure **2.3** (**a**) photographic image of carbonized V_2O_5 aerogel resting on a flower, TEM images of (**b**) VO and (**c**) CVO aerogels (**d**) TEM image of CVO aerogel showing the carbon layer covered over V_2O_5 nanowires (**e**) HRTEM image of CVO aerogel with encircled portions indicating crystalline parts, SEM image of (**f**) VO aerogel (**g&h**) CVO aerogel at different magnifications, and (**i**) EDS spectrum of CVO.*

Figure 2.3a certifies the ultra-lightness of carbonized aerogel. The nanowire morphology of the pure and carbonized V_2O_5 aerogels is clear from the TEM images (figures 2.3b and c, respectively). In composite aerogel, the nanowires are rigidly bound by polymerized carbon. A closer observation reveals that a thin layer of nanostructured carbon is seen wrapped around the oxide nanowires (figure 2.3d). Although it is difficult to distinguish between the carbon layer and the V_2O_5 nanowires, the HRTEM image suggests the presence of both amorphous and crystalline phases in the composite. The marked

portions in figure 2.3e represent some of the crystalline phases corresponding to $V_2O_5.nH_2O$. The observation by field emission scanning electron microscope (FESEM) provides insight into the micro-morphology of samples and is shown in figures 2.3f-h. As seen, the pure V_2O_5 aerogel presents an irregularly arranged layered but porous structure. The layers are highly flexible with a clean and smooth surface, as shown in figure 2.3f. Composite aerogel is similar to the pristine form nanowire clusters but is connected by a thin envelope of carbon layer (figure 2.3g). This carbon envelope is supposed to provide electrical contact among V_2O_5 nanowires. Further, the highly wrinkled nanowire layers construct a 3D architecture, which can provide a vast surface area for the interaction and scattering of EM waves. A closer analysis shows that the distance between the layers and diameter of pores formed by the layers varies from hundreds of nanometres to tens of micrometers (figure 2.3h). It should be noted that if the pore size in a homogeneous composite is 2-50 nm, it is mesoporous, whereas systems with pores size over 50 nm are categorized as macroporous. Present aerogels fall well within meso and macroporous regimes. These pores formed by curved layers increase multiple reflections, thereby providing a longer propagation path for incoming electromagnetic radiations that suffer collective attenuation. The EDS spectra shown in figure 2.3i once again authenticate the presence of carbon in the composite gel.

The aerogels' porosity and specific surface area were further examined by nitrogen adsorption−desorption isotherms (figure 2.4a& b). Initially, the adsorption is very low but gradually increases with pressure. The type IV isotherm has a hysteresis loop in the high-pressure region ($P/P_0>0.3$). This is because mesopores and macropores in the sample, which agree well with the SEM observation (M. Li, Li, *et al*., 2011). The as-prepared V_2O_5 gel has a surface area of 8.3 m^2/g (figure 2.4a), whereas the BET surface area of carbonized composites measures 48.2 m^2/g (figure 2.4b), which is nearly six times higher than that of the pristine one. Both aerogels contain mesopores of average diameter in the range of 1-50 nm (inset of figure 2.4a& b). The excellent surface area and presence of meso-macropores in CVO aerogels synthesized via hydrothermal carbonization suggest they can display excellent electromagnetic shielding properties.

The as-prepared CVO aerogels with high porosity exhibit decent electrical conductivity (figure 2.4c). Pure aerogel has only a very low conductivity of 0.009 S/cm, which is improved to 0.133 S/cm upon carbonization by 15 times. This considerable

improvement is contributed by the thin carbon layer enveloping the nanowires. Interestingly, an LED light was illuminated when the CVO aerogel was fixed in a circuit (figure 2.4d), which clearly shows the good electrical conductivity of the hybrid gel. The hydrothermally derived carbon over the long and highly connected V_2O_5 nanowire network provides abundant pathways for fast electron movement. This might be the reason for the higher electrical conductivity. The densities of aerogels are also shown in figure 2.4c. The aerogel density was 26 mg/cm^3, slightly more significant than the pure V_2O_5 aerogel (~21 mg/cm^3). The feather-light aerogels can reduce the overall weight of equipment while used as shields in portable devices or aerospace applications.

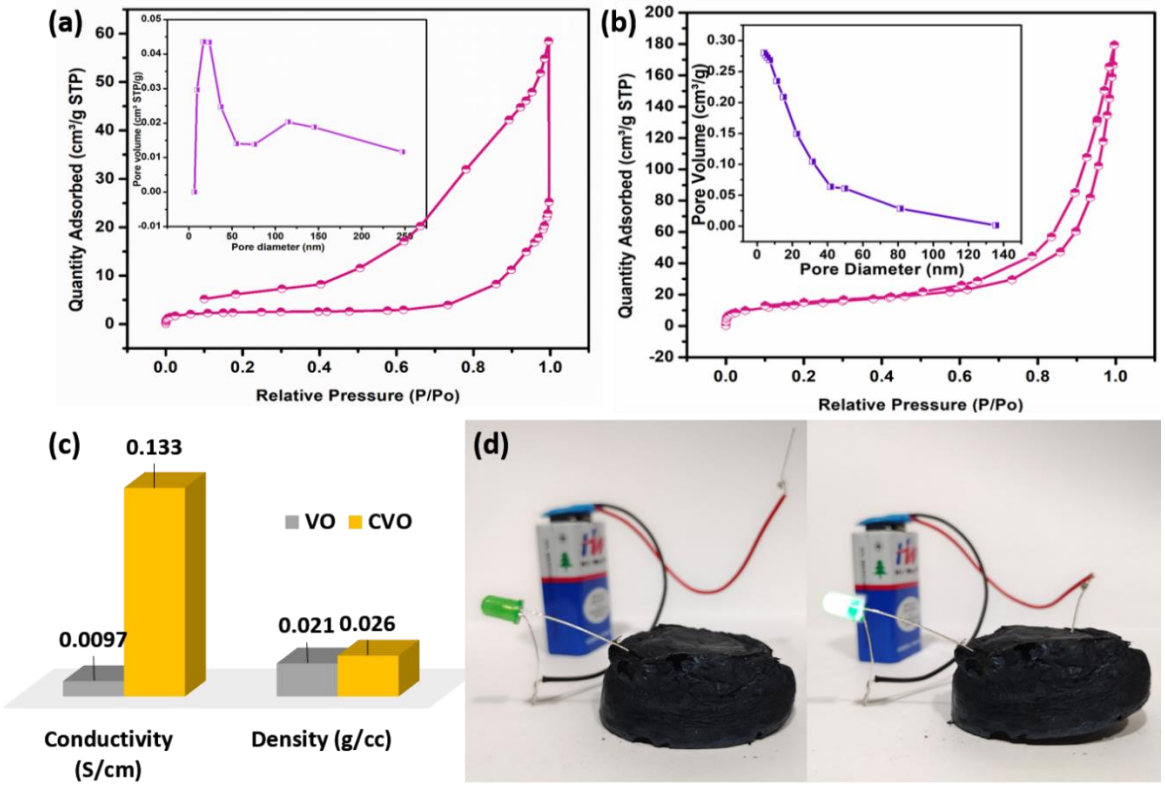

*Figure **2.4** N_2 adsorption-desorption isotherms and pore distribution curves of (**a**) VO and (**b**) CVO aerogel, (**c**) electrical conductivity and density of aerogels; (**d**) LED illuminates when the circuit with aerogel is connected to a power source.*

Now let us look into the possible mechanism behind the formation of carbonized gels. In the past few decades, there have been many reports on the hydrothermal treatment of mono- and poly- saccharides (Ryu *et al*., 2010; X. Sun & Li, 2004; Z. C. Yang *et al*., 2011). Most of them narrate that hydrothermal carbonization using sugars at a temperature in the range of 160- 240ºC resulted in the formation of carbon spheres of diameters 100 nm to a few micrometers. In the present research, we used a cost-effective carbon source,

dextrose, to fabricate conducting vanadium composite aerogels. First, the finely powdered ammonium metavanadate was treated with hydrochloric acid at room temperature and then washed with hot water a few times. The initial yellow solution switches its color to orange and then to deep red with time. Here, polycondensation of vanadic acid occurs, and we obtained a deep red colloidal dispersion containing < 2μm long nanofibers. To this solution, dextrose was added and mixed well by stirring for a few hours. Upon hydrothermal treatment of this mixture at 140ºC for 24 hours, $V_2O_5\,nH_2O$ sheets were formed first, and they were dehydrated and shaped to V_2O_5 nanowires as the reaction progressed (N. Wang *et al*., 2015). The suggested nanowire growth mechanism is the oriented attachment (OA) growth. In this case, the nanofibers formed by polycondensation at room temperature will orient and attach longitudinally to develop tens of micrometers long nanowires under the high temperature and pressure of hydrothermal reaction (M. Li, Kong, *et al*., 2011; X. Wu *et al*., 2003). Meanwhile, hydrothermal carbon formation takes place simultaneously. According to literature, glucose carbonization starts with water loss, followed by polymerization or condensation of the dehydrated and fragmented products (Sevilla & Fuertes, 2009; X. Sun & Li, 2004). Subsequently, the polymer undergoes aromatization. In the case of the hybrid system, glucose, the organic carbon source, plays an additional role as a reductant causing the formation of V^{4+} states by partial reduction, which is evident from XPS analysis (Y. Zhang *et al*., 2017). The polymerized carbon is adsorbed and bound over the long V_2O_5 nanowires leading to the formation of carbonized V_2O_5 composite. The growth of amorphous carbon interrupts vanadium pentoxide's crystallization to complete, as evident from WAXD and TEM results. The temperature and reaction time are crucial for forming the highly porous three-dimensional network. It is reported that most of the hydrothermal carbon composites synthesized in similar routes at low temperatures with sugars as the precursor possessed shallow surface areas, <4 m^2/g (Demir-Cakan *et al*., 2009). However, in the present work, the layered morphology and the carbonization provide a high surface area, which is beneficial for good absorption shielding. Further, we varied the temperature and reaction time of hydrothermal treatment and noticed that a perfect gel structure is obtained with an optimum reaction temperature of 140ºC and 24 hours.

The EMI shielding performance of CVO was investigated in X (8-12 GHz), Ku (12-18 GHz), and K (18-27 GHz) bands. To begin with, the shielding performance of pure V_2O_5 gel was compared to that of carbonized gel. For this, the gels were precisely cut into

rectangular blocks suitable for the X band with 3 mm thickness and scattering parameters (S_{11}, S_{22}, S_{12}, and S_{21}) recorded from a vector network analyzer. Absorption and reflection shielding efficiency were calculated using equations 1.5 and 1.6. Total SE mainly depends on the overall contribution from absorption (SE_{Abs}), reflection (SE_{Ref}), and multiple reflections (SE_M).

$$SE_{Total} = SE_{Abs} + SE_{Ref} + SE_M \quad (2.1)$$

Aerogel-like samples dissipate the internally reflected waves by absorption after multiple scattering. It is said that, for porous materials having an absorption dominant shielding mechanism, the energy of internally reflected signals will be absorbed by the material and can be attributed to absorption (Lalan *et al*., 2019; Tong, 2008; X. Wu *et al*., 2018).

Figures 2.5 (a & b) depict the variation in absorption, reflection, and total shielding ability of VO and CVO aerogels within the X band frequency range. The aerogels display stable shielding efficiency with low fluctuations throughout the measured region, providing a steady shielding bandwidth. The primary shielding mechanism in both the aerogel samples is absorption. Although the unique layered structure of VO contributes to absorption shielding effectiveness (~14 dB), the total EMI SE does not reach up to the commercial benchmark of 20 dB. Reflection shielding stays less than 3.5 dB in the entire frequency span. On the other hand, the carbonized aerogels with a thickness of only 3 mm present an excellent EMI SE of 31.7 dB (>99.9% attenuation) in the X-band. The high shielding efficiency can be attributed to its layered and porous structure and increased electrical conductivity. The conducting network inside the aerogel facilitates microwave attenuation through ohmic and heat loss, and the porous architecture provides ample room for multiple internal reflections. Moreover, carbonization enhances interfacial polarization and dielectric loss due to the formation of polarization centers around a large number of functional groups. Exceptional absorption shielding efficiency up to 29.39 dB is achieved in the X band. Absorption loss is mainly due to heat and ohmic loss inside the aerogel, which is a function of the physical characteristics of the gel. The excellent absorption SE validates that the robust and regular 3D porous skeleton formed in the VO gel is exactly replicated inside the CVO gels, acceding to the SEM-assisted microstructural analysis discussed before. Compared to VO, the absorption SE of CVO is significantly improved by ~10 dB in the X band frequency span. The highly compact and layered microstructure

of the CVO is mainly responsible for the pronounced increase in absorbance EMI SE. Unlike VO gels, the highly connected nanowires and conducting layers provide charge-transporting channels, thereby playing a significant role in the absorption SE. The slight increase in the density of aerogels substantiates the more compact packing of layers. Also, the increase in electrical conductivity contributes to wave attenuation, as in equation 1.4. SE_{Abs} has a gradually increasing trend toward the higher frequency region due to this direct proportion to frequency. On the other hand, SE_{Ref} is inversely proportional to frequency as given in equation 2.2, and hence it moderately decreases towards the higher frequencies. The reflection shielding is given by:

$$SE_{Ref} = -10 \log \left(\frac{\sigma}{16 f \varepsilon \mu}\right) \quad (2.2)$$

where f, σ, μ, and ε are the frequency of EM wave, the shield's total conductivity, and its permeability and permittivity, respectively (M. Wang *et al*., 2021). It is to be noted that the optimum conductivity of CVO aerogel limits the reflection SE in the range of 2.3 to 3.3 dB. The high degree of impedance matching is also responsible for the lower values of reflection SE (Tong, 2008). As a result, only a negligible amount of harmful secondary reflection enters the external environment.

Next, we probed into the dependence of shielding performance of aerogels on thickness in the X band. Figure 2.5c shows the total shielding efficiency of CVO at three different thicknesses; 3, 4, and 5 mm, namely CVO 3, CVO 4, and CVO 5, respectively. Shielding performance is more or less linear concerning the thickness of the shield. As expected, the reflection shielding is independent of the thickness of samples and displays a value < 4 dB. Absorption SE reaches 30.7 and 34.3 dB, with the maximum total SE achieving 32.6 and 37.0 dB for 4 and 5 mm thick samples. A minimum shielding efficiency of 31.3 dB is ensured in the entire X band for the 5 mm thick aerogel. This suggests that a 5 mm thick sample will suffice for the practical requirements demanding 99.99% shielding capacity.

Skin depth (δ) is the distance through which the initial intensity reduces to 37%. The relation of skin depth with absorption shielding efficiency of materials with a fixed thickness, *t* is:(Zhan *et al*., 2019)

$$SE_{Abs} = 20 \frac{t}{\delta} log\, e \quad (2.3)$$

Figure 2.5d shows the higher skin depth of pure aerogels in the X band frequency range, ~2 mm. Upon carbonization, the value was immensely reduced to ~1 mm. So, CVO

aerogels with >1 mm thickness can well attenuate the EM waves inside them.

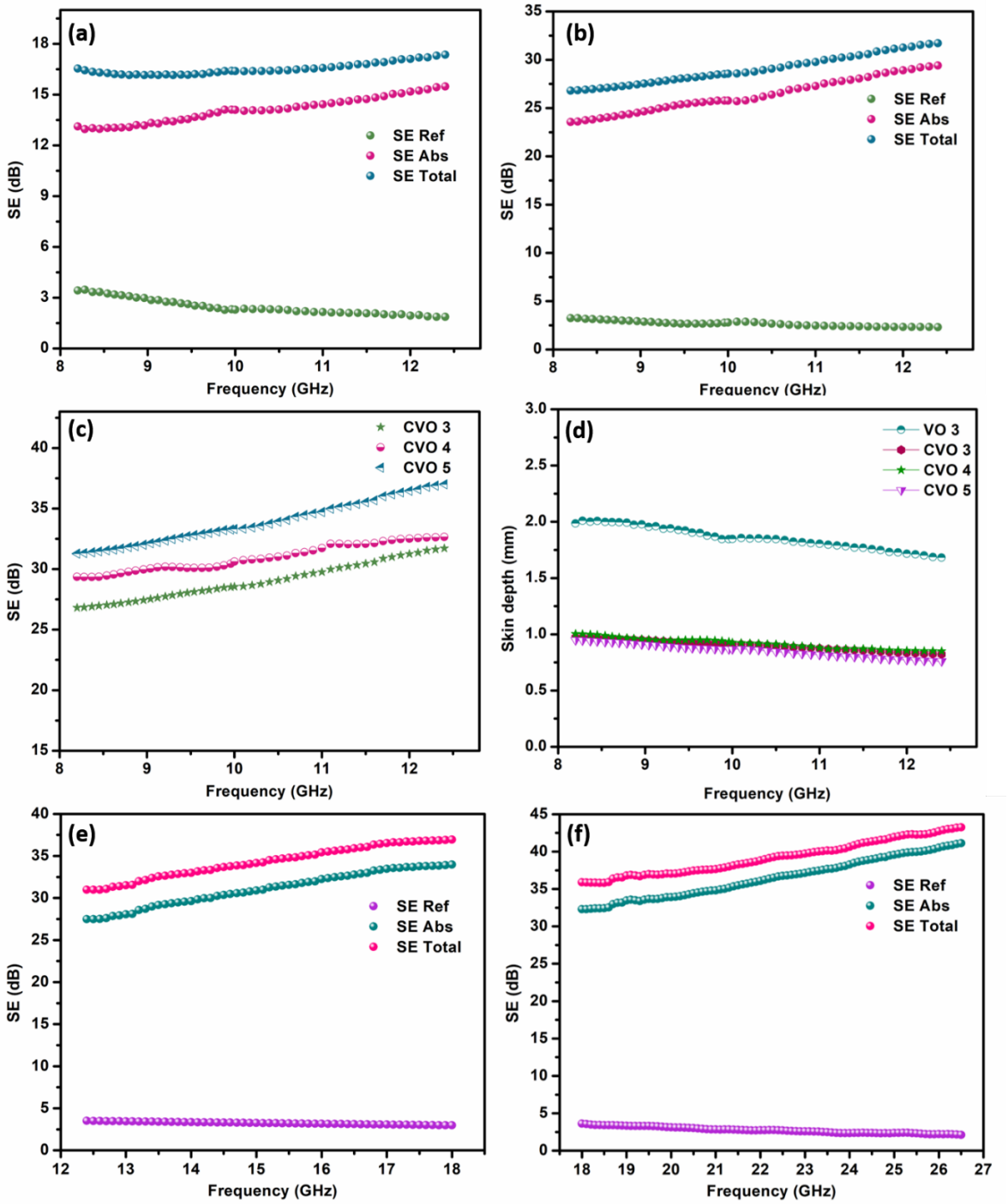

*Figure **2.5** Frequency-dependent variation of total EMI shielding effectiveness (SE_{Total}), reflection shielding effectiveness (SE_{Ref}), and absorption shielding effectiveness (SE_{Abs}) of (**a**) VO and (**b**) CVO aerogels (**c**) Variation of total shielding efficiency of aerogels with different thicknesses3-, 4- and 5-mm and (**d**) frequency variation of skin depth of aerogels in X band. Frequency-dependent variation of total EMI shielding effectiveness (SE_{Total}), reflection shielding effectiveness (SE_{Ref}), and absorption shielding effectiveness (SE_{Abs}) of CVO aerogel in (**e**) Ku band and (**f**) K band.*

Further, the shielding efficiency of aerogels was investigated in Ku and K bands (figure 2.5e and f). CVO gels with 3 mm thickness depict a maximum shielding efficiency of 36.95 dB and 43.24 dB in the Ku and K band. The aerogels have high absorption shielding with a shallow reflection below 3.5 dB in the entire Ku and K bands. In brief, the hybrid CVO aerogel is a potential shielding solution for portable devices, with broad bandwidth in all three frequency bands, X, Ku, and K bands.

The detailed shielding mechanism can be summarised as illustrated in figure 2.6a. The aerogel's meso- and macropore structures favor the facile entry of incoming electromagnetic waves into the aerogel due to suitable impedance matching with the interface. As the EM waves penetrate CVO aerogel, the highly interconnected 3D conductive network enhances the conduction loss. The continuous conducting wires facilitate necessary electron transport channels, which promotes dielectric loss. The abundant polarization centers provided by the functional groups of CVO and interfaces between V_2O_5 nanowires and polymerized carbon would produce lots of dipoles. These dipoles will rotate by absorbing energy from the alternating electromagnetic field, and relaxation occurs, resulting in EM attenuation. In addition, the unfiltered waves will get trapped inside the wrinkled and folded layers and eventually attenuate inside them. Also, the vast interface area provided by the aerogel's layered-porous architecture encourages multi-scattering and internal reflections inside the aerogel. These multiple internal reflections elongate the propagation path of the incident waves and dissipate them within the aerogel. Finally, the synergistic effects caused by the combination of organic carbon and hydrated V_2O_5 nanowires might also be responsible for high shielding performance. In summary, the unique porous morphology combined with the good electrical and dielectric properties of CVO aerogels makes them suitable for light EMI shielding applications.

The EMI SE normalized by density is a crucial term for light and porous shielding structures like aerogels. Specific shielding efficiency ($SSE=SE_{Total}$/density) and thickness averaged SSE (SSE/thickness) are commonly used to compare the shielding performance among different light materials. Materials with high specific shielding capacity are highly preferred in portable electronic and aeronautical applications. The calculated SSE values of CVO aerogel at different frequency bands are shown in figure 2.6b. The maximum SSE/thickness in the K band is 5147.6 dB cm^2/g, much higher than many reported low-dense aerogels (figure 2.6c). Table 2.1 highlights aerogels' excellent specific shielding

ability in present work compared to similar materials in literature. For example, Han *et al.* prepared graphene oxide aerogel film/polymer composites with high shielding efficiency of 53 dB. As its density is 0.122 g/cm^3, SSE/thickness turns out to be ~2800 dB cm^2/g (Han *et al.*, 2016). Table 2.1 below suggests that the outstanding normalized SSE possessed by CVO aerogels makes them a competitive candidate among light-shielding materials.

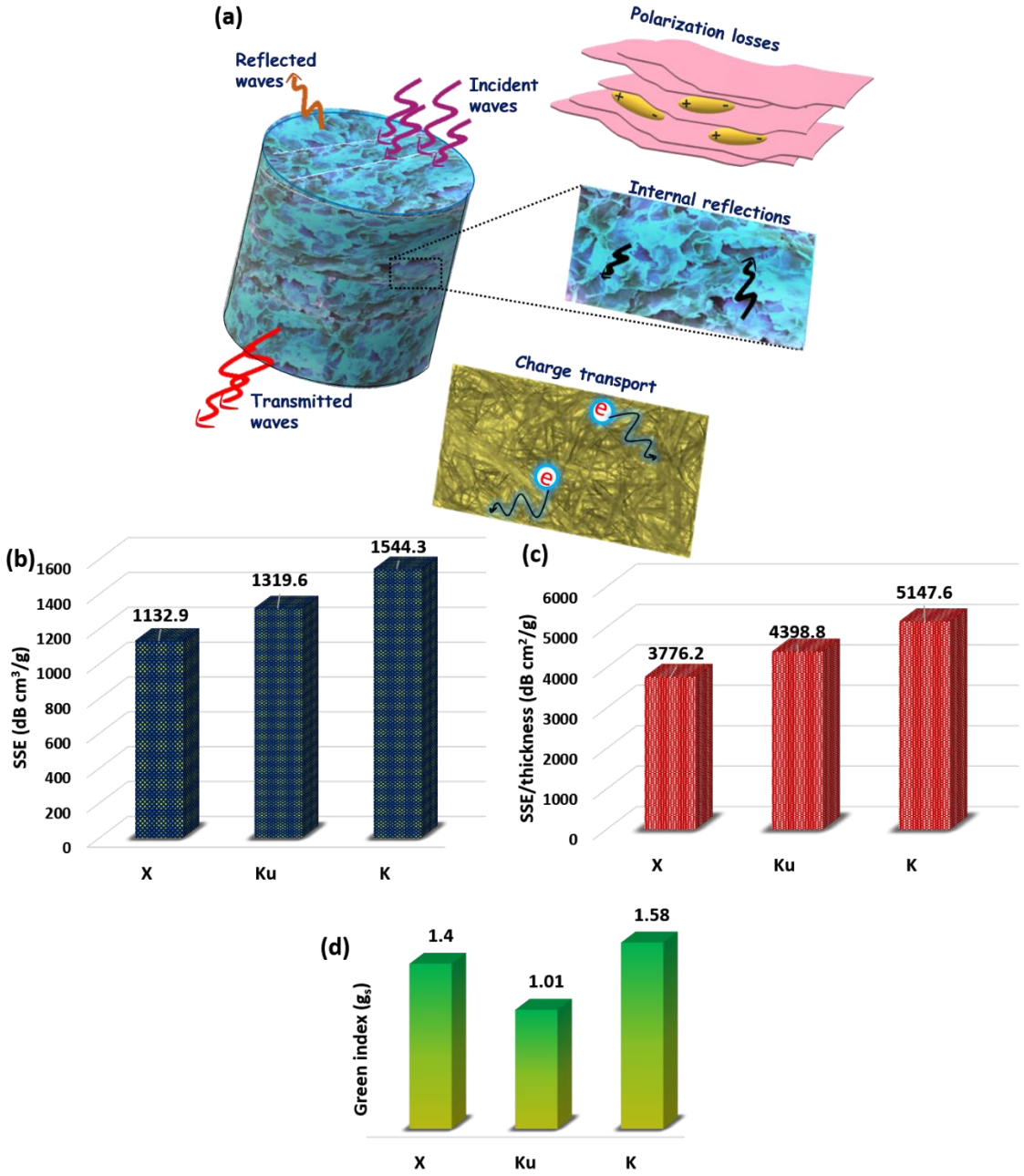

*Figure **2.6 (a)** Illustration showing the possible shielding mechanism in CVO aerogel; (**b**) Specific shielding efficiency (SSE), (**c**) SSE/thickness, and (**d**) green index of CVO aerogel in X, Ku, and K bands. The values correspond to the maximum frequency of each band.*

*Table **2.1**. Comparison of present work's EMI SE, SSE, and SSE/thickness with other reported results. The values are measured at X band frequency.*

Sl No	**Sample**	**EMI SE (dB)**	**Thick-ness (mm)**	**SSE (dB cm^3/g)**	**SSE/ thickness (dB cm^2/g)**	**Ref**
1	Cellulose composite aerogel	20.8	2.5	219	876	(H. D. Huang *et al*., 2015)
2	MXene carbon composite aerogel	71.3	3	360	1200	(Liang *et al*., 2020)
3	GO-polymer aerogel film	53	1.55	434	2800	(Han *et al*., 2016)
4	Aerogel-like Carbon	51	10	455	455	(Y. Q. Li *et al*., 2015)
5	Graphene-carbon hybrid aerogel	37	3	529	1763.333	(W. L. Song *et al*., 2015)
6	Carbon aerogel	40	4	700	1750	(Vazhayal *et al*., 2020)
7	Sponge-supported rGO aerogel	27.3	12	1437	1197.5	(C. Liu *et al*., 2016)
8	V_2O_5-PANI aerogels	34.7	6	1662.2	2770.333	(Puthiyedath Narayanan *et al*., 2021)
9	Carbonized V_2O_5 aerogels	31.7	3	1132.9	3776.333	**Present work**

Lots of materials are available with the same or higher shielding capacity at even lower thicknesses. The main three parameters that distinguish CVO from those shields are cost-effectiveness, ease of synthesis, and its 'green' nature. The materials with outstanding EMI attenuation properties usually generate strong secondary reflection, which risks the environment's health. Bringing high EM loss in an environment-friendly shielding architecture is highly challenging. So, it is high time to consider the 'greenness' of our CVO

aerogels. For this, we examined the green index, g_s which can be calculated from scattering parameters using the following equation (X. Wang *et al*., 2019):

$$g_s = \frac{1-{S_{12}}^2}{{S_{11}}^2} - 1 \tag{2.4}$$

Although many EMI shields have superior SE and SSE, only a few are reported with impressive green values. Generally, shields with g_s values >1 are considered green among EM wave attenuators. An ideal green shield needs the following features: (1) strong absorption, (2) low reflection, (3) high EM loss, and (4) good impedance matching. In the case of CVO aerogels, the impedance of the porous surface matches well with that of incoming EM waves. Also, the layered microstructure enhances absorption with multiple reflections inside its vast interfaces. The lower conductivity value reduces the reflection, which we already discussed, considering its EMI performance. With polarization and ohmic losses, the cumulative EM loss is high enough to achieve a green index value as great as 1.58 in the K band. The g_s were >1 in X and Ku bands, as shown in figure 2.6d. Hence the present ultra-light CVO aerogels exhibiting tailorable EMI shielding properties, are eco-friendly and suitable as shields in portable devices. These results demonstrate that instead of employing expensive 2D materials like graphene and MXene for developing efficient EMI shielding solutions, interesting mesoporous structures can be made through one-pot synthesis using relatively cheaper precursors, which could also show incredible green shielding properties.

2.4 Conclusions

In summary, a novel, ultralight carbonaceous aerogel with high EMI shielding performance was developed by the carbonization of the V_2O_5 nanowire network. The one-pot hydrothermal preparation method is appealing mainly for two reasons; firstly, it saves time, and secondly, it is less laborious. Advantageous is the choice of precursor materials, ammonium metavanadate and the carbon source D-glucose, that are cheaper and abundant, making the final product relatively low-cost. Spectroscopic analyses and elemental mapping confirmed the carbonization of V_2O_5 nanowires that constitute the 3D structure of the aerogel. The specific surface area of the composite aerogel was found to increase nearly six times upon carbonization compared to the pure V_2O_5 aerogel. BET isotherm also suggests the presence of a fair amount of micro and mesopores. Low dense CVO aerogel

(26 mg/cm^3) exhibits good electrical conductivity of 0.133 S/cm. Superior EMI shielding performance of 31.7 dB (3 mm thickness) with exceptional absorption shielding efficiency of 29.39 dB is achieved in the X band. An aerogel sample with 5 mm thickness shows shielding efficiency up to 37 dB in the same band. As observed in the SEM image, the ingenious porous structure promotes multiple internal reflections and scattering of EM waves inside the aerogel interfaces, thus contributing to higher absorption shielding efficiency. The extended carbonized V_2O_5 nanowire network provides highly connected charge transport channels, which helps dissipation of electromagnetic waves trapped inside the aerogel. CVO gels with 3 mm thickness achieve maximum shielding efficiency of 36.95 dB and 43.24 dB in the Ku and K bands. The high shielding ability of gels can be attributed to the peculiar morphology and synergistic effects of polymerized carbon and hydrated V_2O_5 nanowires. All the measured samples show broad bandwidth throughout the frequency bands measured. The CVO aerogels display high specific shielding efficiency and SSE/thickness of 1544 dB cm$^{3/}$g and 5147.6 dB cm^2/g, respectively, in the K band. These values were found to be much higher compared to many reported low-dense aerogels. The aerogel also possesses an exceptional green index value of 1.58 at 26.5 GHz. Using cheaper precursors employed here, the facile hydrothermal strategy opens new avenues for growing efficient, environment-friendly EMI shields with affordable materials.

Chapter 3

Aerogels of V_2O_5 Nanowires Reinforced by Polyaniline for EMI Shielding

- Novel ultra-light EMI shielding aerogels made of a 3D network of nanowires of layered oxide V_2O_5 are reported for the first time.
- The V_2O_5 gel network reinforced by PANI was prepared by a facile polymerization followed by freeze-drying.
- Lightweight aerogels of density as low as 0.02 g/cm^3 displayed an impressive specific shielding efficiency of 1662.2 dB cm^3 g^{-1}
- V_2O_5 -PANI aerogels show an absorption-dominant shielding mechanism with the highest green index of ~ 2.91.

3.1 Introduction

Hydrogels amalgamate the advantages of the excellent electronic properties of conducting polymers with a three-dimensional (3D) continuous network based on an inorganic oxide. Polyaniline, probably the most studied conducting polymer, is a favorable candidate in EMI shielding aerogels because of its easy availability, ease of synthesis, low cost, controllable electrical conductivity, and better environmental stability (Bhadra *et al*., 2009; Stejskal *et al*., 2008). Recently, Huangfu *et al.* investigated the shielding property of PANI/Multi-walled carbon nanotube (MWCNT)/graphene aerogel and found that they could achieve a maximum shielding efficiency of 42 dB in the frequency range of the X band (Huangfu *et al*., 2019). Polyaniline (PANI)/graphene aerogel (GA) synthesized via the in-situ polymerization process using ammonium persulfate as the oxidizing agent has shown an EMI SE of 42.3 dB at 11.2 GHz for a sample thickness of 3 mm (Y. Wang *et al*., 2019).

Although scores of publications surface every month on EMI shielding, less focus has been made on synthesizing aerogels, especially carbon filler-free conductive polymer aerogels, with good shielding efficiency. A combination of three- dimensional, porous inorganic nanoarchitecture and properties of a conducting polymer is charming for an electromagnetic shield. The synthesis of carbon-free conductive aerogels is a big challenge due to the criticality in maintaining electronic transport and the complications involved in supercritical drying, which can likely result in gel collapse from capillary action. Making environmentally friendly EMI shields, which do not create EM pollution through secondary reflection, is also important. As seen in the previous chapter, the green index is assigned to measure the eco-friendliness of EMI shields. Green shields require less reflection loss and high absorption loss (X. Wang *et al*., 2019). Here in this chapter, we discuss the EMI shielding aspects of V_2O_5 nanowires fortified into a 3D network, which acts as an oxidizing template to synthesize polyaniline-based hydrogel. (Ahirrao *et al*., 2018; Purushothaman *et al*., 2017; Xiong *et al*., 2008).

In the present research, green V_2O_5 – PANI composite aerogel was prepared by polymerizing aniline monomer using three- dimensional array of V_2O_5 nanowires. In sharp contrast to the previous chapter, carbonization and hydrothermal conditions are avoided here, while PANI is used as the polymer matrix. To the best of our knowledge, ours is the

first report on using a combination of layered inorganic oxide (V_2O_5) and a conducting polymer (PANI) in lightweight microwave attenuator applications. The structure, morphology, formation of gel, and the EMI shielding properties of V_2O_5 – PANI composite aerogel are investigated in detail. The aerogel has a very low density with a maximum EMI SE of 34 dB in the X band and an impressive specific EMI SE of 1662.2 dB cm^3 g^{-1}.

3.2 Experimental

3.2.1 Materials

Ammonium metavanadate (NH_4VO_3, 99%) was purchased from Sigma-Aldrich Co. USA. Aniline ($C_6H_5NH_2$), and hydrochloric acid (HCl, 37%) were obtained from Merck Life Science Private Limited, Mumbai. All the chemicals were used as received without any further treatment.

3.2.2 Synthesis of V_2O_5 nanowire dispersions

The V_2O_5 nanowire dispersion was prepared following the same procedure as in chapter 2. The obtained dispersion was then refilled with hot water to a total volume of 40 mL. In order to study the effect of aging in the EMI assay, the dispersions were kept from 5 days to 70 days. The dispersion after a proper aging period is named the V_2O_5 precursor.

3.2.3 Synthesis of hydrogel

About 0.42 mL of aniline monomer was dispersed in 40 mL of deionized water. The viscous V_2O_5 nanowire dispersion was taken in a rectangular-shaped mold of an appropriate dimension. Composite hydrogels of V_2O_5-PANI were synthesized by immersing the mold of V_2O_5 nanowire dispersion in the prepared aniline monomer dispersion. Gelation happens instantaneously. The solution was kept at room temperature for a few hours to complete the gelation. Hydrogels were freeze-dried at -60 ºC for 24 hours, and the V_2O_5 -PANI aerogels (VP aerogels) were obtained. For comparison, the corresponding V_2O_5 aerogel (V aerogel) was also fabricated by directly freeze-drying the V_2O_5 precursor solution at -60 ºC for 24 hours. Samples with and without polymerization were coded as VP and V, respectively, and the following number is the days of aging of V_2O_5 dispersion. For example, V 30 means the V_2O_5 aerogel sample (i.e., without

polymerization) with an aging period of 30 days, while VP 30 is V_2O_5 -PANI composite with its precursor stored for 30 days.

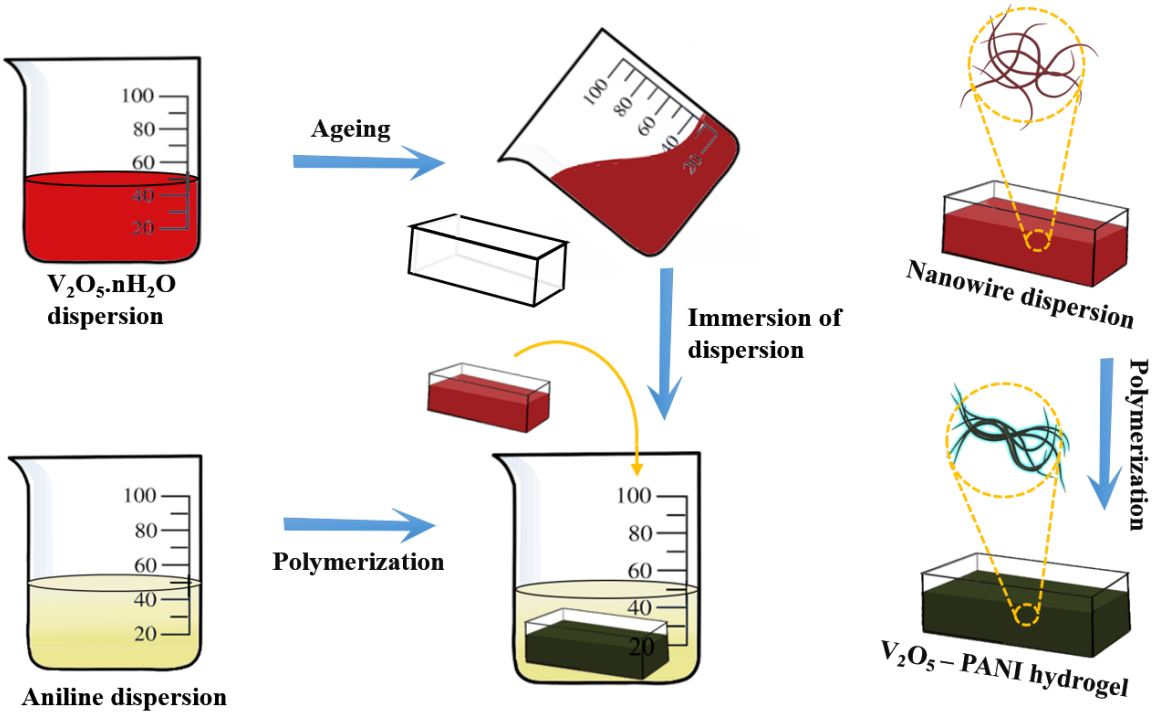

*Figure **3.1** Schematic illustrating the fabrication of V_2O_5- PANI aerogel*

3.2.4 Characterization

The formation of V_2O_5 and V_2O_5- polyaniline composite was identified and confirmed by detailed spectroscopic analysis. The Fourier transform infrared (FTIR) was used to compare the precursor's chemical structure before and after polymerization using Nicolet Magna 560 FTIR (Thermo Scientific, Waltham, MA, USA). Raman spectra were recorded with a confocal Raman microscope (α-300R WITec Inc., Ulm, Germany). The microstructures of the samples were analyzed using a scanning electron microscope (SEM) (JEOL- JSM 5600LV, Akishima, Tokyo, Japan). WAXD measurements were carried out on a XEUSS SAXS/WAXS system using a Genixmicro-source (Xenocs, Grenoble, France) operated at 50 kV and 0.6 mA to identify the chemical structure of precursor dispersion. The morphology and nanowire growth with aging was studied by high-resolution transmission electron microscopy – HRTEM (FEI Tecnai G2 30S-TWIN, FEI Co., Hillsboro, OR, USA). The chemical composition was analyzed using X-ray Photoelectron Spectroscopy (XPS) 500 Versa Probe 2 with Al Kα radiation (PHI, Physical Electronics,

Chanhassen, MN, USA). Thermogravimetric analysis was done using a Simultaneous Thermogravimetric Analyzer (STA 7300, Hitachi, Japan). The samples were heated from 25ºC to 650ºC at a rate of 10ºC min^{-1} in the air atmosphere. The Brunauer–Emmett–Teller (BET) surface area and pore size of the samples were measured after degassing the samples at room temperature for 12 hours using a nitrogen adsorption-desorption isotherm (Gemini 2375, Micromeritics, Norcross, USA). The pore size distributions of the aerogels were measured using the Barrett–Joyner–Halenda (BJH) method. The DC conductivity of the samples was calculated using the four-probe method from Keithley 2450 source meter.

Here in the present investigation, the electromagnetic characterization of the V_2O_5 and V_2O_5- PANI aerogels was performed at the X band (8.2-12.4 GHz) of the microwave frequency range by VNA, Agilent E5071C, Santa Clara, CA, USA. The dimension of samples used in the X band is 22.8 mm × 10.1 mm × 6 mm. Keysight PNA-L network analyzer N5234B was used for the Ku and K band measurements. The corresponding sample dimensions are 15.79 mm × 7.89 mm × 6 mm for the Ku band and 10.67 mm x 4.32 mm × 4 mm for the K band.

3.3 Results and discussion

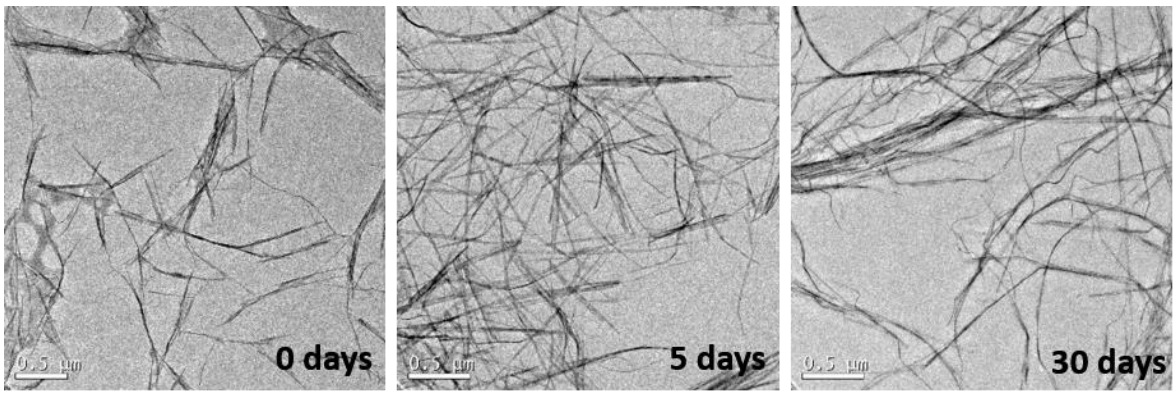

*Figure **3.2** TEM images of V_2O_5 dispersion 0, 5, and 30 days of storage*

The aerogels synthesis involves several tricky steps, which begin with meticulous growing and crosslinking of solid nanoparticles to form a three-dimensional solid network wherein pores are filled with solvent. This is attained by aging to give sufficient strength to the network, and then the solvent is carefully removed by freeze-drying, leaving the aerogel structure intact. The schematic of the synthesis procedure adapted for the preparation of V_2O_5-PANI hydrogel is shown in Figure 3.1. Initially, ribbon-like hydrated

V_2O_5 nanofibers were prepared through polycondensation of vanadic acid in the water at room temperature. In this method, a fine powder of ammonium metavanadate was acidified with hydrochloric acid. As time passes, the solution turns its color from yellow to orange and then to red. The deep red, colloidal dispersion remained at room temperature for a few weeks.

Figure 3.2 shows the transmission electron microscopy (TEM) images of V_2O_5 nanoribbons at different duration of aging. Longitudinal dimensions of nanofibers in the range of 0.3 – 2 μm were formed initially, and subsequently, they have grown up to tens of micrometers. In contrast, there is no significant change in the width of wires during aging. As seen, a network of intertwined nanowires was obtained with storage times beyond fifteen days. The proportionate increase in the length of V_2O_5 nanowires with reaction time is ascribed to the self-assembling nature of V_2O_5 nanowires, even at room temperature. This is explained by the mechanism of oriented attachment growth in which V_2O_5 nanofibers orient and attach to form ultra-long wires (M. Li, Kong, *et al*., 2011). The as-prepared V_2O_5 nanofiber dispersion was carefully immersed in an aniline solution where *in-situ* oxidative polymerization occurs rapidly. The color switch from deep red to dark green confirms the polymerization of aniline. Gelation happens simultaneously, and the tube-inversion test verified the formation of a hydrogel. Here, the strong oxidizing character of the vanadium oxide causes polymerization. At the same time, they act as an inorganic template on which the organic material can bind and grow (Sacanna & Pine, 2011). The absence of any residue in the final solution indicates that the polymerization happens selectively over the nanowires. It is reported that gelation in a colloidal suspension of long fibrils leads to structures with low solid content. The high aspect ratio of the colloids is said to be the reason for the observed yield stress at low concentrations (Philipse & Wierenga, 1998). Hence, in the present V_2O_5 colloidal system, the formation of a 3D network is possible because of the high aspect ratio of nanowires. The fast polymerization of aniline makes a permanent hydrogel structure that is retained after its lyophilization. Hydrogels, which differ in shape and size, could be prepared directly using different molds. We observed that the reaction conditions and storage time play a vital role in hydrogel formation. After several trials, we found that V_2O_5-PANI aerogel prepared with an aging time of 30 days has ample machinability and good EMI shielding efficiency of 34.74 dB. Hence, this sample was qualified for further characterizations.

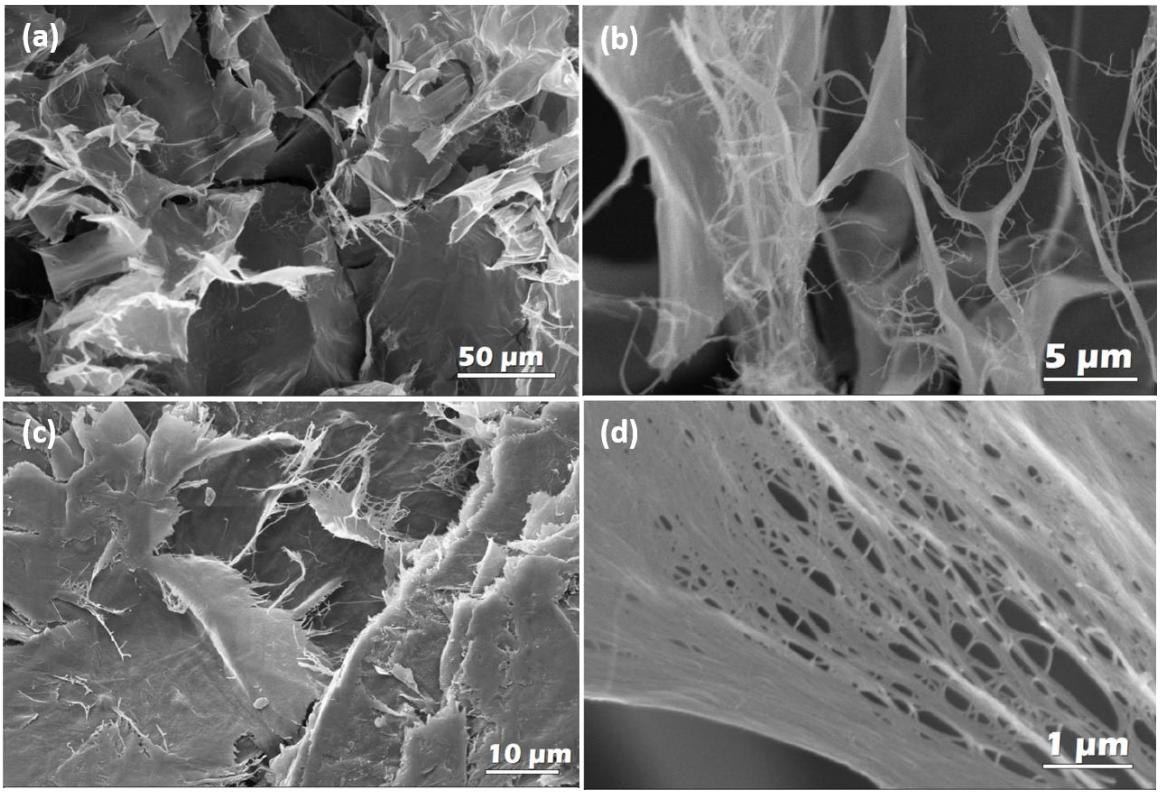

*Figure **3.3 (a&b)** SEM images of V 30 aerogels at different magnifications, **(c&d)** SEM images of VP 30 aerogels at different magnifications.*

The microscopic structure of the aerogel is obtained from scanning electron microscopy (SEM). Figures 3.3a-d shows SEM images of V_2O_5 precursor and V_2O_5-PANI aerogel at different magnifications. SEM image clearly reveals that the aerogel has an ultra-porous but layered structure, with each sheet in a layer consisting of interwoven nanowires with diameters less than 20 nm. Nanowires are clustered together to form web-like structures that are extended as sheets woven with nanowires. The observed irregularly arranged layered 3D aerogel architecture is believed to be beneficial to multiple internal reflections of electromagnetic waves, which helps to achieve absorption dominant EMI shielding effectiveness. Also, the folds in the layers and voids between sheets provide more interfaces for the dissipation of electromagnetic waves. The magnified image of the V_2O_5 precursor shows a sea of uniformly distributed nanowires that forms a matrix. After polymerization, several fibers are aligned to form a small bundle-like structure bound together by the polymer. Figure 3.3d shows the magnified portion of a single aerogel layer, where the polymer well bounds the nanowires. The presence of polymer can be identified by the bright regions in this SEM image.

Transmission electron microscopy (TEM) (see figure 3.4a-d) further confirmed the nanowire morphology of V_2O_5 dispersion. Nanowires are ultrathin with an average diameter in the range of 4-16 nm. TEM and SEM results of the aerogel and V_2O_5 dispersion show the retention of the precursor's skeleton even after the gelation. This suggests that the structure of precursor dispersion played an essential role as a chassis for forming V_2O_5-PANI hydrogel (see figure 3.4f). The observed high aspect ratio of nanowires is vital in determining the connectivity and electron conductivity, which can also be beneficial to supplement the shielding efficiency of the final aerogel. Figures 3.4e & g show the photographic images of aerogels V 30 and VP 30. The aerogels are so light that they could lay on a delicate flower's stamen without drooping.

The chemical structure of the precursor dispersion was characterized by wide-angle X-ray diffraction (WAXD). Diffraction patterns of the dispersion and V_2O_5- PANI aerogel are shown in figure 3.5a. Five reflection peaks are observed at 2θ values of 15.2º, 21.8º, 26.6º, 31.1º, and 32.4º, respectively, corresponding to (200), (101), (110), (301), and (011) reflections of the orthorhombic V_2O_5 (Abd-alghafour *et al*., 2016). Surprisingly, the WAXD pattern of V_2O_5-PANI aerogel is similar to that of the V_2O_5 precursor with no additional peaks of PANI. This may be due to low crystallinity and lower volume percentage of conducting polymer in the VP aerogel (Mostafaei & Zolriasatein, 2012). However, the remarkable decline in the intensity of peaks suggests the presence of foreign incorporation in the initial precursor. Let us further examine the aerogels using infrared and Raman spectroscopy to assess the presence of PANI in the composites.

The formation of PANI in the final aerogel was examined by FT-IR spectroscopy (figure 3.5b). The bands at 1558 and 1450 cm^{-1} are attributed to C=C and C=N stretching of the benzenoid and quinoid ring units in PANI, respectively. The bands related to C−N stretching and C−H bending of phenyl units are found at 1240 and 1127 cm^{-1} (K. Zhou *et al*., 2018). The peaks around 472 cm^{-1} are assigned to V-O-V stretching mode, and peaks at 608 and 711 cm^{-1} correspond to the stretching of triply coordinated oxygen atoms between three vanadium atoms. Doubly coordinated oxygen bond, V-O-V contributes to the peak at 828 cm^{-1} (Chu *et al*., 2016; Margoni *et al*., 2017; X. Zhou *et al*., 2013). Characteristic peak at 1000 cm^{-1} can be assigned to the terminal oxygen stretching in the V=O bond (Pandit *et al*., 2017). The deformation band of H_2O is situated at 1609 cm^{-1} (Cao *et al*., 2013).

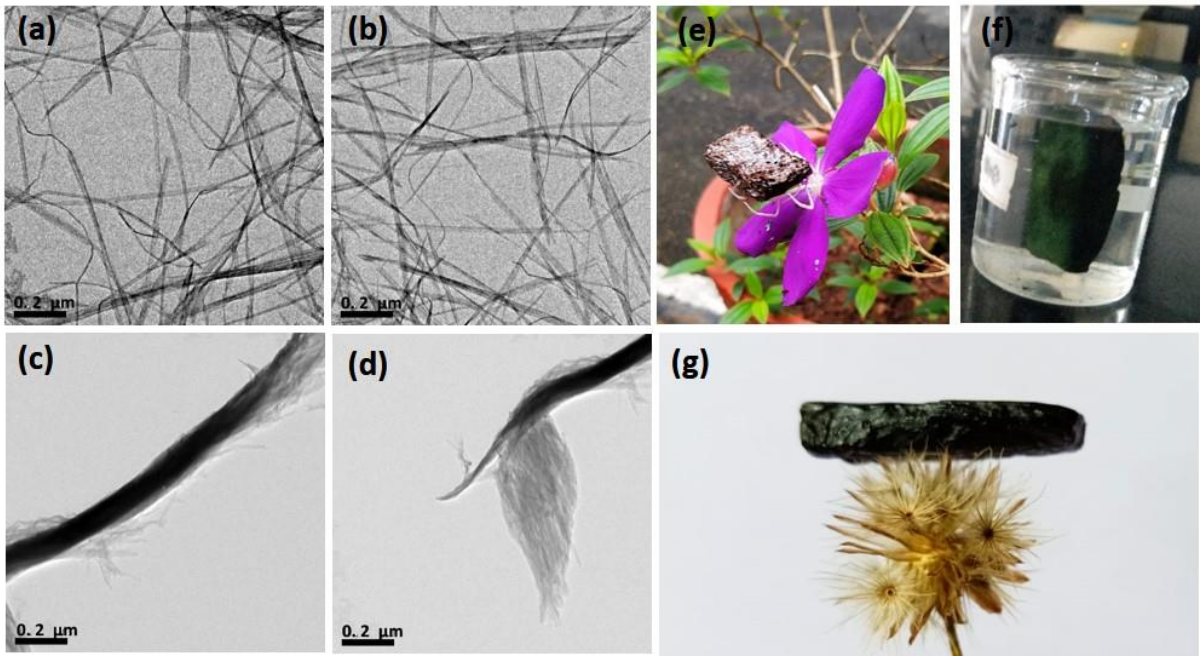

*Figure **3.4** (**a**) & (**b**) TEM images of V 30 aerogels, (**c**) & (**d**) TEM images of VP 30 aerogels, photographic images of (**e**) V 30 aerogel resting on a flower, (**f**) VP 30 hydrogel floating in DI water and (**g**) VP 30 aerogel resting on a flower.*

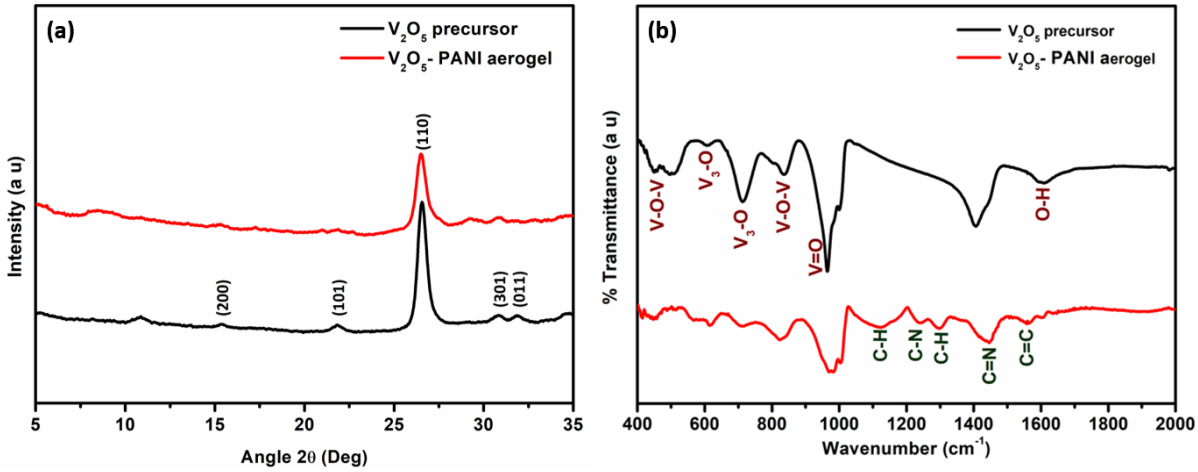

*Figure **3.5** (**a**) WAXD pattern and (**b**) FTIR spectra of V_2O_5 precursor and V_2O_5-PANI aerogel*

The formation of polyaniline was further confirmed using Raman spectroscopy, which can distinguish the vibrations of benzenoid and quinoid segments in PANI. Figure 3.6a displays the Raman spectra of V_2O_5 precursor and V_2O_5- PANI aerogel in the wavelength range of 0-1750 cm^{-1}. The spectrum for precursor shows characteristic bands of V_2O_5. The peaks can be assigned to Raman modes for the V_2O_5 orthorhombic phase. The dominant peak at 143 cm^{-1} is attributed to the V-O-V chain vibrations, pointing out

the layered orthorhombic structure of the V_2O_5 phase (Abd-alghafour *et al*., 2016). The peak located at 289 cm^{-1} is assigned to the bending vibration of the V=O bonds. The peak located at 484 cm^{-1} is assigned to the bending vibrations of the bridging V-O-V (doubly coordinated oxygen) (Ahmad *et al*., 2015). The peak at 693 cm^{-1} is assigned to the doubly coordinated oxygen (V-O-V) stretching mode, which results from corner-shared oxygen common to both pyramids. The peak at 995 cm^{-1} corresponds to the V=O stretching mode, which is associated with the crystallinity quality and stoichiometry of the samples (Abd-alghafour *et al*., 2016; Ahmad *et al*., 2015). The peaks at 1170, 1340, and 1561 cm^{-1} in the V_2O_5- PANI aerogel spectrum are assigned to in-plane C-H bending of the quinoid ring, the C-N stretching vibration, and C=C is stretching of the benzenoid ring respectively, confirming the presence of PANI (Jin *et al*., 2018). Thus, our Raman and FTIR studies undisputedly confirmed the polymerization of aniline in the aerogel.

The surface composition and chemical state of the V_2O_5- PANI aerogel were studied by X-ray Photoelectron Spectroscopy (XPS). XPS survey scan (Figure 3.6b) reveals the chemical state of vanadium (V), oxygen (O), nitrogen (N), and carbon (C). Two peaks observed at around 517 and 524 eV, respectively, are assigned to V $2p_{3/2}$ and V $2p_{1/2}$. The deconvoluted V2p spectra (figure 3.6c) suggest that the aerogel contains predominantly V(V) (517.1 eV) and a small amount of V(IV) (515.7 eV). This indirectly proves that the aerogel's major skeleton is built by V_2O_5 nanowires. The +4 oxidation state may be due to the small amount of VO^{2+} ion formed by partial reduction of vanadium in ammonium metavanadate salt by its reaction with hot hydrochloric acid (Ibris *et al*., 2005). O1s peak at 531 eV shows the presence of oxygen. The peak centered at 285 eV is assigned to the carbon backbone of PANI. The results of the curve-fitting show three broad peaks, at 284.6, 285.6, and 287 eV (see Figure 3.6d). The peak at 284.6 eV indicates the presence of quinoid structure and benzenoid rings, whereas peaks at ~285.6 and 287 eV are attributed to C-N and C-O, respectively. N1s peak observed at 400.7 eV can be attributed to PANI. The asymmetric peak can be deconvoluted into three peaks, namely, quinoid amine (–N=) at 399.6 eV, benzenoid amine (–NH–) at 400.4 eV, and the nitrogen cationic radical ($–N^+$) at 401.4 eV (Patil *et al*., 2018) (See figure 3.6e).

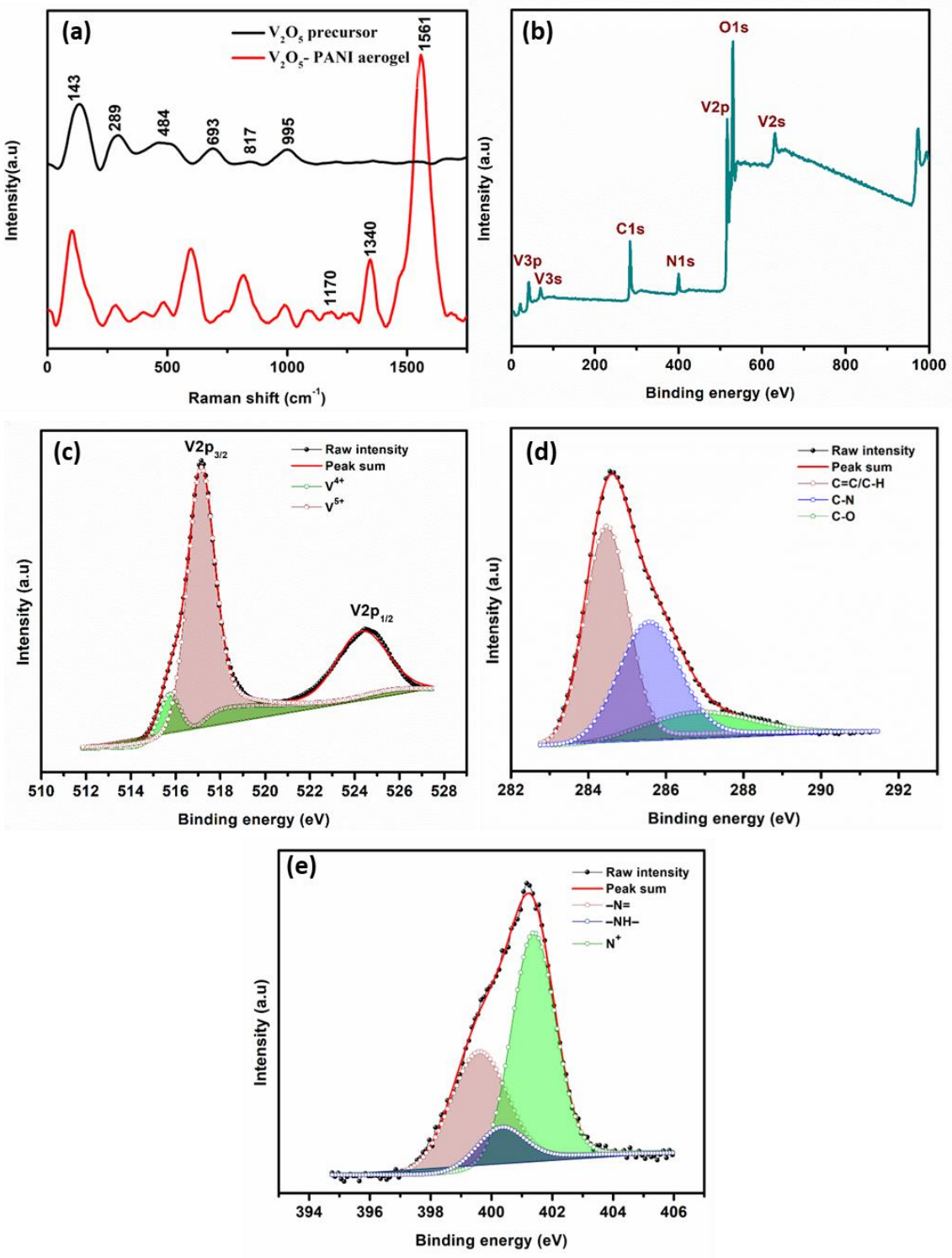

*Figure **3.6** (**a**) Raman spectra of V_2O_5 precursor and V_2O_5-PANI aerogel,(**b**) XPS survey spectrum of V_2O_5-PANI aerogel, high-resolution XPS spectra of (**c**) V2p, (**d**) C1s and (**e**) N1s.*

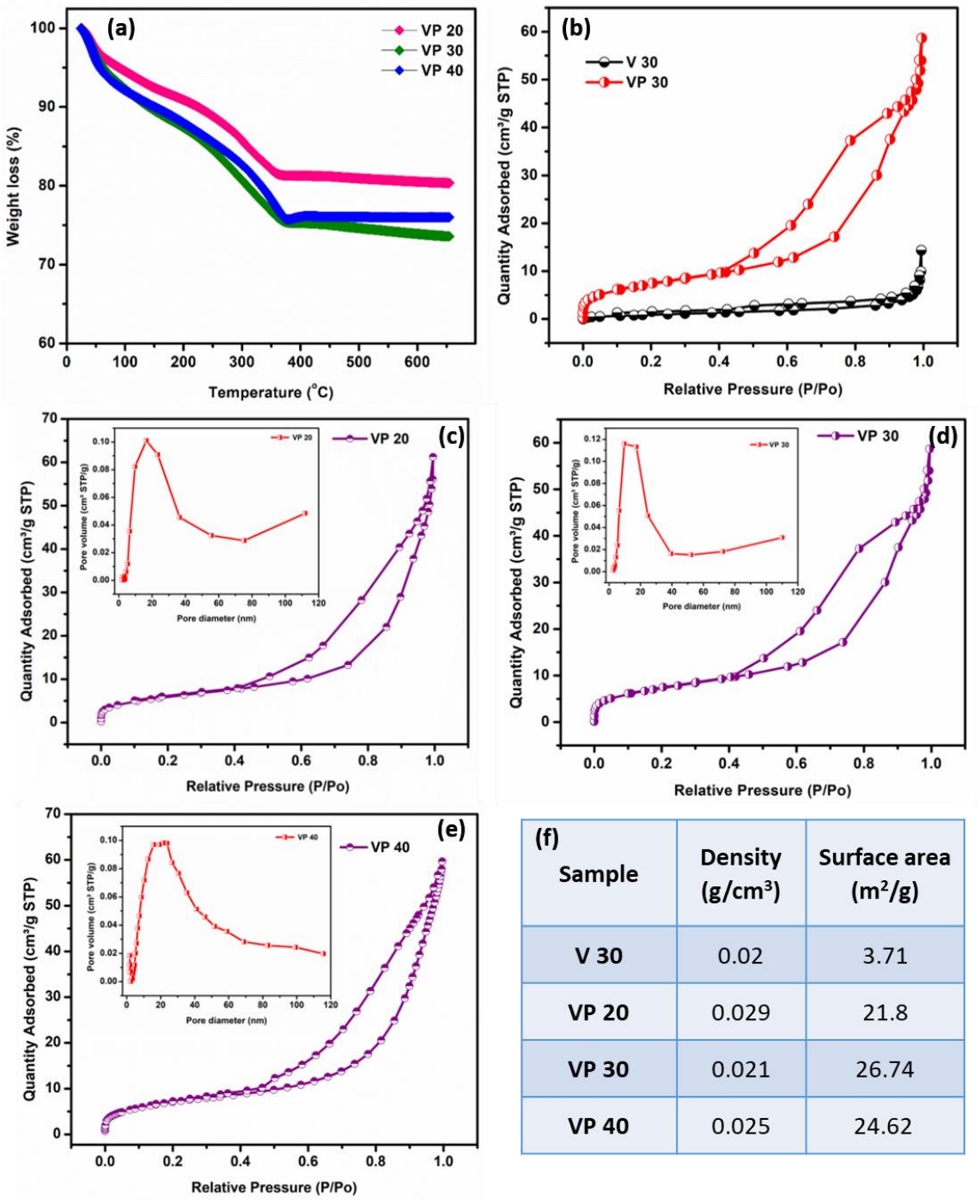

(f)

Sample	Density (g/cm³)	Surface area (m²/g)
V 30	0.02	3.71
VP 20	0.029	21.8
VP 30	0.021	26.74
VP 40	0.025	24.62

*Figure **3.7** (**a**) TGA of V_2O_5-PANI aerogels prepared with V_2O_5 dispersions at different periods of aging. (**b**) N_2 adsorption-desorption isotherms of V 30 and VP 30 aerogels, N_2 adsorption-desorption isotherms, and pore distribution curves of aerogels (**c**) VP 20, (**d**) VP 30, (**e**) VP 40, and (**f**) tabulation of density and surface area of aerogels.*

In order to understand the composition of aerogel samples, thermogravimetric analysis (TGA) was done. TGA diagram of V_2O_5 -PANI aerogel (Figure 3.7a) shows two different weight loss steps. The initial weight loss below 100 ºC is due to the evaporation of water and other volatile matter retained in the sample. Polyaniline decomposition occurs

near 400 ºC (Park *et al*., 2010). The amount of V_2O_5 in the V_2O_5-PANI aerogels is indicated by the plateau above 400 ºC. The V_2O_5 contents in the aerogels VP 20, VP 30, and VP 40 are estimated to be approximately 81%, 76%, and 75%, respectively. This implies that the sample VP 30 has a higher polymer content than other samples. The higher the amount of PANI in the composite, the higher the conductivity. Hence VP 30 is expected to have more shielding efficiency.

The BET surface area was determined for samples from the nitrogen adsorption−desorption isotherms. The observed isotherm (Figure 3.7b) belongs to type IV of the Brunauer−Deming−Deming−Teller classification. The actual BET surface area and pore volume of the V_2O_5-PANI aerogel obtained are 26.74 m^2/g and 0.075 cm^3/g, respectively. The surface area of various aerogel samples is given in figure 3.7f. Compared with the V_2O_5 precursor, aerogel shows approximately seven times increase in the surface area and eight times increase in pore volume. Polymerization clearly increased the specific surface area and pore volume, favoring the dissipation of electromagnetic waves. The pore size distribution curve indicates that the main pore diameter of aerogel samples has a wide pore size distribution range of 5- 100 nm, with the main pore diameter in the range of 5- 50 nm. BET isotherms and pore distribution curves of samples VP 20 – 40 are shown in figure 3.7c-e. The improved high specific surface area and interlayer voids are believed to increase the propagation path of the electromagnetic waves and thus favor efficient EM energy dissipation.

The lightness of aerogels was verified by measuring their densities. There is no observable difference in the density of samples V 30 and VP 30. The apparent density of samples is ~0.02 g/cc. Figure 3.7f gives the densities of various samples. It is evident that the ultra-low density helps to improve the specific shielding efficiency of V_2O_5 -PANI aerogels as an attractive candidate for lightweight shielding applications.

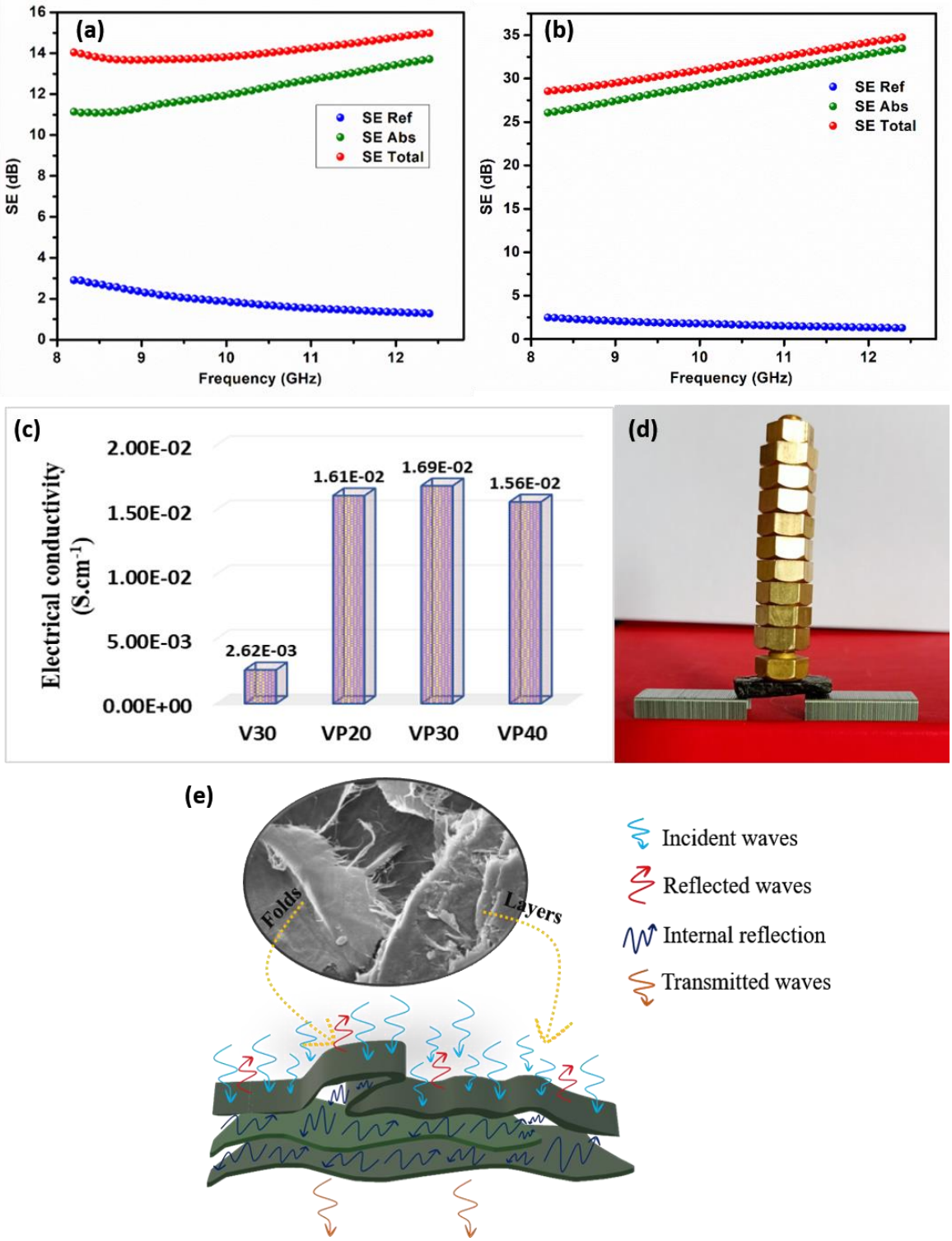

*Figure **3.8**. Frequency-dependent variation of total EMI shielding effectiveness (SE_{Total}), reflection shielding effectiveness (SE_{Ref}), and absorption shielding effectiveness (SE_{Abs}) of **(a)** V 30 **(b)** VP 30 over X band frequency range (8.2–12.4 GHz). **(c)** The electrical conductivity of various aerogels. **(d)** A digital image showing an as-prepared VP aerogel (340 mg) supports ~1000 times its weight (~340 g). Each bolt weighs ~30g. **(e)**Schematic illustration of the shielding mechanism happening at the polymer wrapped V_2O_5 layers in the interior of the aerogel.*

Figures 3.8a and b depict the variation of the EMI SE of V_2O_5 -PANI aerogel of thickness 6 mm as a function of frequency. EMI SE values of the composite aerogels were determined in the X band of the microwave frequency range (8.2–12.4 GHz), widely used in broadband communications, satellite communications, space communications, and radars (Dragoman *et al*., 2019). Aerogels show excellent EMI shielding efficiency above 20 dB, the minimum required SE for commercial applications. With different periods of aging of V_2O_5 dispersion, the total shielding efficiency value of V_2O_5 -PANI aerogel varies between 23-35 dB. For an aging period of 30 days, aerogel showed a maximum shielding efficiency of 34.74 dB. The specific EMI SE values of V 30 and VP 30 were calculated to be 883.5 and 1662.2 dB cm^3 g^{-1}, respectively.

As seen before, the basic mechanism of EMI shielding is the sum of the contribution due to reflection from the material surface (SE_{Ref}), absorption (SE_{Abs}), and the multiple internal reflections of electromagnetic radiation (Dijith *et al*., 2018). Reflection loss comes from the mismatch in impedance between the incident wave and shielding material. Shielding through absorption is due to ohmic and heating loss in the shielding material (Lalan *et al*., 2019). It can be clearly seen that SE_{Abs} values are much larger than SE_{Ref} over the entire frequency range. For V 30, the values of SE_{Total}, SE_{Abs}, and SE_{Ref} at the frequency 12.4 GHz are 14.99, 13.72, and 1.27 dB, respectively, while the corresponding values for VP 30 are 34.74, 33.46, and 1.28 dB, respectively. This clearly suggests that aerogel samples exhibit an absorption dominant shielding mechanism, which is obvious for porous shielding materials. High volume gas fractions in aerogels reduce the reflection loss, as they could minimize the impedance mismatch. Since the reflection loss of the electric field is inversely proportional to frequency, maximum shielding efficiency due to reflection is achieved at a lower frequency range. Unlike reflection loss, shielding by absorption shows an increasing trend with frequency. This is expected because absorption loss in a material is proportional to the square root of frequency, given by Equation 3.1;

$$A = 131\, t\sqrt{f\mu\sigma} \tag{3.1}$$

where A is the absorption loss, t is the thickness of the shielding material, f is frequency, and μ is relative permeability (Tong, 2008).

Compared to the V_2O_5 sample, V_2O_5 -PANI aerogel's SE nearly doubled. Improved shielding efficiency after polymerization can be attributed to increased interconnections between the nanowires and enhancement of interaction between electromagnetic waves and conducting polymer. The electrical conductivity of composite material is a crucial parameter in determining EMI shielding performance. Figure 3.8c shows the electrical conductivity of samples. With the introduction of conducting polymer, electrical conductivity is increased by ten times that of the sample before polymerization. The aging of nanowire dispersion controls the nanowire growth and determines polyaniline's conjugation and chain length. Samples with a higher amount of polymer and longer polymer chains will be expected to show higher conductivities (C. G. Wu *et al*., 1996). From TEM and TG analyses, it is clear that VP 30 has longer nanowires and higher PANI content. Hence it has a higher conductivity of 1.69×10^{-2} S cm^{-1} than V 30. This obviously contributes to its better EMI SE.

The above results suggest that the incorporation of PANI though marginally only improves the SE_{Ref} value, significantly improves the SE_{Abs} values. The formation of a more conducting network by PANI contributes to the overall absorption loss of the aerogel. As a result of simultaneous polymerization and gelation, the polymer binds the V_2O_5 nanowires together to form interconnected 3D architecture with more interfaces. This multilevel layered 3D structure enhances the specific surface area of the sample, which is evident from BET analysis. This causes abundant multi-scattering and enhances the transmission path of EM waves, resulting in a significantly improved shielding performance. The irregularly arranged layers and the folds on the layers bring about more reflection for the EM wave (Figure 3.8e). This increases the propagation path of EM waves and causes their attenuation. In conclusion, the excellent EMI performance of the V_2O_5 -PANI sample is from the synergistic effect between conducting polymer and the 3D framework construction (D. Zhang *et al*., 2019). In addition to the improvement in microwave attenuation, the polymer reinforcement has significantly improved the compressive strength of the V_2O_5-PANI aerogel. Our qualitative testing proves that (see Figure 3.8d) the as-prepared VP aerogel (340 mg) could support up to 1000 times its weight (~340 g). However, detailed mechanical testing is needed to confirm its mechanical strength quantitatively.

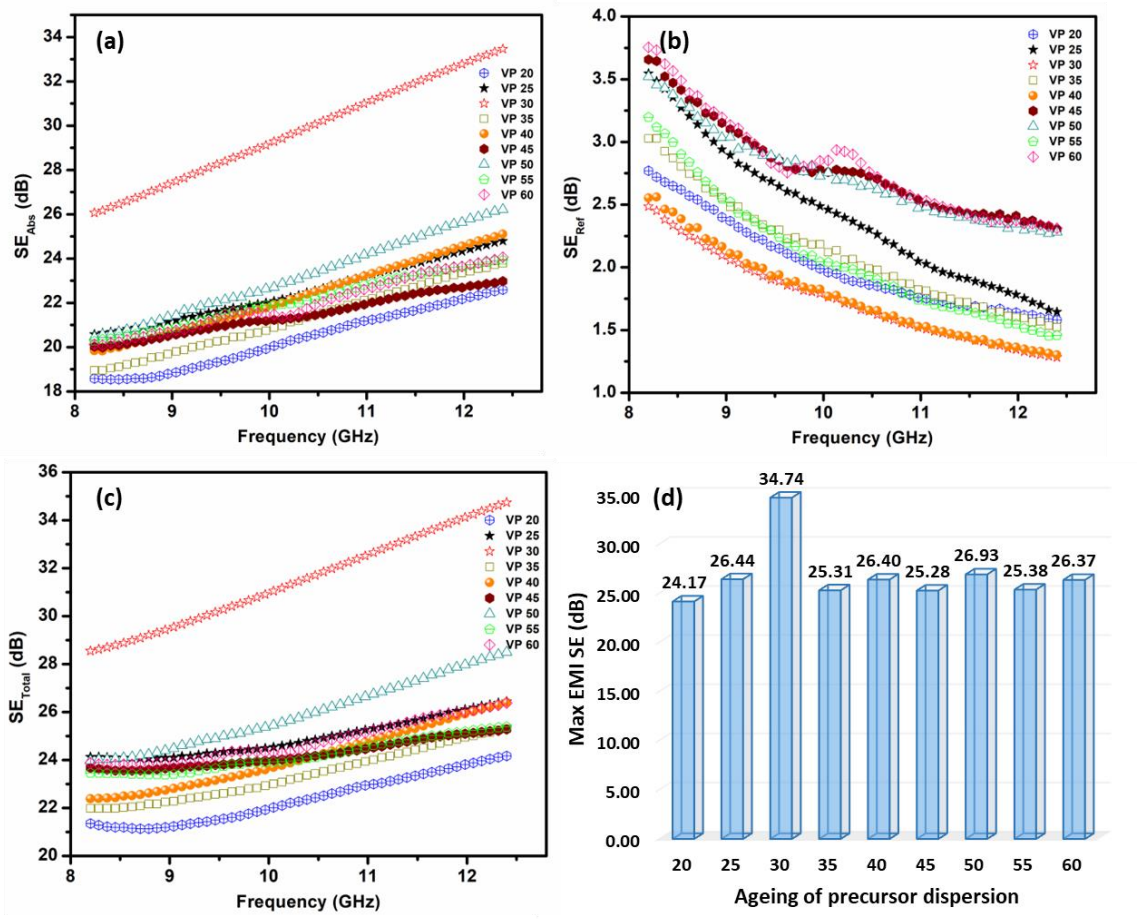

*Figure **3.9** Frequency variation of the(**a**) SE_{Abs}, (**b**) SE_{Ref}, and (**c**) SE_{Total} of V_2O_5 -PANI aerogels prepared with different aging. (**d**) Variation of maximum shielding efficiency of composite aerogels as a function of the aging time of the precursor dispersion.*

The frequency variation of the SE_{Ref}, SE_{Abs}, and SE_{Total} of V_2O_5 -PANI aerogels prepared with different aging times ranging from 20 days to 60 days in the X band frequency range is given in Figure 3.9a-c. All the samples have an SE value greater than 20 dB (<1% of incident waves are transmitted). As aging increases from 20 to 30 days, the aspect ratio of nanowires increases. The high aspect ratio improves the connectivity inside the aerogel, enhancing the EMI SE. Figure 3.9d shows the variation of maximum shielding efficiency with aging. Max EMI SE for aerogels aged over 30 days varies around 26 dB. Slight variations may be due to machining errors with the samples. Aerogel with 30 days of aging shows superior shielding efficiency compared to all other samples. As evident from TEM and TG analyses, the extreme aspect ratio and highest PANI content could be the reasons for the highest EMI SE. It can be inferred that the aspect ratio of nanowires in VP 30 is optimum for forming an efficient PANI conducting network.

*Table **3.1** A comparative analysis of shielding effectiveness values of porous materials measured in X-band.*

Sl No	Sample type	EMI SE (dB)	Thickness (mm)	SSE (dB cm^3/g)	Ref
1	MWCNT/Cellulose aerogels	19.1	2	-	(C. Wan *et al*., 2016)
2	Anisotropic Graphene Aerogels	32	4	-	(X. H. Li *et al*., 2016)
3	PAM/CNF/MWCNT composite hydrogels	28.5	2	-	(W. Yang *et al*., 2018)
4	Pyrolyzed/ ARF aerogels	20	2	-	(Abolghasemi Mahani *et al*., 2018)
5	Graphene-PMMA foam	19	2.4	25	(H. Bin Zhang *et al*., 2011)
6	CB/EPDM	18	5.5	30.3	(Ghosh & Chakrabarti, 2000)
7	CNT-PS foam composite	20	1.2	33.1	(Y. Yang & Gupta, 2005)
8	PEI/graphene/Fe_3O_4 foam	18.2	2.5	41.5	(Shen *et al*., 2013)
9	Graphene/PEI foam	12.8	2.3	44.1	(Ling *et al*., 2013)
10	MXene/Calcium alginate aerogel film	54.3	0.026	46	(Z. Zhou *et al*., 2019)
11	PP−SSF composite foams	48	3.1	75	(Ameli *et al*., 2014)
12	Nano-copper/CDCF	29.3	2	92	(Jiao *et al*., 2019)
13	C/SiO_2/SiC aerogels	24	6	120	(An *et al*., 2019)
14	Cellulose composite aerogel	20.8	2.5	219	(H. D. Huang *et al*., 2015)
15	Cellulose composite aerogel	20.8	2.5	219	(H.-D. Huang *et al*., 2015)

16	CuNi-CNT foam	54.6	1.5	237.4	(Ji *et al*., 2014)
17	Graphene foam	56	1	311	(Xing *et al*., 2019)
18	Graphene/PDMS foam	20	1	333	(Z. Chen *et al*., 2013b)
19	Phthalonitrile Carbon Foam	51.2	2	341.1	(L. Zhang *et al*., 2016)
20	MXene carbon aerogel	71.3	3	360	(Liang *et al*., 2020)
21	GO-polymer aerogel film	53	1.55	434	(Han *et al*., 2016)
22	DLG/Ni NPs/CFs	50.6	0.65	448	(C. Wan *et al*., 2020)
23	Aerogel-like Carbon	51	10	455	(Y. Q. Li *et al*., 2015)
24	Graphene-carbon aerogel	37	3	529	(W. L. Song *et al*., 2015)
25	Carbon aerogel	40	4	700	(Vazhayal *et al*., 2020)
26	Graphene oxide-cellulose aerogels	58.4	2	1061	(C. Wan & Li, 2016)
27	Porous MWCNT/WPU	20	2.3	1148	(Zeng *et al*., 2016)
28	Sponge-supported rGO aerogel	27.3	12	1437	(C. Liu *et al*., 2016)
29	V_2O_5-PANI aerogels	34.7	6	1662.2	**Present work**

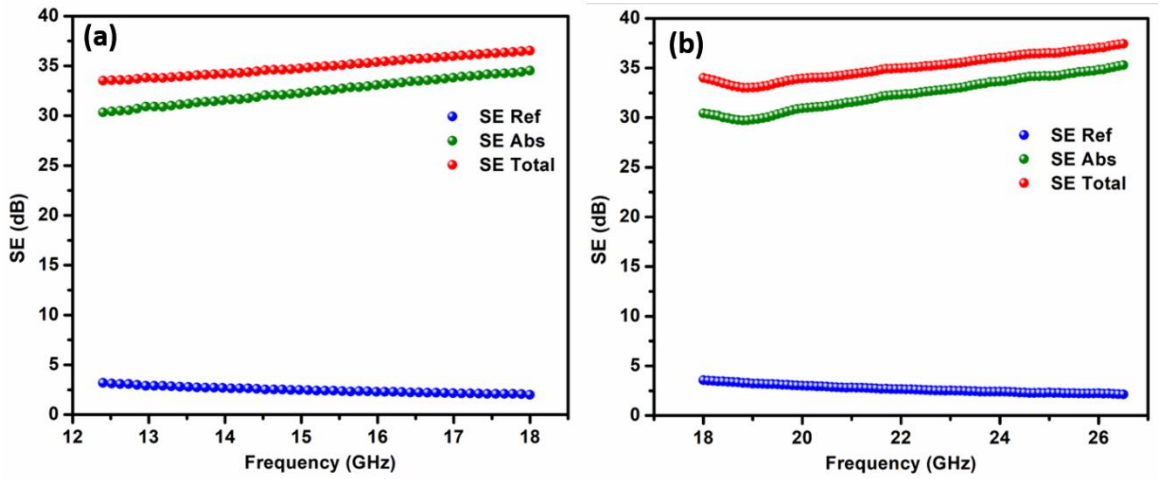

*Figure **3.10** Frequency variation of the SE_{Abs}, SE_{Ref}, and SE_{Total} of VP 30 in (**a**) Ku and (**b**) K bands.*

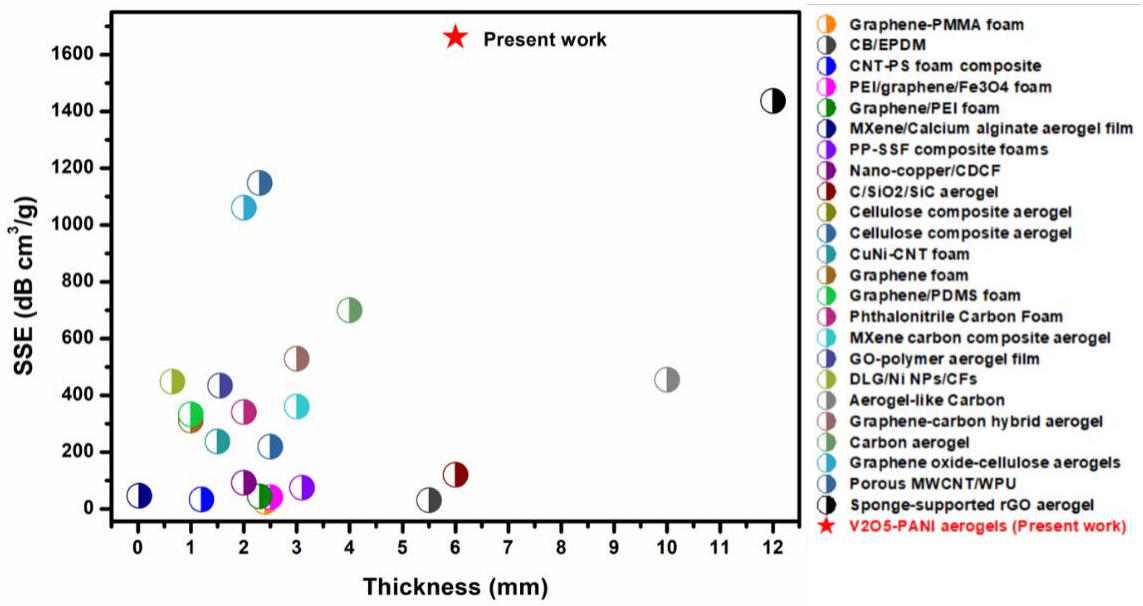

*Figure **3.11** Comparison of EMI shielding performance of VP aerogels with the reported porous materials. SE/density (SSE) versus the thickness of different materials. References in the graph are given in Table 3.1.*

Further, the shielding efficiency of the VP 30 aerogel was examined in both Ku (12.4-18 GHz) and K bands (18-26.5 GHz) of the electromagnetic spectrum. The sample thickness in Ku and K bands is 6 mm and 4 mm. The shielding values could reach up to a maximum of 36.54 dB and 40.97 dB in Ku and K bands, respectively (figures 3.10a& b). Absorption shielding varies from 30.33 dB to 34.43 dB, and reflection falls below 3.6 dB in the Ku band. Absorption shielding efficiency reaches 38.8 dB at 26.5 GHz, which is expected since the absorption loss increases as a function of frequency. The specific shielding effectiveness of the VP 30 has maxima of 1740 dB cm^3/g in the Ku band and 1951

dB cm^3/g in the K band. The corresponding thickness normalized SSE (SSE/thickness) are respectively 2900 and 3252 dB cm^2/g.

Figure 3.11 gives a graph indicating the SSE values versus the thickness of various porous EMI shielding materials reported in the literature compared with V_2O_5-PANI aerogels. Only a few studies reported on carbonless aerogels as efficient microwave absorbers. In contrast, most materials use either carbon in some form or MXene, which all have cumbersome synthesis processes. The green absorber reported here could be the one with a lightweight, cost-effective EMI shield, synthesized with very few chemicals through a simple procedure. This comparison strongly indicates that these V_2O_5-PANI aerogels have immense potential as light, green, and high-power microwave absorbers. Table 3.1 summarises some of the previously reported works on porous foams/aerogels and their corresponding attenuation efficiency, along with the thickness and their specific shielding performance at the X-band frequency range. The reported values show that the fabricated aerogels are potential candidates for avionic and space EMI shielding applications due to their exceptional specific shielding values.

Figure 3.12a schematically illustrates the detailed shielding mechanism across the aerogel samples. Firstly, part of the incoming waves is reflected at the interface between VP 30 and air because of their impedance mismatch while the remaining travels into the sample. The array of nanowires in the V_2O_5 dispersion, which acts as an effective substrate for polymerizing aniline, forms a three-dimensional conducting network. The presence of polymer makes these nanowires closer together to form more conducting layers. The connected network of wires in layers helps to shield the waves emanating through the aerogel. The folds in individual layers and space between the layers of aerogel trap and attenuate the entered electromagnetic waves by reflection, multiple absorption, and scattering.

High absorption and low reflection towards incident EM waves make the aerogels green EMI shields. The shielding material's green index (g_s) is calculated using equation 3.2 (D. Zhang *et al*., 2019).

$$g_s = \frac{1}{{S_{11}}^2} - \frac{{S_{21}}^2}{{S_{11}}^2} - 1 \tag{3.2}$$

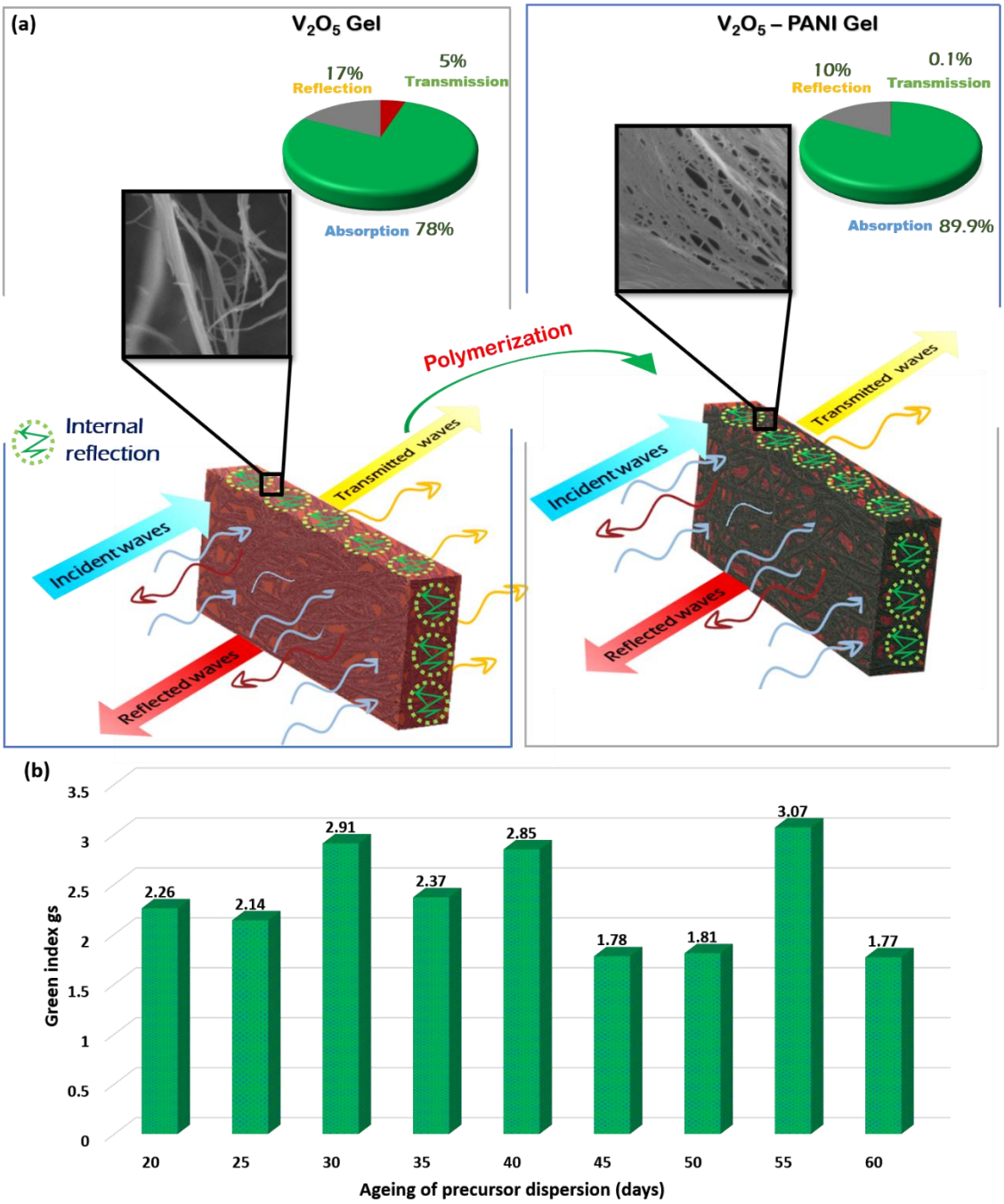

*Figure **3.12** (**a**)A schematic illustration of the EMI shielding mechanism, (**b**)green index (g_s) of V_2O_5-PANI aerogels prepared with different aging.*

The greater the value of g_s, the greener the shielding material. Figure (3.12b) presents the values of the green index of aerogels with various aging periods. All the aerogel samples have a green index greater than 1, indicating green EMI shielding. Good impedance matching of aerogels helps easily transmit EM waves through the shield, reducing the reflection loss. The closer the impedances of shield and EM waves, the minimal the reflection. The impedance of conducting materials is low; hence, the impedance mismatch

with incoming electromagnetic waves gives rise to more reflection (Tong, 2008). Here, the lower conductivity of aerogels favors the green shielding, and at the same time, the porous nature enhances the total shielding efficiency by higher EM wave absorption. Also, the absence of carbonaceous fillers and other metallic nanostructures makes the samples eco-friendly. Hence this V_2O_5 -PANI aerogel prepared by a very simple strategy could be used as an efficient green, lightweight EM wave absorber.

3.4 Conclusions

From aeronautics to portable electronics, lightweight and robust electromagnetic interference, shielding materials are in huge demand. In this work, we demonstrate that without employing 2D materials like graphene or MXene, cost-effective oxides like V_2O_5 could be used for generating green, robust EMI shielding aerogels with an impressive performance in the X-band. The fabrication of shielding material follows a simple and economical route. The V_2O_5-PANI composite hydrogel was primarily prepared by simultaneous polymerization and gelation of V_2O_5 nanowire dispersion with aniline monomer. The V_2O_5 nanowire network acts as a 3D skeleton as well as an excellent oxidizing agent for polymerization. After gelation, the hydrogel was freeze-dried to form V_2O_5 -PANI aerogel, to yield maximum microwave attenuation. The present research reveals that using the current strategy of controlled storing conditions of V_2O_5 dispersion, we can tune the shielding performance via tailoring the nanowire growth. Remarkable shielding efficiency of 34.74 dB at X band was achieved for the CPC aerogel with the aging of 30 days. Interestingly, the EMI SE of the V_2O_5 -PANI composite shows a 50% increase over that of the sample without polymer. The high shielding is corroborated by visible improvement in electrical conductivity from 2.6×10^{-3} to 1.69×10^{-2} S cm^{-1} and the surface area of the mesoporous samples. The growth of the 3D porous network structure made the density of aerogel as low as 20.0 mg/cm^3, and hence, the specific shielding efficiency of V_2O_5 -PANI aerogel achieved a high value of 1662.2 dB cm^3 g^{-1} in the X band. The EMI SE achieved ~41 dB in the K band at a thickness of 4 mm with a thickness normalized SSE of 3252 dB cm^2/g. These robust but ultra-lightweight aerogels could be used as efficient EMI shields in portable gadgets and avionic devices.

Chapter 4

Acid Polymerized V_2O_5-PANI Aerogels with Improved EMI SE

- Acid polymerized, mechanically robust aerogels of V_2O_5- PANI with high electrical conductivity (4.4 S/cm) is reported.
- Ultra-light aerogels (density = 0.03 g/cm^3) have absorption dominant shielding and broad band width.
- Polymerized aerogels display impressive SE of 68.1 dB and SSE of 2196.8 dB cm^3/g in the X band.
- EMI SE reaches 86.1 dB in the K band with an excellent SSE/thickness of 9258.1 dB cm^2/g.

4.1 Introduction

In the construction of aerogel shields, the choice of the conductive polymer and apt matrix is highly critical. The previous chapter (chapter 3) investigation provided vital clues about the microwave attenuation of V_2O_5-PANI aerogels. Polyaniline (PANI) is a noble candidate from the conducting polymers with low density, good chemical stability, and tunable conductivity (W. Huang *et al*., 1986). Several reports, including our own investigation, proved that PANI is an excellently lossy microwave absorbing material with good environmental stability (Gopakumar *et al*., 2018; J. Liu *et al*., 2019; K. Zhou *et al*., 2018). Although PANI can be produced cheaply and effortlessly, achieving high conductivity in them is challenging since the synthesis conditions largely affect the morphology and properties of PANI (Karatchevtseva *et al*., 2006; J. Liu *et al*., 2019). Several researchers have studied different polyaniline composites for shielding purposes because of their conducting nature (Huangfu et al., 2019; Joseph et al., 2015, 2016). Wang *et al.* prepared polyaniline/graphene aerogels using the hydrothermal technique and found their shielding capacity to be 42.3 dB for 3 mm thick samples (Y. Wang *et al*., 2019). Recently, Zhang *et al.* prepared an integrated leather solid waste/poly(vinyl alcohol)/polyaniline aerogel to show an EMI shielding effectiveness of more than 40 dB (T. Zhang *et al*., 2021).

As the previous chapter shows, conducting polymers combined with layered semiconducting oxides can lead to promising electrical transport properties. Few reports in the literature present V_2O_5-based aerogels as excellent microwave absorbers. In this regard, ours was the earliest effort to develop V_2O_5-based green EMI shielding gels, owing to their less environmental hazard resulting from the effective attenuation of spurious waves with minimal secondary reflection(Puthiyedath Narayanan *et al*., 2021). We later realized that the shielding performance of V_2O_5-PANI composite aerogels could be maximized if the in-situ polymerization of the conducting polymer is completed, which is possible only in a strong acidic environment.

In the present study, microstructure engineered V_2O_5-PANI composite aerogels were prepared using a facile, in-situ oxidative polymerization in the presence of hydrochloric acid. The structure, morphology, thermal stability, electrical conductivity, and

electromagnetic shielding properties were examined, and we got the highest EMI shielding for V_2O_5-PANI composite aerogels reported in the literature.

4.2 Experimental

4.2.1 Materials

Ammonium metavanadate (99%) was purchased from Sigma-Aldrich Co., USA. Aniline and hydrochloric acid (HCl 37%) were obtained from Merck Life Science Private Limited, Mumbai. All the chemicals were used as received without any further treatment.

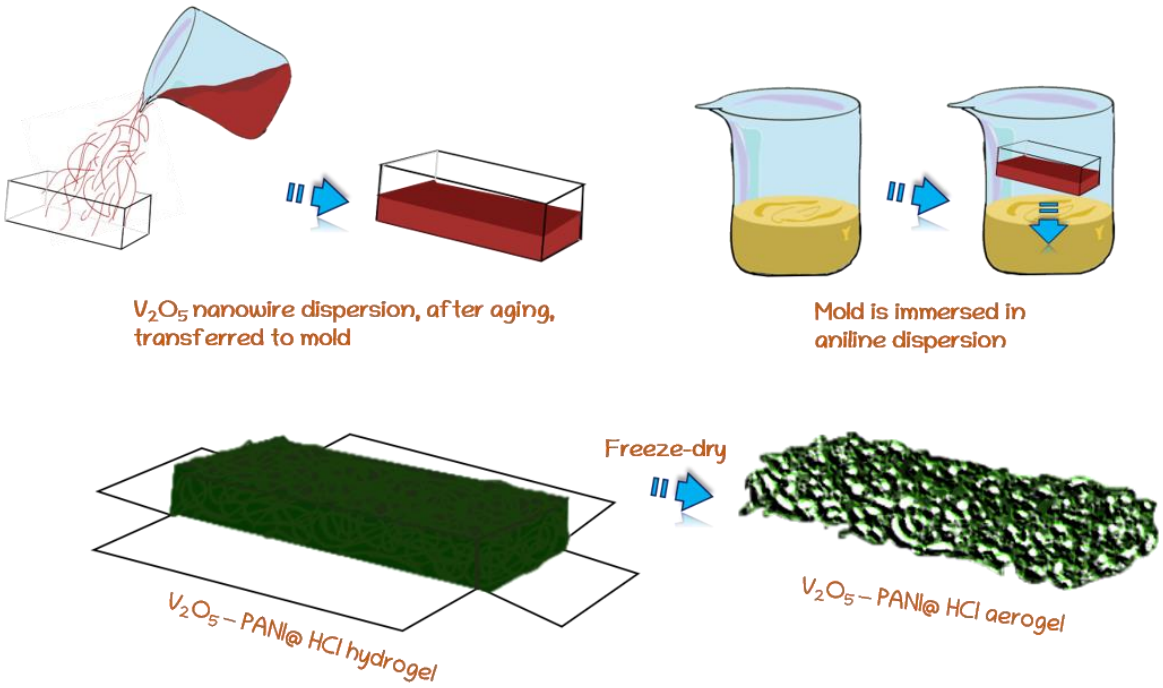

*Figure **4.1** Schematic illustration of the fabrication of V_2O_5-PANI@HCl aerogel*

4.2.2 Synthesis of V_2O_5 – PANI@ HCl aerogels

Herein, V_2O_5 – PANI@ HCl hybrid hydrogels were fabricated employing simple and effective in-situ polymerization of V_2O_5 nanowire dispersion (figure 4.1). Hydrated vanadium pentoxide with layered microstructure in well-dispersed form was prepared through the same procedure as in chapter 3. Similar to the same process, the prepared dispersions were kept undisturbed for 15-60 days to investigate aging-dependent shielding properties. Meanwhile, pure V_2O_5 aerogel was also prepared by direct freeze-drying of this dispersion for comparison.

To prepare hybrid hydrogel, aniline monomer was dispersed in dilute HCl (0.25 and 1 M), and V_2O_5 nanowire dispersion took in a mold was immersed in it. Gelation and polymerization were allowed to happen simultaneously at room temperature. Hydrogels were formed within a few hours and were freeze-dried at -100 ºC for 48 hours to obtain final aerogels. Hereafter, pure V_2O_5 aerogel and V_2O_5 -PANI@ HCl hybrid aerogel samples with the highest EMI SE were coded as VHA and VPHA, respectively.

4.2.3 Characterization

The hydrogels employed in this investigation were freeze-dried using Scanvac Cool Safe Pro 110-4, M/s. Labogene, Denmark at -110°C. High-resolution transmission electron microscopy (HRTEM) (FEI Tecnai G2 30S-TWIN, FEI Co., Hillsboro, OR, USA) and field emission scanning electron microscopy (FESEM) using an FEI-Nova Nano SEM 450 (beam potential of 10 kV) were used to observe the microstructure and morphology of the surface of the sample. V_2O_5 precursor (VHA) and V_2O_5-polyaniline composites (VPHA) were characterized with a Perkin Elmer Series FT-IR spectrum-2 Fourier-transform infrared (FT-IR, ATR mode) spectrometer, confocal Raman microscope (α-300R WITec, Inc., Germany), Wide-angle X-ray diffractometer (XEUSS SAXS/WAXS system using a Genixmicro-source from Xenocs operated at 50 kV and 0.6 mA) and a PHI 500 Versa Probe 2 X-ray Photoelectron Spectroscope (Al Kα radiation). Thermal decomposition was studied by a thermogravimetric analyzer (STA 7300, Hitachi, Japan) at a heating rate of 10°/min from 25 to 650°C under air atmosphere. The surface area was measured using the Brunauer–Emmett–Teller (BET) method, using a nitrogen adsorption-desorption isotherm (Gemini 2375, Micromeritics, Norcross, USA). The pore size distributions of the aerogels were measured using the Barrett–Joyner–Halenda (BJH) method. The DC conductivity of the samples was recorded by the four-probe method using Keithley 2450 source meter. The electromagnetic characterization of the V_2O_5 and V_2O_5-PANI@ HCl composite aerogels was measured using a rectangular transmission waveguide technique, with a Keysight PNA-L network analyzer N5234B, at X band (8.2-12.4 GHz), Ku (12.4-18 GHz) and K band (18-26.5 GHz) of the microwave frequency range, at room temperature. All samples were precisely machined into 3 mm thick rectangular blocks suiting exactly with the inner slot dimensions of the waveguide sample holders; 22.8 mm x 10.1 mm for X, 15.79 mm x 7.89 mm for Ku, and 10.67 mm x 4.32 mm for K bands.

4.3 Results and discussion

One-dimensional nanostructures such as nanowires have been gaining attention as indispensable functional components in communication nanodevices due to their dimensionality and quantum confinement effect (Dubal *et al*., 2011). In the present work, as prepared V_2O_5 nanowires in precursor were aged for more than 15 days to attain ultra-long nanowires through oriented homogeneous nucleation of polyaniline units. The cluster of these lengthy hydrated nanowires plays a prominent role in forming free-standing sheets that construct the skeleton of composite hydrogels. Polycondensation of ammonium metavanadate in dilute HCl at room temperature sets ion exchange between NH_4^+ and H^+ ions, and hydrated V_2O_5 nanowires of length >10 μm were formed with a storage time of >15 days (Xiong *et al*., 2008). As the previous chapter shows, the nanowire growth mechanism can be oriented attachment (OA) in the colloidal state. In this model, adjacent nanostructures self-organize by the coalescence of solid particles. Nanocrystals in the colloidal dispersion collide with each other, and an effective collision between particles with common crystallographic orientation leads to an irreversibly oriented attachment (Dalmaschio *et al*., 2010; M. Li, Kong, *et al*., 2011). As shown in Figures 4.2 a & b, the as-prepared V_2O_5 dispersion has a nanobelt-like morphology with a length <1 μm. Nanowire growth continues through self-assembling interactions among 1D structures in a well-dispersed colloidal state. Here, the nanobelts imbricate and attach to each other (see figure 4.2b) to form high aspect ratio nanowires (Dalmaschio *et al*., 2010).

The preparation method adopted in the present investigation is briefed in figure 4.1. After introducing vanadium salt into the acid-water mix, the solution turned yellow, and increased coordination shifted the color to crimson red. Aging for optimal duration brought about a sufficiently thick V_2O_5 precursor dispersion comprised of robust nanowires. The dispersion was taken in a mold and immersed in the aniline-acid solution. We could observe the pretty rapid formation of the gel. An earlier report suggests that polymerization of the aniline monomer is highly efficient only in the presence of a protonic acid (Golba *et al*., 2020). Here, HCl acts as a strong polar solvent that plays a critical role in assembling the polyaniline nuclei, leading to the direction-oriented fiber structure by suppressing secondary growth. Further, owing to the strong oxidizing ability of V_2O_5, the aniline monomers are readily polymerized in the vicinity of hydrochloric acid, simultaneously with gelation. Finally, the trapped liquid within the continuous three-dimensional oxide skeleton

of nanocomposite hydrogel is carefully removed to obtain low-dense homogenously constructed hybrid aerogels. It is believed that the high degree of polymerization of the conducting polymer within the layered oxide network supplements the aerogels' electron transport and microwave attenuation characteristics.

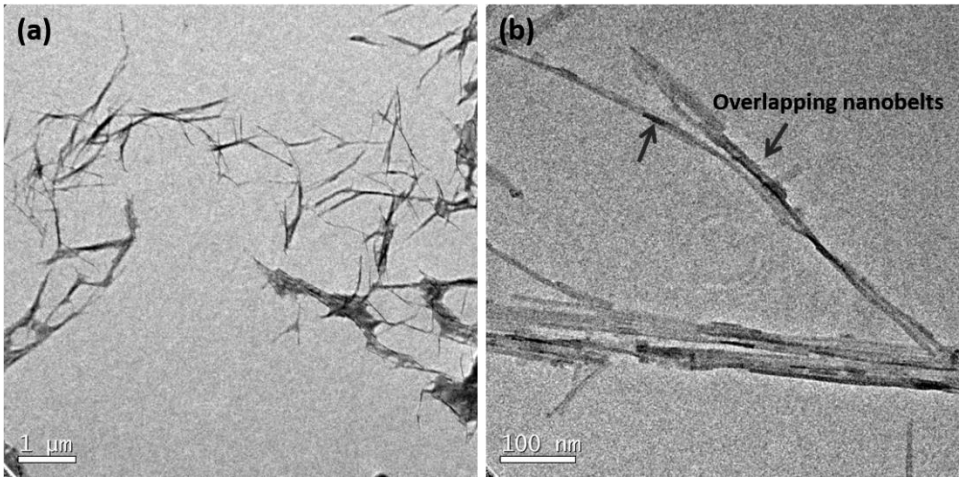

*Figure **4.2** (**a**&**b**) TEM images of as-synthesized V_2O_5 precursor dispersion at different magnifications; The arrows point to the overlapping of nanobelts to form longer nanowires.*

Figure 4.3a shows the photographic image of a lightweight VPHA aerogel. FESEM image of VHA in Figure 4.3b shows a flake-like microstructure of V_2O_5 aerogel. The high-magnification reveals that each flake is constructed with several microns long intertwined nanowires of width <50 nm. Meanwhile, the morphology of polymerized aerogels VPHA (figure 4.3d-f) drastically varies from that of the VHA aerogels. They possess an impressively homogeneous and meso-macroporous microstructure that provides vast space for scattering and internal reflections of incident EM waves. The detailed scanning electron microscopy reveals that the aerogels have a dual pore-like structure with the big pores that form with the sublimation of ice having the dimension of 1-3 µm, whereas the smaller pores that form between the nanowires have a diameter between 100 and 500 nm. The aerogel possesses an open cellular construction of interconnected pores created through triangular or quadrangular junctions. Recently reported rGO@FeNi/Epoxy composites exhibited a high EMI SE of 46 dB mainly due to their regular honeycomb-like microstructure (P. Song *et al.*, 2022). Hence, the regularly ordered porosity created in VPHA aerogels is also expected to contribute to good shielding properties.

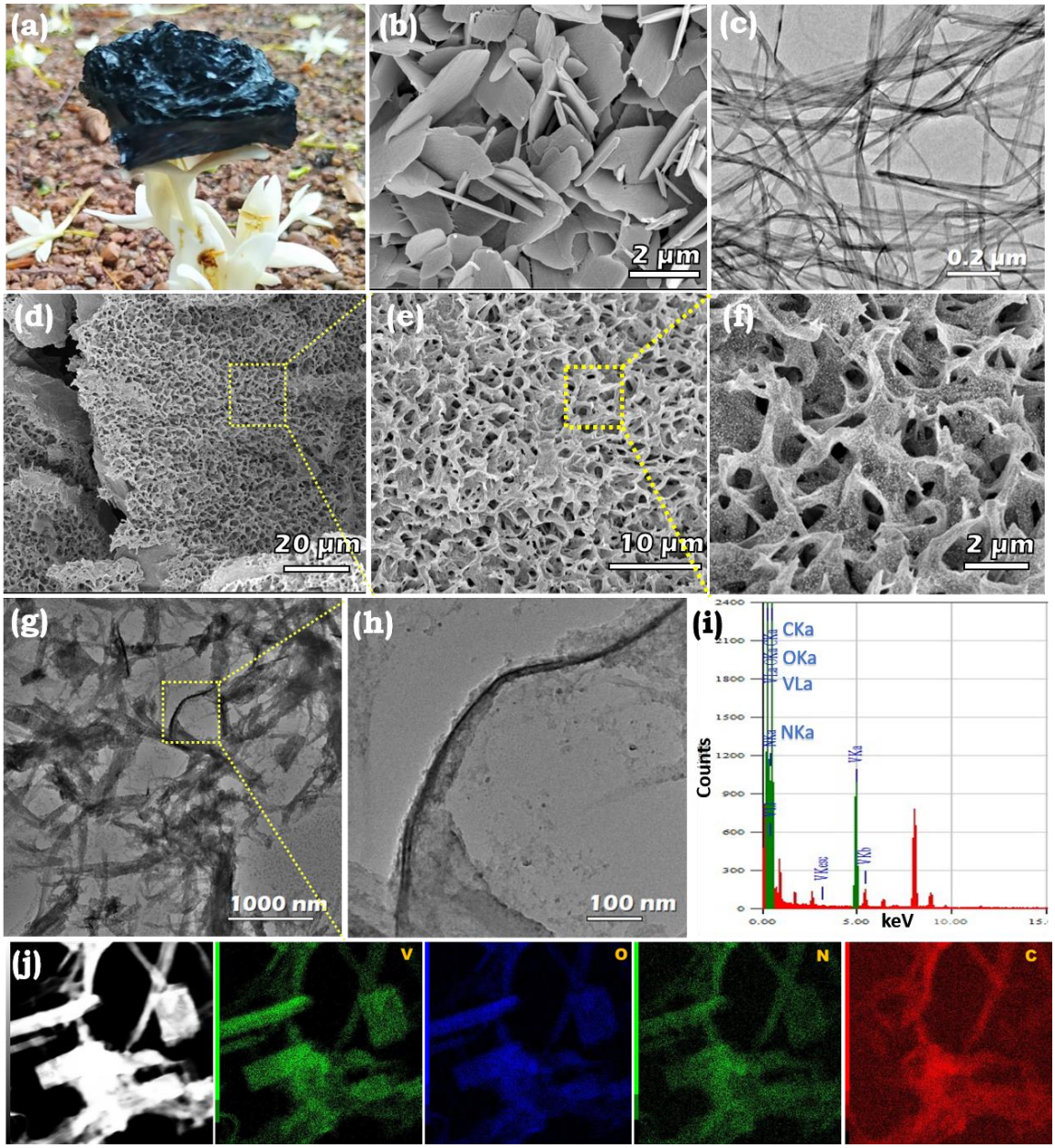

*Figure **4.3** (**a**) VPHA aerogel resting on a flower. (**b**&**c**) FESEM and TEM images of VHA aerogels (**d**, **e**, &**f**) FESEM images of VPHA aerogels at different magnifications (**g**&**h**) TEM images of VPHA aerogels at different magnifications. (**i**) EDS spectrum of VPHA, (**j**) elemental mapping of VPHA.*

TEM images were recorded to unveil the fine structures of aerogels further. It can be seen from Figure 4.3c that VHA consists of ultra-thin nanowires of a high aspect ratio. The diameter of the nanowires in VHA is typically around 10 nm. VPHA composite aerogels also emulate the nanowire morphology of VHA. The well-maintained nanowire morphology of the composite indicates that the hydrated vanadium pentoxide nanowires were uniformly coated and reinforced by polyaniline. After polymerization, the V_2O_5 NWs

tend to form a bunch with their bundle diameter ranging between 50 to 60 nm. Figures 4.3g & h clearly show that the NWs are distinctly flexible, with some even circularly bent. Such microstructure is of great significance for microwave attenuation. This is because interfaces and voids inside the porous microstructure provide vast surface area for the incidence of electromagnetic waves and thus intensify the microwave absorption performance by multiple reflections (Y. J. Wan *et al*., 2017; Zeng *et al*., 2016). Moreover, the nanowires are bound together, forming a well-connected conductive network. This peculiar structure of VPHA composite, made of hierarchically porous layered morphology of polygonal comb-like microstructure with substantially connected layers at the microscale, bent and folded to form conductive aerogel at the macroscale, is expected to enhance the overall EMI shielding performance. The formation of a more connected and conducting skeleton is supplemented by electron transport of the conducting polymer due to the delocalization of π electrons, which can also contribute to the shielding ability. EDS spectrum of the composite gel (figure 4.3i) clearly indicates the presence of polymer. The claim of uniform polymer coating on the layered oxide is further supported by the chemical mapping spectra of VPHA that show a more or less uniform presence of elements V, O, C, and N (figure 4.3j).

The crystalline structure of all as-synthesized samples was investigated by wide-angle X-ray diffraction (WAXD) (figure 4.4a). Only a few Bragg reflections are visible in the WAXD spectrum, pointing to the amorphous nature of gels. The peaks of the V_2O_5 precursor match with the layered orthorhombic structure of hydrated vanadium pentoxide. Peaks observed at 2θ values of 15.3º, 21.6º, 26.4º, 30.5º, and 31.6º are attributed to (200), (101), (110), (301), and (011) reflections (Abd-alghafour *et al*., 2016). Intercalation of polymer ends up in a much more amorphous material, as evident in Figure 4.4a. The absence of changes in composite peaks after polymerization compared with VHA indicates that the precursor's layered structure is well maintained.

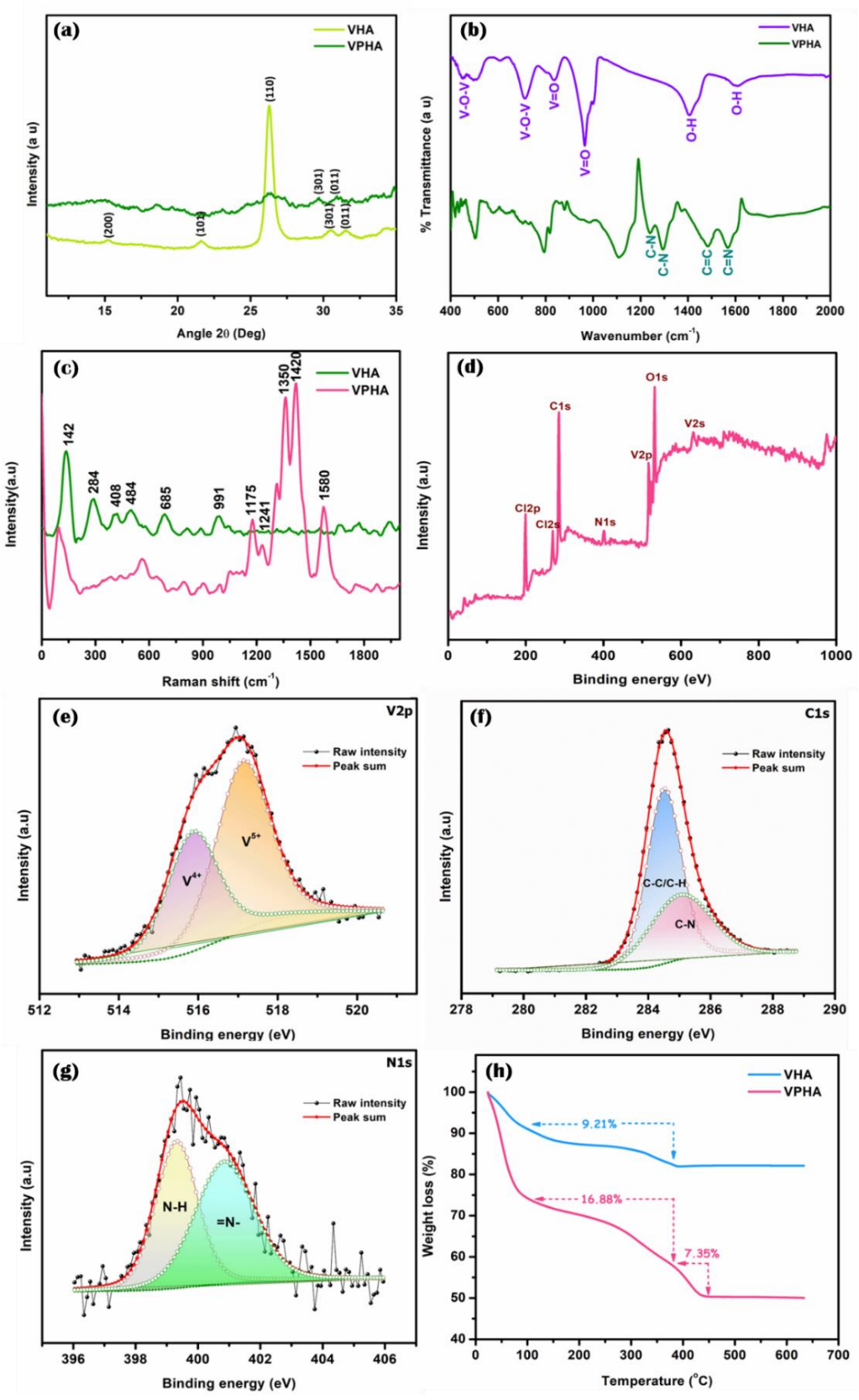

*Figure **4.4** (**a**) WAXD pattern, (**b**) FTIR spectra, and (**c**) Raman spectra of VHA and VPHA aerogels (**d**) XPS survey spectrum of VPHA aerogel High-resolution XPS spectra of (**e**) V2p, (**f**) C1s, (**g**) N1s in VPHA aerogel, and (**h**) TGA of VHA and VPHA aerogels*

The formation of hybrid V_2O_5- PANI@ HCl aerogel was authenticated by Fourier transform infrared (FTIR) analysis (figure 4.4b). The peaks in the FTIR spectra of VHA around 450 and 714 cm^{-1} are assigned to the V-O-V stretching mode's asymmetric and symmetric stretching bands (Mukhtar *et al*., 2017). The peak at 836 cm^{-1} is attributed to the coupled vibration V=O and V-O-V (Derkaoui *et al*., 2017). The strong peak at 964 cm^{-1} corresponds to the terminal symmetric stretching band of oxygen in the V=O bond (Mukhtar *et al*., 2017). The narrowband at 1606 cm^{-1} is due to stretching vibrations of the water molecule (Cao *et al*., 2013). The characteristic peaks ranging from 1000 to 1800 cm^{-1} confirm polyaniline formation. The bands at 1565 and 1484 cm^{-1} are attributed to ring stretching of quinoid and benzenoid form in PANI, C=N, and C=C, respectively. The bands related to the C−N stretching of an aromatic amine appear around 1298 and 1237 cm^{-1}. Besides, the band near 1110 cm^{-1} has been attributed to electronic-like absorption of N=Q=N (Q denotes the quinoid ring) stretching mode (John *et al*., 2010). Also, the weaker V=O bonds in V_2O_5- PANI@ HCl aerogel indicate the polymer's intercalation into the V_2O_5 matrix.

Raman spectrum of aerogels was taken at room temperature in the wavenumber range of 100–2000 cm^{-1} (see figure 4.4c). The peaks of pure V_2O_5 aerogel are symmetric with the reported Raman modes for $V_2O_5.nH_2O$ (Abd-Alghafour *et al*., 2020; Londoño-Calderón *et al*., 2010). The dominant peak at 142 cm^{-1} corresponds to V-O-V chain vibrations. The two peaks at 284 and 408 cm^{-1} are associated with the bending vibration of the V=O bonds, and the one at 991 cm^{-1} is assigned to the V=O stretching vibrations (Londoño-Calderón *et al*., 2010). The peaks located at 484 and 685 cm^{-1} are assigned to V-O-V bending and stretching modes, respectively (Abd-alghafour *et al*., 2016). The presence of protonated polyaniline is manifested by the Raman bands in the wavenumber range of 1000 to 1700 cm^{-1}. The peak observed at 1175 cm^{-1} can be assigned to the C-H in-plane bending vibrations of aromatic rings. Raman bands at 1241 and 1420 cm^{-1} are set to the C–N stretching mode(Morávková & Dmitrieva, 2017; Rohom *et al*., 2014). The band around 1350 cm^{-1} is attributable to $C–N^+$ vibrations of polaronic structures in PANI (Rohom *et al*., 2014). The band at 1580 cm^{-1} is related to C=C stretching vibrations in a quinonoid ring (Stejskal *et al*., 2015). Therefore, the FTIR and Raman results are consistent with the polymerization of polyaniline over hydrated V_2O_5 nanowires, which is in good agreement with the SEM and TEM observations.

X-ray photoelectron spectroscopy (XPS) characterization is conducted to study the surface composition and chemical structure of the obtained V_2O_5-PANI@ HCl aerogels. The XPS survey scan (figure 4.4d) revealed the presence of nitrogen (N), oxygen (O), vanadium (V), chlorine (Cl), and carbon(C) in the nanocomposite aerogel. The high-resolution XPS of $V2p_{3/2}$ and $V2p_{1/2}$ peaks states can be fitted by two different electronic states of V^{5+} and V^{4+}. Figure 4.4e shows the deconvoluted $V2p_{3/2}$ binding energies with V^{5+} located at 517.2 eV and V^{4+} at 515.9 eV. The broad peak centered at approximately 530 eV is assigned to oxygen present in the lattice. The XPS peak due to the carbon backbone of PANI at ~285 eV can be deconvoluted to two prominent peaks. The peak at 284.5 eV corresponds to C–H/ C–C functional carbon of the quinoid ring, and that at 285.0 eV is attributed to C-N (figure 4.4f). N1s region of the composite gels can be deconvoluted into two synthetic peaks, consistent with the typically reported values for benzenoid amine (399.4 eV) and quinoid amine (400.9 eV) (figure 4.4g) (Patil *et al*., 2018; Waghmode *et al*., 2017). The chlorine peaks in the survey spectrum indicate that hydrochloric acid's presence during the gelation enhances the degree of polymerization. Further, it also suggests that a part of HCl gets doped into the composite aerogel.

The thermal decomposition of as-synthesized aerogels was analyzed by thermogravimetric analysis (TGA), as depicted in figure 4.4h. The TGA profile of pure $V_2O_5.nH_2O$ aerogel shows two-step weight loss as a function of temperature. The initial weight loss below 100 ºC was attributed to the evaporation of physisorbed water and the other volatile matter retained in the aerogels. The second weight loss of 9.21%, witnessed in the range of 100-390 ºC, is attributed to the loss of water bound to vanadium sites exposed to the interlayer region and crystallization to orthorhombic vanadium pentoxide (Huguenin *et al*., 2000). In composite aerogels, the weight loss in this second step is increased to 16.88%. The extra loss is due to the simultaneous decomposition of polymer and removal of strongly bonded water. In addition to these two weight loss steps, V_2O_5-PANI composite sample shows a third significant weight loss of 7.35% after 450 ºC. This was attributed to the thermo-oxidative decomposition of polyaniline (Hasan *et al*., 2015). The plateau above 450 ºC in the TGA diagrams indicates the approximate amount of V_2O_5 in the composite aerogels, corresponding to 82.2 wt% for pure V_2O_5 aerogel. Clearly, the weight percentage of V_2O_5 in the hybrid aerogels after thermal treatment is lowered to 50.2%, indicating the presence of polyaniline. In this way, a high degree of polymerization improves the thermal stability of the aerogel.

Textural properties of the aerogels were studied using N_2 adsorption−desorption isotherms (figures 4.5a & b). At low relative pressure, only a small volume of nitrogen gas was adsorbed by the aerogels VHA and VPHA, and the gels consisted of mostly small mesopores (2–50 nm) (insets of figures 4.5a & b). Moreover, the adsorption isotherm of pure V_2O_5 aerogel features a relatively low specific surface area of 8.84 m^2/g. However, the BET surface area of the polymerized sample is about 24.67 m^2/g. The high surface area provides more space for scattering and internal reflection of incident EM waves and thus can support absorption dominant shielding.

Figure 4.5c shows the electrical conductivities of aerogels aged 15-45 days. Polymerization in the presence of acid endows VPHA aerogels with 2150 times higher conductivity (~4.3 $S.cm^{-1}$) than pure V_2O_5 aerogel (0.002 $S.cm^{-1}$). It is known that the electrical conductivity of PANI composites varies at different pH values. Mohsin *et al*. reported that the electrical conductivity value increases with a decrease in the pH of the solution (Ali Mohsin *et al*., 2020). The treatment of monomer with a highly oxidizing template of V_2O_5 in the presence of HCl accelerates the polymerization rate and leads to preferential protonation. This increases the number of polaron in the polymer chain and their mobility, thereby boosting conductivity values. High conductivity along with increased connectivity is a rare combination for porous materials, and it can endow the aerogels with supreme shielding efficiency.

The ultra-low density of these aerogels is also quite striking (figure 4.5d). Notably, the pure V_2O_5 aerogels have a very low density, measured to be ~20.0 mg/cm^3. With the incorporation of polyaniline, the density is slightly increased to ~31.0 mg/cm^3. However, the acid polymerization reinforces the aerogel architecture. In this regard, the weight-bearing capacity and structural stability of VPHA were qualitatively examined. For this, an as-prepared VPHA but machined aerogel block of dimension $2 \times 2 \times 0.5$ cm^3 (approximate weight ~850 mg) was periodically loaded with standard weights. It was found to hold weight up to ~240g without any structural deformations. The well-retained three-dimensional porous structure without breaks confirms the better compressive strength of nanocomposite aerogel, much higher than that of pure V_2O_5 gel.

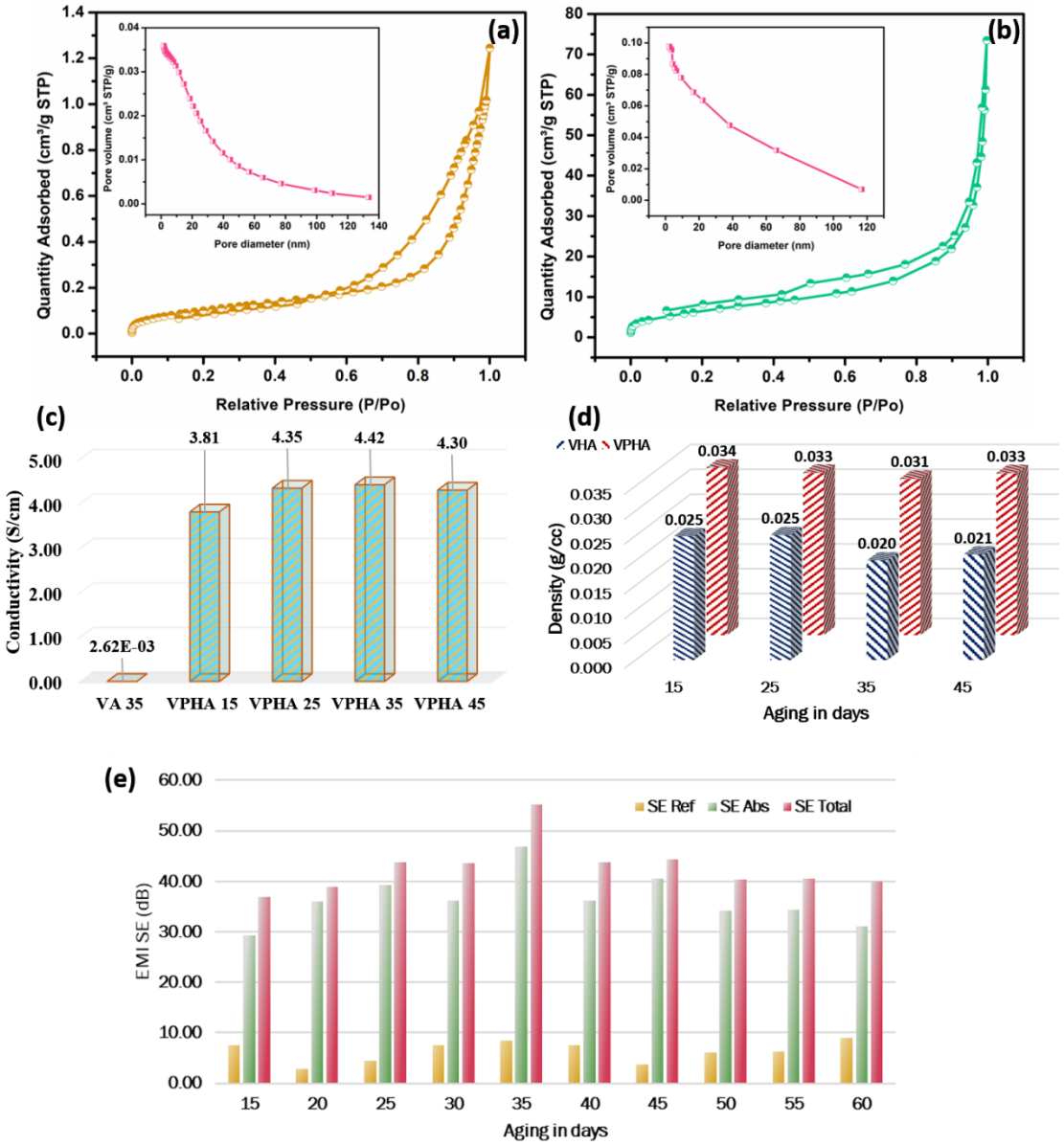

*Figure **4.5** N_2 adsorption-desorption isotherms of (**a**) VHA and (**b**) VPHA aerogels. (**c**) the electrical conductivity and (**d**) density of VHA and VPHA aerogels. (**e**) Total EMI shielding effectiveness (SE_{Total}), reflection shielding effectiveness (SE_{Ref}), and absorption shielding effectiveness (SE_{Abs}) of VPHA aerogels at 12.4 GHz at different storage days.*

To evaluate EMI shielding performance, S parameters of V_2O_5- PANI@ HCl aerogels were measured in the X-band range (8.2–12.4 GHz), where various medical electronic devices and communication systems work. The samples were machined to get a thickness of 3 mm. Reflection shielding effectiveness (SE_{Ref}), absorption shielding effectiveness (SE_{Abs}), and total EMI shielding effectiveness (SE_{Total}) of aerogels were calculated from S parameters. Here, SE_{Ref} is related to the relative impedance mismatch between the incident wave and shielding material, while SE_{Abs} is associated with the physical characteristics of the shield. The greater the impedance mismatch between the

incident wave and shielding material, the greater the reflection losses (Lalan *et al*., 2019). Shields with higher conductivity show strong reflection due to impedance conflict, leading to secondary EM wave pollution. But in the case of VPHA aerogels, the high volume of air pockets on the surface promotes suitable pairing of impedance and reduces the reflection loss. For non-magnetic samples, absorption loss originates mainly from the dielectric loss, composed of polarization and conductive loss (L. Wang *et al*., 2021). The formation of an electrically conductive network is crucial for imparting conductive loss. Thus, both SE_{Abs} and SE_{Ref} are intimately related to the shield's conductivity, frequency, permittivity, and permeability, as given in the following equations 4.1 and 4.2;

$$SE_{Abs} = -8.68\, t \frac{\sqrt{\pi f \mu \sigma}}{2} \tag{4.1}$$

$$SE_{Ref} = -10 \log \left(\frac{\sigma}{16 f \varepsilon \mu}\right) \tag{4.2}$$

where t, f, μ, ε, and σ are the shield's thickness, frequency, permeability, permittivity and total conductivity (M. Wang *et al*., 2021).

First, the time-dependent storage variation of EMI SE of composite aerogels polymerized in 0.25M HCl and aniline mixture was investigated in the X band. As shown in figure 4.5e, all the samples with an aging period of over 20 days are excellent electromagnetic shields, with EMI SE values exceeding 40 dB. This implies that the ultralight aerogels with a thickness of ~3 mm transmit less than 0.01% of the incident power throughout the X band frequency range. The highest SE_{Total} of V_2O_5- PANI@HCl aerogel reaches 55.2 dB (i.e., >99.9997% of the incident waves are shielded) with aging of 35 days (i.e., VPHA 35). The EMI shielding material should have strong absorption and weak reflection on qualifying as an ideal eco-friendly shield. It is clear from figure 4.5e that the absorption shielding effectiveness exceeds reflection shielding effectiveness by more than four times. For example, the absorption SE of VPHA 35 (46.8 dB) is nearly six times its reflection SE, while that of VPHA 45 (40.53 dB) is over ten times its reflection SE of 3.73 dB. Here, the number following the sample name indicates the number of storage days of V_2O_5 dispersion. Evidently, this absorption dominance makes VPHA aerogels green. Figure 4.6a shows the minimum and maximum values of total EMI SE in the X band frequency range, and figures 4.6b-d depicts the detailed variation of SE_{Abs}, $SE_{Ref,}$ and SE_{Total} with

frequency. All the gels have good SE with minor variance in the entire bandwidth, making them suitable for practical applications.

Figures 4.6 e&f depict the SE_{total}, $SE_{Abs,}$ and SE_{Ref} of V_2O_5 and V_2O_5- PANI@ HCl aerogels with 35 days of aging, in the frequency range of 8.2-12.4 GHz. Evidently, we can find that the shielding efficiency has been significantly enhanced with the HCl-assisted polymerization of V_2O_5. Impressive is to note that the total EMI SE value as high as 55.2 dB is achieved for VPHA 35 while specific shielding efficiency reaches 1780.6 dB cm^3/g. Both the samples VHA 35 and VPHA 35 show absorption dominant shielding performance with relatively low SE_{Ref} values. Shielding efficiency due to reflection falls below ~2.5 at 8.2 GHz for VHA 35 and gradually decreases to 1.02 dB as frequency increases. In the case of VPHA 35, SE_{Ref} varies from 10.65 to 8.36 dB towards the higher frequency, which is less than 20 % of the total shielding effectiveness. The Absorption shielding efficiency of VHA 35 varies between 7.2 and 7.8 dB, while that of VPHA 35 was significantly improved to values varying from 41.7 to 46.8 dB. The declining and inclining trends of absorption and reflection SE with frequency are evident from the direct relationship between frequency and respective shielding efficiency in equations 4.1 and 4.2. The sample VPHA 35 shows a minimum 52.4 dB shielding efficiency in the X-band, which can be translated as 99.9994 % of the incident waves are blocked. Hence the shielding of the presently developed polymer composite is impressive in the entire X band region, with a total SE achieved maximum of 55.2 dB at 12.4 GHz. The rise in shielding performance is obviously due to the porous morphology and more interlayer connections, resulting in higher polaron conduction that improves both conductivity and internal reflections. As seen before, the HCl doping in polyaniline enhances the conductive network inside the three-dimensional oxide network. Hence, the shielding is more effective in the composite than pure V_2O_5 aerogel.

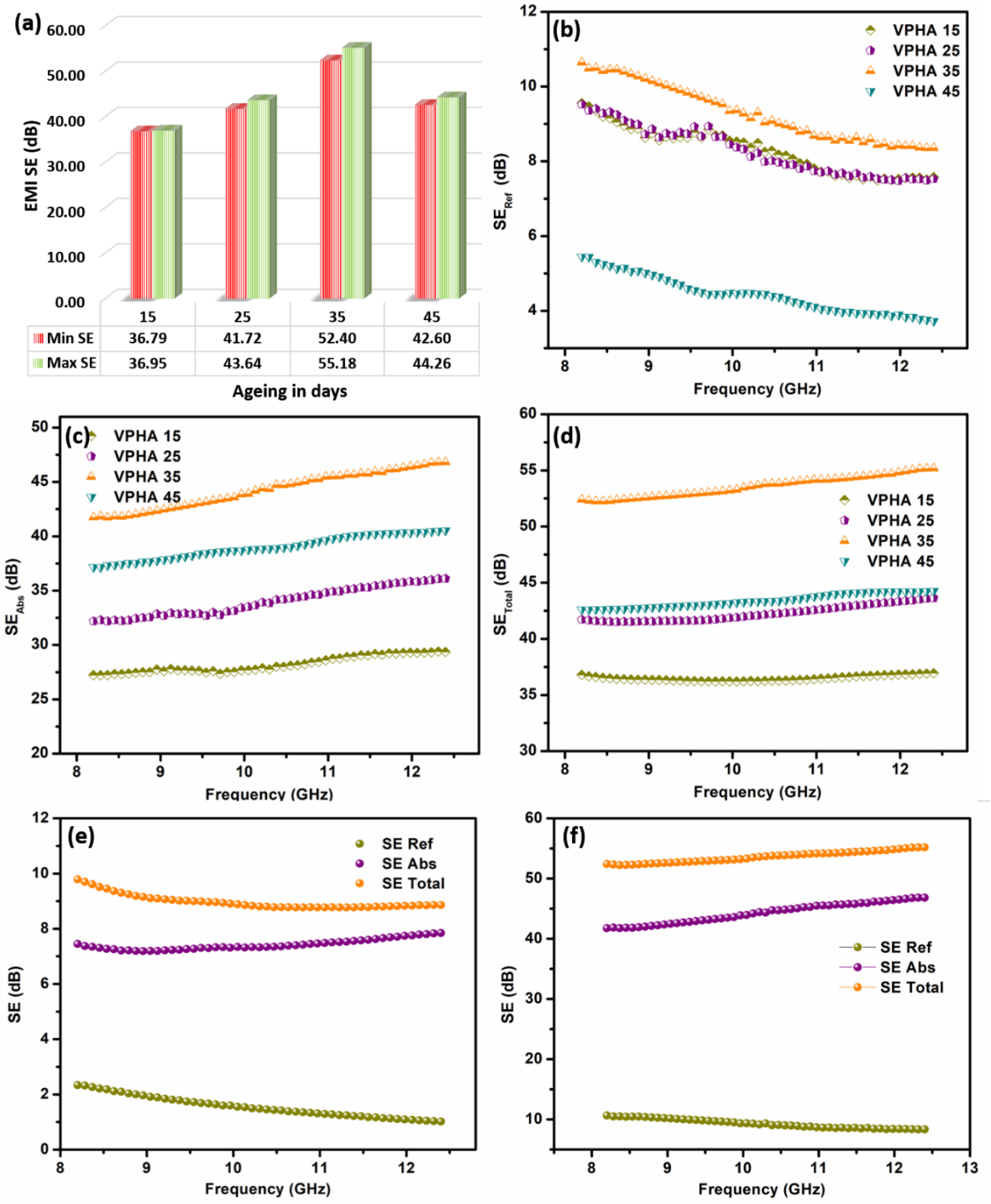

*Figure **4.6** (**a**) Minimum and maximum total SE of aerogels with different aging periods at X band frequency range, frequency variation of the (**b**) reflection shielding effectiveness (SE_{Ref}), (**c**) absorption shielding effectiveness (SE_{Abs}), and (**d**) total EMI shielding effectiveness (SE_{Total}) of VPHA aerogels (0.25M HCl) prepared with different aging, frequency-dependent variation of SE_{Total}, $SE_{Ref,}$ and SE_{Abs} of (**e**) VHA 35 and (**f**) VPHA 35 (0.25M HCl) over X band frequency range (8.2–12.4 GHz)*

Now, it became imperative to investigate the effect of acid concentration during polymerization and subsequent nucleation of gel, which was systematically studied by increasing the molarity of HCl in the aniline dispersion. Shielding performance of VPHA 35 with 1 M HCl (namely VPHA, and all the above characterization studies corresponds to this sample) in the X band is shown in figure 4.7a. We can find that the shielding efficiency has been enhanced with an increase in acid concentration during the polymerization of V_2O_5. As expected, VHA and VPHA show absorption dominant shielding performance with relatively low SE_{Ref} values. As shown, SE_{Ref} varies from 9.6 to 7.8 dB towards the higher frequency, which is actually less than 20 % of the total shielding effectiveness. Meanwhile, absorption shielding efficiency is significantly improved to the range 51.4 - 60.3 dB. Compared to VHA, VPHA has nearly eight times higher total SE. The sample VPHA shows a minimum of 61.0 dB and a maximum of 68.1 dB total shielding efficiency in the X-band, corresponding to 99.99992% and 99.99998% blocking of the incident waves, respectively. It is also remarkable that the specific shielding efficiency (SSE=SE/aerogel density) reaches 2196.8 dB cm^3/g. The conductance loss, a key parameter in determining EMI shielding performance, results from the movement of charges in the shield. The binding nature of polymer enhances the interconnections between the nanowires, whereas a high degree of polymerization eases the directional flow of charged particles (Park *et al*., 2010). When the concentration of acid increases at the time of polymerization, the degree of protonation (which largely depends on the pH of the solution) also increases (Ali Mohsin *et al*., 2020; Detsri & Dubas, 2009). The higher the extent of protonation, the greater the inter-chain charge transport in the form of polarons, which largely contributes to the conductivity of polyaniline. In a nutshell, improvement in electrical conductivity of the composite aerogel combined with the chemically engineered porous morphology magnifies the shielding efficiency of VPHA aerogels.

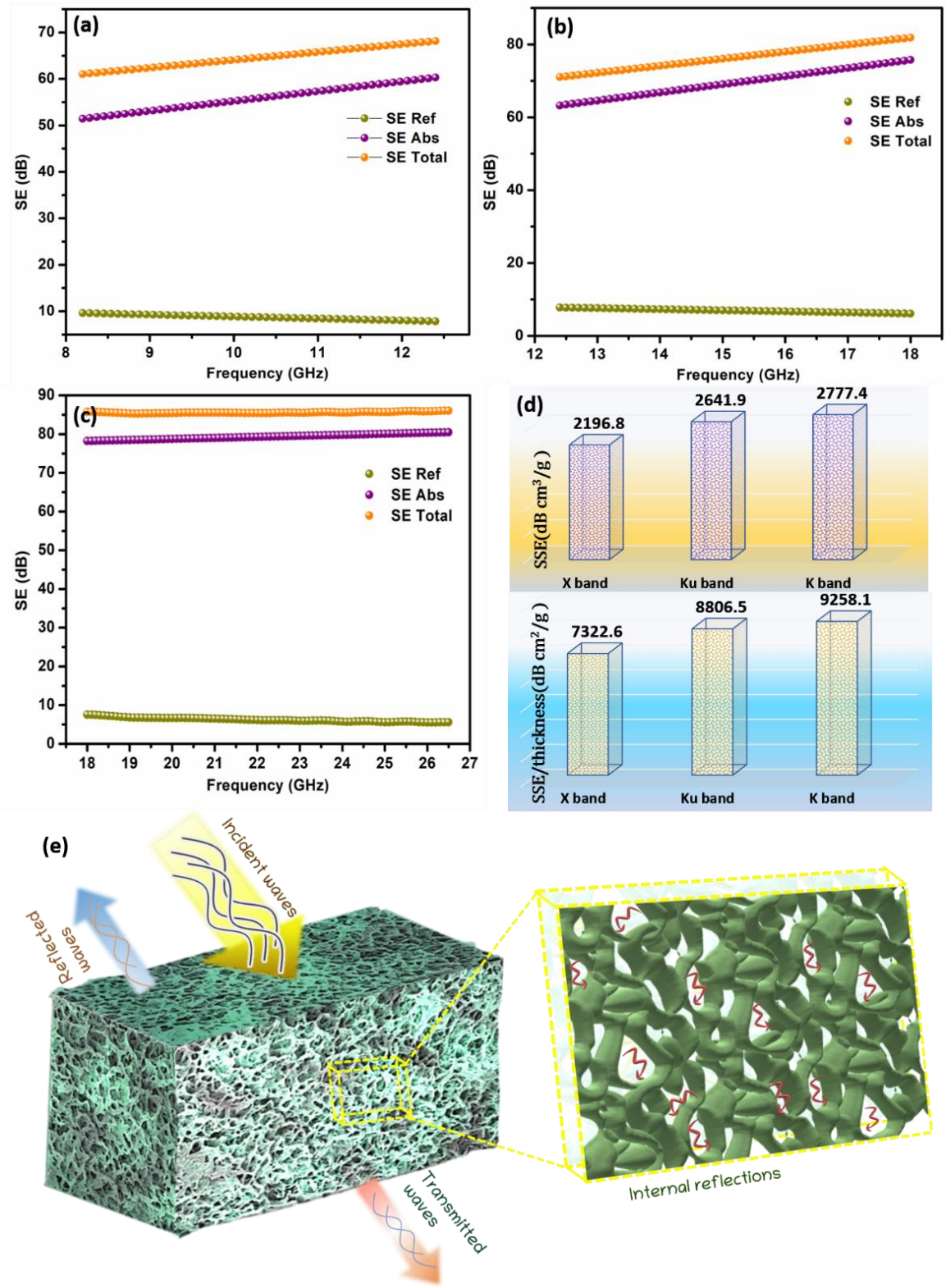

*Figure **4.7** Frequency-dependent variation of total EMI shielding effectiveness (SE_{Total}), reflection shielding effectiveness (SE_{Ref}), and absorption shielding effectiveness (SE_{Abs}) of VPHA (VPHA 35 with 1 M HCl) in (**a**) X (**b**) Ku and (**c**) K band. (**d**) Maxima of SSE and SSE/thickness of VPHA in X, Ku, and K bands and (**e**) a schematic illustration of the EMI shielding mechanism*

Further, the shielding efficiency of the VPHA aerogel was examined in both Ku (12.4-18 GHz) and K bands (18-26.5 GHz) of the electromagnetic spectrum as well. The significant surge in 5G technology and Internet of Things (IoT) demand for reliable EMI shields with high performance in high-frequency bands. Surprisingly, the total shielding values could reach up to maxima of 81.9 dB and 86.1 dB in Ku and K bands, respectively (figures 4.7b&c). Compared to absorption shielding, which varies from 63.2 dB to 75.7 dB, shielding due to reflection is as low as ~7 dB in the Ku band. Absorption shielding efficiency in the K band reaches an even higher value of 80.5 dB, which is expected since the absorption loss increases with increased frequency. Obviously, the massive absorption of the newly designed aerogel stems from high electrical conductivity and the hierarchically porous network formed inside the aerogel.

High EMI SE combined with low density endows VPHA aerogels exceptional specific EMI SE as high as 2196.8 dB cm^3/g in the X-band frequency range. The superior specific shielding efficiency (SSE) and SSE/thickness of VPHA in X, Ku, and K bands are shown in figure 4.7d. The SSE/thickness achieved a supreme value of 9258.1 dB cm^2/g in the K band. This normalized specific absorption is massively better by 2.5 times than the similar V_2O_5-PANI aerogel already reported by us (Puthiyedath Narayanan *et al*., 2021). Green, lightweight, and mechanically robust aerogels like VPHA with excellent specific EMI SE, qualify them as efficient EMI shields in aircraft and portable device applications.

The possible shielding mechanism in the aerogels is illustrated in figure 4.7e. Good impedance matching due to high porosity facilitates the ease of entry of electromagnetic waves into the interior of the VPHA aerogel. A few portions of the waves are still get reflected. The highly connected conductive network formed by the oxide-polymer network improves the electron transfer channels and thus dissipates the entered EM energy by electric loss. The hierarchical architecture of the gel facilitates the electromagnetic waves to get trapped and eventually reabsorbed inside the inner voids and pores by multiple internal reflections and scattering. The high surface area of porous morphology promotes prolonged transmission paths, resulting in attenuation of the EM waves. In a nutshell, the porous structure, interlinked three-dimensional conductive polymer network, and synergistic effects of V_2O_5 and PANI endow the composite aerogel with excellent EMI shielding property and superior specific shielding values.

Table 4.1. A comparative analysis of shielding effectiveness values of porous materials measured in X-band.

Sl No	Sample name	EMI SE (dB)	Thickness (mm)	SSE (dB cm^3/g)	SSE/thickness (dB cm^2/g)	Ref
1	Sponge-supported rGO aerogel	27.3	12	1437	1197.5	(C. Liu *et al*., 2016)
2	C/SiO_2/SiC aerogels	24	6	120	200.0	(An *et al*., 2019)
3	Cellulose composite aerogel	20.8	2.5	219	876.0	(H. D. Huang *et al*., 2015)
4	Carbon aerogel	40	4	700	1750.0	(Vazhayal *et al*., 2020)
5	Graphene-carbon hybrid aerogel	37	3	529	1763.3	(W. L. Song *et al*., 2015)
6	Aerogel-like Carbon	51	10	455	455.0	(Y. Q. Li *et al*., 2015)
7	Polyimide/Graphene Composite Aerogels	28.8	2.5	369	1518	(Z. Yu *et al*., 2020b)
8	GO-polymer aerogel film	53	1.55	434	2800.0	(Han *et al*., 2016)
9	MXene carbon aerogel	71.3	3	360	1200.0	(Liang *et al*., 2020)
10	Leather solid waste /PVA/PANI aerogel	40	2	73	365.0	(T. Zhang *et al*., 2021)
11	V_2O_5-PANI aerogels	34.7	6	1662.2	2770.3	(Puthiyedath Narayanan *et al*., 2021)
12	V_2O_5-PANI@HCl aerogels	68.1	3	2196.8	7322.6	**Present work**

A survey on the EMI shielding performance of similar porous EMI shielding materials in the X band in the aspects of shield thickness and shielding effectiveness is given in table 4.1. In addition, specific EMI SE (SSE=SE/aerogel density) and thickness averaged SSE (SSE/thickness), which we believe are more comprehensive and normalized criteria than total SE in porous materials, are also summarized. Remarkably, the excellent specific shielding values of the present V_2O_5-PANI@ HCl aerogels are significantly higher than

most other materials among EMI shielding gels. As discussed earlier, the present work's exceptional SSE and SSE/t values may be attributed to its ultralow density (~ 30 mg/cm^3) and other factors like the synergistic effect between conductive polymer and the peculiar layered V_2O_5 nanofibers, assembled in hierarchically porous construction. It is worthwhile to note that most highly effective lightweight shields are formed using mesoporous composite architectures, with either carbonaceous components (CNT, graphene, GO, graphite, etc.) or MXene used as the filler to impart sufficient electrical transport. For example, Wang *et al.* synthesized MXene ($Ti_3C_2T_x$)/PBO nanofiber films with excellent SSE/thickness of 8211 dB cm^2/g with 70 wt% loading of polyetherimide-functionalized $Ti_3C_2T_x$ nanosheets (L. Wang *et al.*, 2022). To the best of our knowledge, ours is the first-ever report on creating aerogels without the above-mentioned fillers to achieve the so far highest specific shielding per unit thickness. These robust and lightweight shielding solutions are useful for EM wave attenuation in aeronautical structures and portable devices.

4.4 Conclusions

In summary, a hybrid aerogel comprising hydrated vanadium pentoxide nanowires and polyaniline (PANI) was prepared by introducing aniline monomer to oxidative V_2O_5 template in the presence of a strong acid, HCl. Polyaniline, grown over the V_2O_5 nanowire bundles, binds the wires to form a robust 3D networked, porous structure. The high degree of polymerization in controlled addition of HCl promotes the porosity to organize hierarchically, with substantially connected polygonal comb-like microstructure at the microscale, whose blocks are bent and folded to form conductive aerogel at the macroscale. Their organized microstructure facilitates the efficient conduction of charge carriers in the polymer chain, thereby boosting their conductivity values. Thus, the polymerization of V_2O_5-PANI aerogels in an acid medium derives high conductivity aerogels (~4.3 S.cm^{-1}), whose electrical conductivity is 2150 times better than that of pure V_2O_5 aerogel (~0.002 S.cm^{-1}). The V_2O_5-PANI aerogels aged for a period of 35 days are found to be ultralight in density (~32.0 mg/cm^3). An adequately machined aerogel block of 850 mg can hold a weight up to ~240g without any structural deformations, which means that the well-retained three-dimensional porous structure provides sufficient compressive strength to the nanocomposite aerogel, much better than that of pure V_2O_5 gel. All the aerogel composites used in this research showed absorption dominant shielding performance with relatively low reflection shielding values (percentage SE_{Ref} < 20% total EMI SE). Compared to V_2O_5

aerogel, the high shielding V_2O_5-PANI composite aerogels have nearly eight times higher shielding efficiency. The sample V_2O_5-PANI aerogels aged for 35 days show a maximum of 68.1 dB total shielding efficiency in the X-band, corresponding to 99.99998% blocking of the incident waves, respectively. These aerogels show better shielding performance in the Ku and K bands (81.9 dB and 86.1 dB, respectively). The specific shielding efficiency is 2777.4 dB cm^3/g, while SSE/thickness shows an impressive value of 9258.1 dB cm^2/g, which is at least 2.5 times more than the nearest report. Based on the experimental results, we believe that the meso and macroporous structure combined with the high electrical conductivity of polymer adds up to high EM wave absorption. Moreover, the synergistic effect between the two components, V_2O_5 and PANI, leads to remarkable improvements in properties. To the best of our knowledge, ours is the first-ever report on creating aerogels without the carbonaceous and MXene fillers to achieve the so far highest specific shielding/thickness. Further, this study provides an economical and effective way to obtain a promising carbon filler-free candidate for ultra-light shields that can be used in portable electronic mobile devices and aeronautic structures.

Chapter 5

Hydrothermally Derived Vanadium Pentoxide -Polyaniline Aerogels

- Novel hydrothermally derived EMI shielding aerogels made of V_2O_5 and polyaniline are reported for the first time
- Mechanically stable and light aerogels have a good green index (>1) and high electrical conductivity (5.11 S/cm)
- V_2O_5 -PANI aerogels have broad bandwidth with EMI SE reaching 53.6 dB in the X band
- EMI SE reaches 71.2 dB in the K band with an exceptional SSE/thickness of 5929.2 dB cm^2/g.

5.1 Introduction

Our previous two chapters discussed highly porous V_2O_5- PANI aerogels prepared by polymerizing the vanadium pentoxide precursor solution prepared by polycondensation of vanadic acid. They exhibited an impressive EMI SE >30 dB even at a nominal density of ~20 mg/cm^3. Noticeable is the fact that, although these materials show excellent EMI shielding properties, the construction of the aerogels is time-consuming, as it needs at least 20-30 days to obtain sufficient shielding. Herein, we aimed to formulate a cheap alternative to integrate the conductive polymer within the porous inorganic skeleton of vanadium pentoxide to achieve excellent shielding values within a short period.

Hydrothermal synthesis is a competent tool for creating distinct, beautiful nanoscopic V_2O_5 morphologies compared to other methods such as sol-gel, template-assisted growth, and electrospinning (Ahirrao *et al*., 2018; G. P. Li & Luo, 2007; Xiong *et al*., 2008). Specific nanostructures, unattainable by other traditional routes, can be developed efficiently by the hydrothermal method. This is important since forming 3D porous architectures requires longer nanowires to form a robust cell wall skeleton. As discussed in chapters 2 and 3, polycondensation of vanadic acid in water yields $V_2O_5.nH_2O$ nanowires, but it takes several weeks to obtain micrometers long nanowires. On the other hand, hydrothermal reactions are cost-effective, time- and labor-saving methods to synthesize excellent vanadium oxide nanostructures with a high aspect ratio (Y. Wang & Cao, 2006). Once the synthesis protocol for a standard hydrothermal procedure with optimum reaction temperature, the concentration of solvents, pH value of the system, reaction time, autoclave geometries, etc., is established, it is easier to develop three-dimensional architectures made of desired nanostructures (Krumeich *et al*., 1999).

The present study demonstrates a high-pressure-assisted facile strategy to synthesize a green polymer composite aerogel with more efficient EMI shielding. Herein, V_2O_5 hydrogel synthesized by the simple one-pot hydrothermal method was reinforced by conducting polymer polyaniline followed by the freeze-drying process to obtain V_2O_5-polyaniline aerogel. The advantage is that ultra-low-dense aerogels' nature and pore distribution can be readily tuned using this method. Aerogels' formation mechanism, morphology, and EMI properties were systematically investigated and discussed.

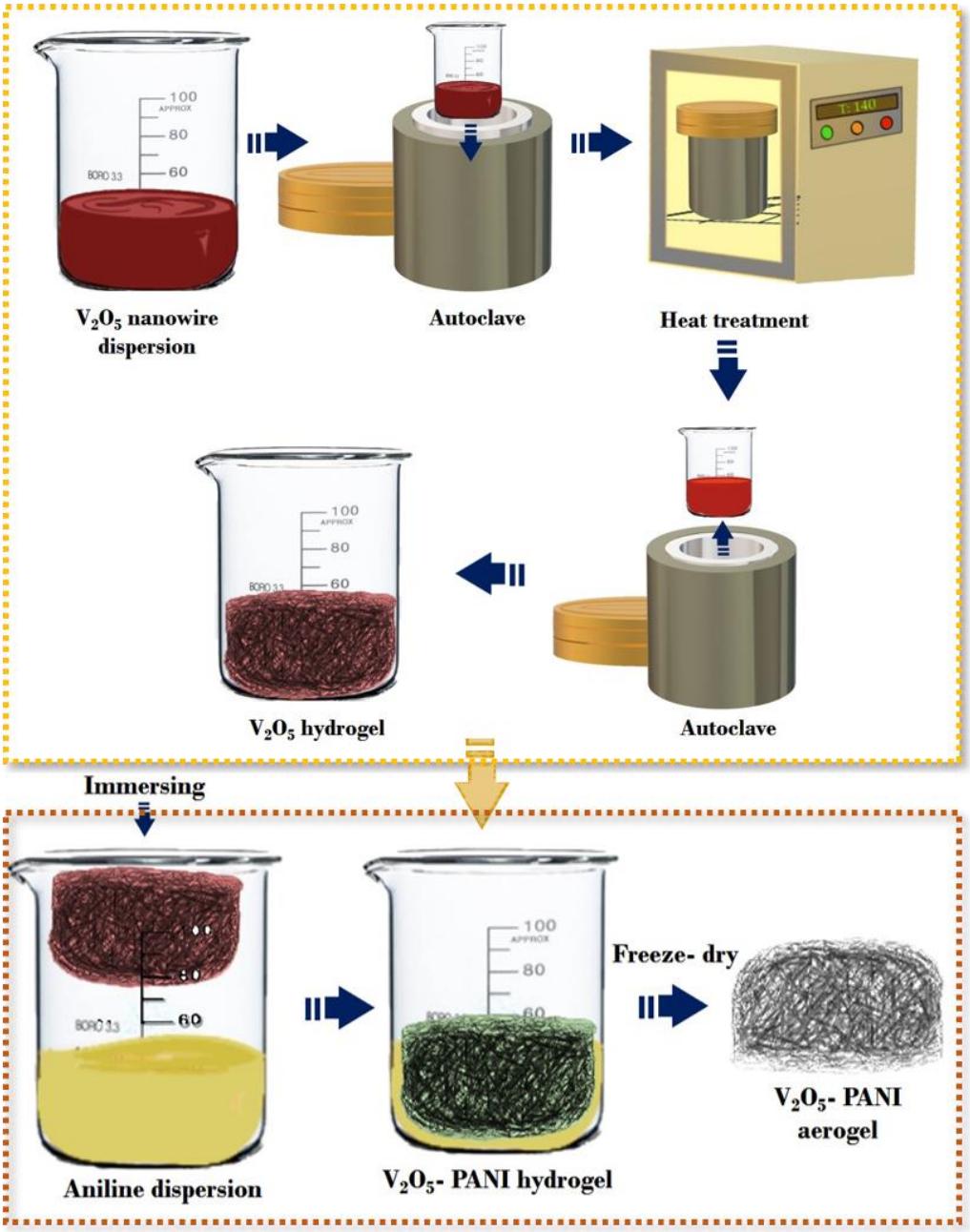

*Figure **5.1** Schematic illustration of the synthesis of V_2O_5- PANI aerogel.*

5.2 Experimental

5.2.1 Materials

Ammonium metavanadate (99%) was purchased from Sigma-Aldrich Co. USA. Aniline and hydrochloric acid (HCl 37%) were obtained from Merck Life Science Private Limited, Mumbai. All the chemicals were used as received without any further treatment.

5.2.2 Hydrothermal preparation of V_2O_5 hydrogel

The V_2O_5 gel was prepared by the simple and time-saving hydrothermal method (see figure 5.1). Initially, the V_2O_5 dispersion was prepared through the same protocol, as described in chapter 2. Final dispersion was made to 40 mL by adding hot water, transferred to a Teflon-lined autoclave, and heated to 140 ºC for 24 hours. The resulting V_2O_5 hydrogel was washed with DI water several times to purify it.

5.2.3 Preparation of V_2O_5- PANI aerogels

The V_2O_5 hydrogel was immersed in a solution of aniline monomer in deionized water. Polymerization was evident from the sudden hydrogel color change from dark red to emerald dark green. The solution was kept undisturbed for about 3-5 hours until the polymerization was complete. Finally, the V_2O_5- PANI hydrogel was freeze-dried at -110 ºC for 24 hours to form the V_2O_5- PANI (VPHT) aerogel. Similarly, V_2O_5- PANI@HCl (VPHTH) aerogel was prepared with only a slight variation in the monomer composition. In the case of VPHTH, aniline solution was prepared by dissolving the same amount of monomer in 1M hydrochloric acid. Then V_2O_5 hydrogel was immersed in it, followed by freeze-drying. For comparison, pure V_2O_5 hydrogel was also freeze-dried under the same conditions, and the sample was named VHT.

5.2.4 Characterization

The three hydrogels of VHT, VPHT, and VPHTH were freeze-dried at -110ºC by Scanvac Cool Safe Pro 110-4, M/s. Labogene, Denmark. Fourier transform infrared spectroscopy (FTIR) was performed to compare the chemical structure of the pure and composite aerogels using a Perkin Elmer Series FTIR spectrum-2 instrument through the ATR method. Raman spectra (confocal Raman microscope α-300R WITec, Inc., Germany) and Wide-angle X-ray diffractogram (Xeuss SAXS/WAXS system using a Genixmicro-source from Xenocs (Grenoble, France), operated at 50 kV and 0.6 mA) were recorded to confirm the formation of composites. X-ray photoelectron spectroscopy (PHI 500 Versa Probe 2 with Al Kα radiation) was used to evaluate the surface chemical composition of the aerogels. Field emission scanning electron microscopy (FESEM, FEI-Nova Nano SEM 450, beam potential of 10 kV) and high-resolution transmission electron microscopy (FEI Tecnai G2 30S-TWIN, FEI Co., Hillsboro, OR, USA) observed the microstructure and

morphologies. Thermogravimetric analysis was done using a simultaneous thermogravimetric analyzer (STA 7300, Hitachi, Japan). For this testing, the samples were heated from 25ºC to 650ºC at a rate of 10ºC/min in the air atmosphere. The Brunauer–Emmett–Teller (BET) surface area and pore size of the samples were measured after degassing the samples at 150ºC for 12 hours using a nitrogen adsorption-desorption isotherm (Gemini 2375, Micromeritics, Norcross, USA). The pore size distributions of the aerogels were measured using the Barrett–Joyner–Halenda (BJH) method. The DC conductivity of the samples was measured using the four-probe method from Keithley 2450 source meter. A Keysight PNA-L N5234B network analyzer was used in the X, Ku, and K bands to investigate the EMI shielding performance of the aerogels. All the aerogel samples were precise to a thickness of 3 mm.

5.3 Results and discussion

There are several methods to prepare vanadium pentoxide nanostructures (Ahirrao *et al*., 2018; Dong *et al*., 2016; Xiong *et al*., 2008). Herein, we introduce an effortless, two-step method to prepare the aerogels. Figure 5.1 illustrates a schematic of the preparation of V_2O_5-PANI composite aerogels. A dispersion of hydrated V_2O_5 nanoribbons having less than 2 µm in length was prepared through polycondensation of vanadic acid in DI water at room temperature. After hydrothermal treatment in an autoclave, the colloidal dispersion produced a crimson red colored V_2O_5 hydrogel (see figure 5.2a). During the hydrothermal reaction, decavanadic acid was formed, which then dissociated to V_2O_5 gel. $V_2O_5\,nH_2O$ sheets were developed by dehydration of V_2O_5 gel. As the reaction progressed, these $V_2O_5\,nH_2O$ sheets were further dehydrated and shaped into V_2O_5 nanowires (N. Wang *et al*., 2015). The oriented attachment growth mechanism can explain nanowire growth, which has been recognized as a primary growth mechanism during the hydrothermal synthesis of various materials. The nanowires are self-assembled by their electrical attraction (X. Wu *et al*., 2003). The nanofibers orient and attach to form ultra-long wires in such a way to lower the surface energy (M. Li, Kong, *et al*., 2011). The temperature and reaction time is crucial for the formation of the hydrogel. Primarily, we have noticed that no gel structure was found if the reaction temperature and time exceeded the optimum values of 140ºC and 24 h. Secondly, the penetration of polyaniline solution into the inorganic oxide gel matrix had to be meticulously designed and was also tricky. Incorporating the solution of conducting polymers into a hydrogel matrix is rarely used as a technique to derive conductive aerogels.

In the case of VPHT and VPHTH gel synthesis, the hydrogel was carefully dipped into the respective aniline solution and waited for a few hours for complete polymerization, as shown in figure 5.1. Polymerization and gelation started immediately after the immersion, with a sudden color change from orange-red to dark green; green corresponds to the emeraldine form of polyaniline (W. Huang *et al*., 1986). The composite hydrogel thus formed is rather stable and robust (figure 5.2a). The wet hydrogel can be described as a nanocomposite of a liquid phase trapped within a continuous vanadium oxide nanowire network. Finally, freeze-drying was adopted to convert hydrogel to light aerogel. In the process, the liquid inside the gel's pore will get frozen to a solid phase and then sublimed out of the gel. The freeze-drying process exerts low capillary forces on the pore walls, so the high porosity is well maintained in the dried aerogel (Y. Chen *et al*., 2021).

The light composite aerogel, VPHTH, is shown in figure 5.2b, and detailed microstructure was observed by optical microscopy. The optical microscopic image of the VHT (figure 5.2c) indicates highly crinkled layers with random orientation. This unique architecture, which provides more specific surface area, is highly beneficial for the shielding purpose. The uneven structure increases the number of contact points for an incoming wave, leading to abundant multi-scattering in the aerogel samples. This, in turn, can enhance the transmission path and can thus significantly attenuate the incident EM waves. The detailed elemental mappings of VPHTH explain the homogeneous distribution of elements (figure 5.2d). The uniform coating of components in PANI over vanadium pentoxide wires helps improve microwave absorption performances. The morphology of the aerogels with and without polymer was also examined using FESEM. The interconnected 3D network structure of aerogels is clearly visible in SEM images with high magnification (figures 5.3a&c), and figure 5.3c validates the binding of nanowires by the polymer. The morphology of composites VPHT (figure 5.3d) and VPHTH (figure 5.3e&f) perfectly emulates the highly porous and layered morphology of VHT (figure 5.3b) created by the sublimation of ice crystals during the freeze-drying. This implies that the polymer is uniformly coated over vanadium oxide wires without damaging its nanoskeleton. Stacked nanosheets are visible in figure 5.3e. We believe that the seemingly rough nature of layers and their irregular alignment supports more scattering and internal reflections of EM waves. Moreover, the voids and space between the wrinkled nanosheets can also increase the propagation path of EM waves into their depths and crevasses and dissipate them by more reflections. The ultra-thin V_2O_5 nanowires obtained after the hydrothermal treatment are

several micrometers long (> 20 µm). TEM images (figures 5.3g-i) substantiate the high aspect ratio of ultra-thin nanowires with 8-15 nm width. The optimum aspect ratio of the reinforcing wires is essential for forming a robust gel. Consistent with SEM, the bundles of wires seem wrapped by the polymer and are clearly seen in TEM images of VPHT (figure 5.3h) and VPHTH (figure 5.3i).

Figure 5.4a illustrates the WAXD pattern of the aerogels VHT, VPHT, and VPHTH. It is reported that the partial reduction of vanadium (V^{5+} to V^{4+}) occurs during the hydrothermal synthesis, and hence, the peaks are a mixture of two different phases of $V_2O_5 \cdot nH_2O$. Peaks observed at 2θ values of 8.9º and 21.5º respectively correspond to (001) and (003) reflections of layered vanadium pentoxide. Previous reports suggest that the extreme orientation along (00*l*) planes is initiated during hydrogel's hydrothermal growth (Kundu *et al*., 2017; Q. Wei *et al*., 2015). Peaks at 26.3º, 30.7º, and 32.1º are indexed to orthorhombic phases of vanadium pentoxide (Kundu *et al*., 2017). In other words, the XRD pattern shows a significant part of reflections corresponding to V_2O_5 in the orthorhombic phase and a minor remnant of V_2O_5 in the monoclinic phase (Ronquillo *et al*., 2016). As evident from figure 5.4a, the reflection peaks of both V_2O_5 precursor and V_2O_5-PANI aerogel are alike and without any additional peaks of PANI. So, incorporating PANI into the V_2O_5 matrix does not change its crystalline construction, which can be due to the low volume percentage of polymer or the possibility that reticular planes of the semi-crystalline polymer do not repeat in order. However, a significant decline in the intensity of V_2O_5 peaks is a consequence of the inclusion of polymer. This indirectly means that the hydrated V_2O_5 nanowires are homogeneously enwrapped by polyaniline without affecting their crystalline order. But polymerization must have resulted in a less crystalline composite. The crystallinity of the PANI sample depends on several factors, including the preparation conditions like pH, temperature, doping level, etc. Our observation of low crystallinity in polymer corroborates an earlier report that polymerization in an acidic medium yields PANI having low crystallinity (Fosong *et al*., 1988). Since WAXD could not confirm it, let us further examine the aerogels using infrared and Raman spectroscopy to assess the presence of PANI in the composites.

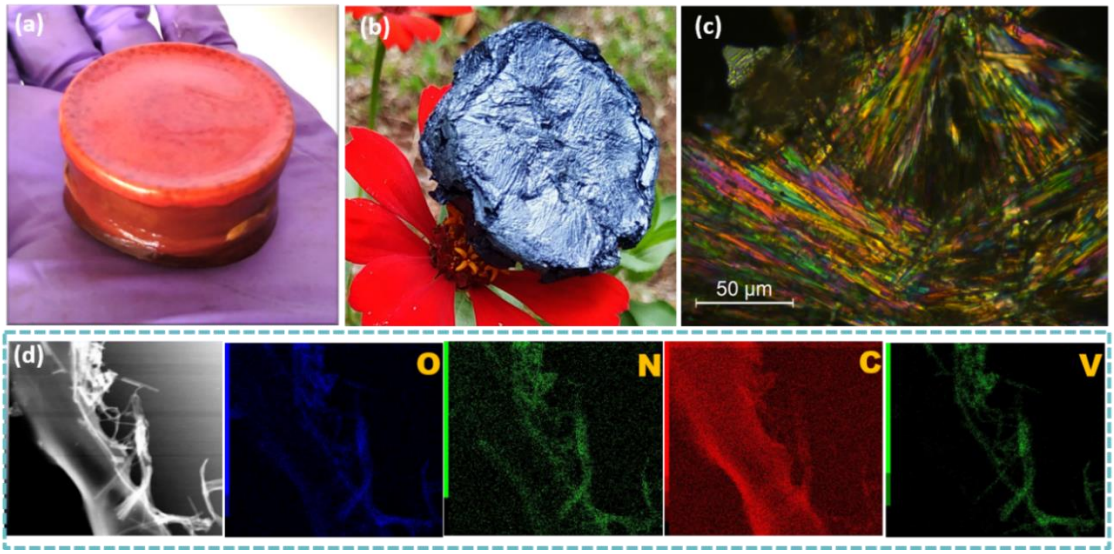

*Figure **5.2** Photographic image of (**a**) V_2O_5 hydrogel, (**b**) V_2O_5- PANI@HCl composite aerogel (VPHTH) resting on a flower, (**c**) optical image of V_2O_5 aerogel (VHT); (**d**) Elemental mapping of VPHTH aerogel.*

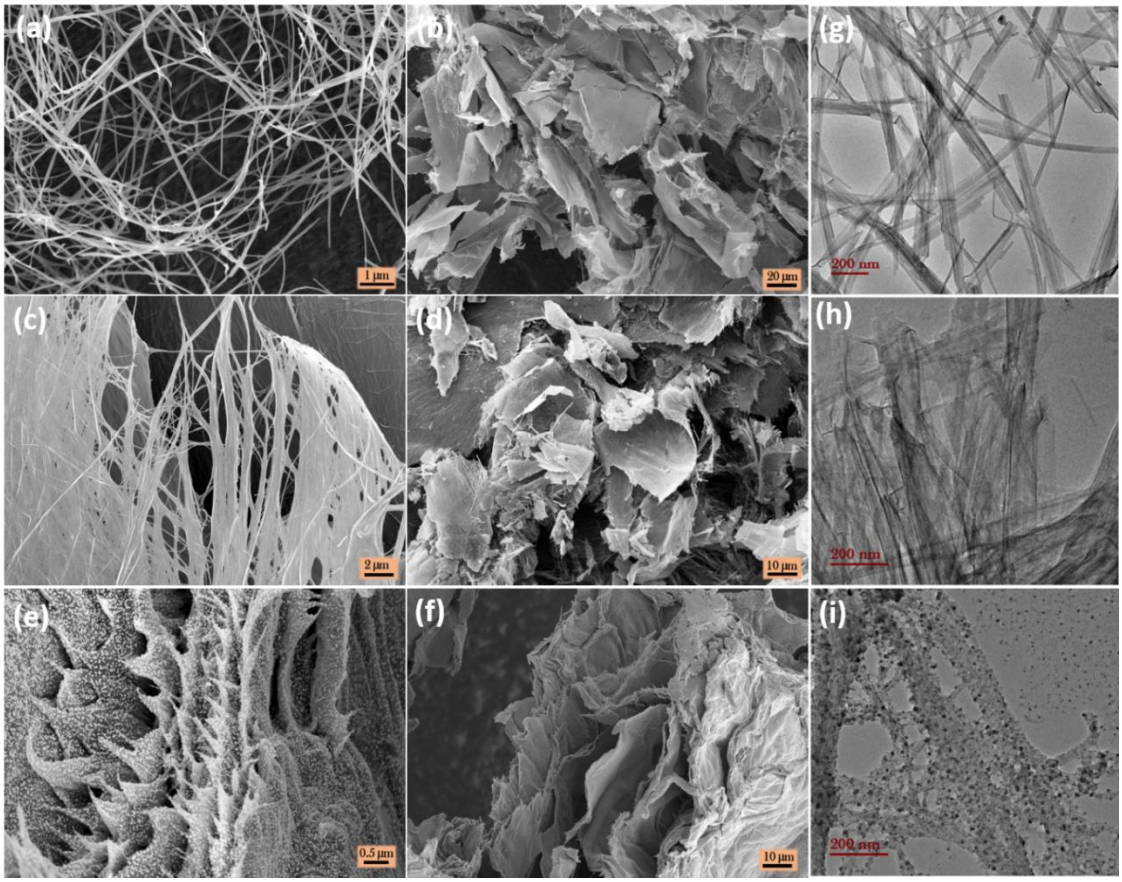

*Figure **5.3** SEM images of (**a& b**) VHT, (**c& d**) VPHT, (**e& f**) VPHTH aerogels, TEM images of (**g**) VHT, (**h**) VPHT, and (**i**) VPHTH aerogels.*

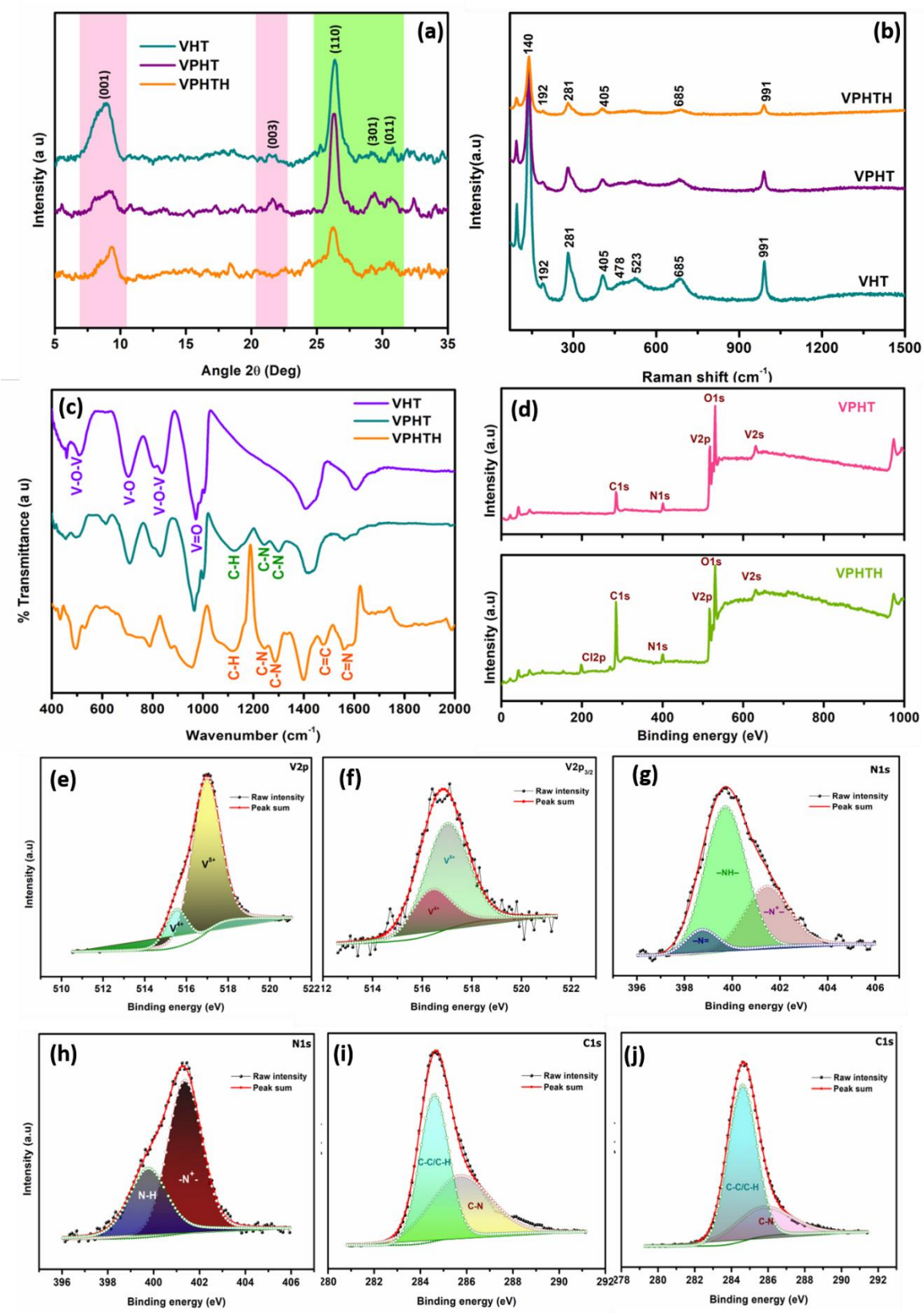

*Figure **5.4** (**a**) WAXD pattern and (**b**) Raman spectra of V_2O_5 precursor and V_2O_5-PANI aerogel; (**c**) FTIR-ATR spectra of aerogels, (**d**) XPS survey spectrum of V_2O_5-PANI aerogels, high-resolution XPS spectra of (**e& f**) V2p, (**g& h**) N1s, and (**i& j**) C1s in VPHT and VPHTH respectively.*

Raman spectrum of aerogels was taken at room temperature in the wavenumber range of 100–1500 cm^{-1} (figure 5.4b). The peaks of pure V_2O_5 aerogel are symmetric with the reported Raman modes for V_2O_5 nH_2O (Abd-alghafour *et al*., 2016; Abd-Alghafour *et al*., 2020; Londoño-Calderón *et al*., 2010). The dominant peak at 140 cm^{-1} corresponding to V-O-V chain vibrations indicates the layer structure of the V_2O_5 precursor. The two peaks at 281 and 405 are associated with the bending vibration of the V=O bonds, and 991 cm^{-1} is assigned to the V=O stretching vibrations (Londoño-Calderón *et al*., 2010). The peaks located at 478 and 685 cm^{-1} are assigned to bridging V-O-V bending and stretching modes, respectively (Abd-alghafour *et al*., 2016; Londoño-Calderón *et al*., 2010). Raman peak at 523 is attributed to triply coordinated oxygen, V_3-O stretching modes (Londoño-Calderón *et al*., 2010). Strangely enough, the polymerization did not make any visible difference in the Raman spectrum. This may be due to the relatively low volume percentage of polymer compared to V_2O_5.

The FTIR results (figure 5.4c) of the pure vanadium oxide hydrogel (VHT) show peaks around 459, 505, and 714 cm^{-1} due to the V-O-V stretching mode. The absorption peak at 837 cm^{-1} is the vibration of doubly coordinated oxygen bonds. The peak at 964 cm^{-1} corresponds to the stretching vibration of terminal oxygen bonds V=O (Derkaoui *et al*., 2017; Mukhtar *et al*., 2017). The broader band near 1409 cm^{-1} and the narrow band at 1610 cm^{-1} are attributed to the water molecules chemically bonded to the oxide network (Cao *et al*., 2013). Five bands observed in the wavenumber range 1000–1600 cm^{-1} clearly describe the intercalation of polymer within the V_2O_5 matrix. The peak at 1120 cm^{-1} shows the stretching of N=Q=N (where Q denotes the quinoid ring). The characteristic peaks at 1240 and 1300 cm^{-1} correspond to C–N stretching band of aromatic amine. The ring stretching of quinoid and benzenoid form are observed at 1585 and 1480 cm^{-1}, respectively (John *et al*., 2010). Hence the FTIR results clearly reveal the signatures of polymerization in the composite aerogel.

In order to authenticate the presence of polyaniline in the composite, its chemical structure was further explored by conducting XPS measurements. The survey spectra of VPHT and VPHTH (figure 5.4d) reveal the presence of N1s and C1s in the composite form, confirming the intercalation of the polymer. The deconvoluted $V2p_{3/2}$ binding energies of both VPHT and VPHTH match with the electronic states of V^{5+} and V^{4+} as shown in figures 5.4e&f, respectively. The peak at 530 eV corresponds to O1s, and the peak centered around

285 eV corresponds to the carbon backbone of PANI. N1s region of both composites can be deconvoluted into two synthetic peaks. The fitted peaks of VPHT at 399.8 eV and 401.4 eV are consistent with the typically reported values for the quinoid amine (=N-) and the nitrogen cationic radical ($–N^+$), respectively (figure 5.4g). Similarly, three peaks are observed in VPHTH (figure 5.4h) at slightly different binding energies, 398.7 eV (=N-), 399.7 eV(-NH-), and 401.5 eV ($–N^+$) (Patil *et al*., 2018; Waghmode *et al*., 2017). The C1s peak can be deconvoluted into two prominent peaks of C–H/ C–C functional carbon of the quinoid ring and the C-N bond (figure 5.4 i& j). Unlike VPHT, the survey spectrum of VPHTH shows chlorine peaks which implies the existence of hydrochloric acid during the gelation, something which not only helps polymerization but also gets doped into the composite aerogel.

Thermogravimetric analysis (TGA) was carried out for all the samples VHT, VPHT, and VPHTH, and the results are shown in figure 5.5a. The TG curve of $V_2O_5.nH_2O$ aerogel exhibits two prominent weight loss slopes. A steep fall in the curve followed by a gradual weight loss until 100ºC corresponds to the loss of weakly bound water. As temperatures increased, the tightly bonded physisorbed hydroxyl molecules started to evaporate. As per the literature reports, the second weight loss step at the proximity of 340 ºC is probably due to phase conversion from the disordered layer phase to the orthorhombic phase with additional elimination of water (Gotić *et al*., 2003). The total weight loss of the pure V_2O_5 sample, VHT, is about 17 % until 380 °C, after which weight remains constant. For the polymer reinforced sample VPHT, the initial loss till 104 ºC due to the removal of bound water is ~8.1%. The increase in weight loss (~18.4%) in the subsequent gravimetric loss step compared to VHT indicates polymer decomposition and phase change of V_2O_5. A seemingly different weight loss profile was obtained for the composite aerogel synthesized in acidic atmosphere (VPHTH). Here, a significant weight loss of ~30% occurs at low temperatures. This is due to the evaporation of excess adsorbed moisture and doped molecules in the emeraldine form of polyaniline (Cruz-Pacheco *et al*., 2020). As the temperature reached beyond 100 °C, the tightly bonded water molecules were removed, and crystallization to orthorhombic V_2O_5 started. Decomposition of polyaniline backbone units also occurs in the temperature range of 300 to 500ºC (weight loss ~ 38.2%). Higher polyaniline content implies polymerization is more efficient with the presence of acid in VPHTH. From the retained weight percentage after the complete burn-off of the polymer at 440 °C, we can calculate the amount of V_2O_5 contained. In the case of the pure sample

VHT, 83% of the initial weight remains, while the values are 75% and 11% for VPHT and VPHTH, respectively. The lower percentage of V_2O_5 suggests that the content of the polymer is highest in VPHTH, which obviously can improve the conductivity and hence the microwave attenuation.

Figures 5.5b-d show the nitrogen adsorption/desorption isotherm of VHT, VPHT, and VPHTH. The isotherm exhibits mesoporous nature, consistent with the sheet-like, porous three-dimensional structure. The actual BET surface area and pore volume of the VHT are estimated to be 8.26 m^2 /g and 0.048 cm^3/g, respectively. Upon polymerization, the surface area and pore volume visibly improved to 22.94 and 0.087 m^2 /g for VPHT and 23.19 and 0.090 m^2 /g for VPHTH, respectively. Therefore, with the addition of polymer, the BET surface area increased nearly three times which can favor the dissipation of electromagnetic energy by prolonged propagation path of the EM waves and total internal reflection. The pore size distribution (inset of figures 5.5b-d) shows that the peak pore diameter is 0-50 nm. The synergistic contribution of mesopores (suggested from BET analysis) and macropores (pore size >500 nm, as evident from the SEM images) qualify the gels as suitable for highly absorbing microwave attenuators.

Figure 5.5e shows the electrical conductivity of VHT, VPHT, and VPHTH aerogels. It can be seen that the addition of polymer significantly improves the conductivity of aerogels. This is because polyaniline enhances the conductive network inside the three-dimensional oxide network. Studies proved that the conductivity of the emeraldine form of polyaniline varies depending on the degree of protonation, from 10^{-10} S/cm (insulating state) to ~10^{-1}-10^{2} S/cm (metallic state) (Ali Mohsin *et al*., 2020). VPHTH composites show the highest conductivity (~5.1 S/cm) compared to others, owing to the higher protonation of polymer in the presence of the acid medium. A visible increase in electrical conductivity with a decreased pH of the monomer solution was reported earlier (Ali Mohsin *et al*., 2020). The inter-chain charge transport depends on protonation, which mainly contributes to the conductivity of polyaniline (Hassan *et al*., 2012; W. Huang *et al*., 1986). The degree of protonation largely depends on the pH of the solution and the oxidation state of PANI (Detsri & Dubas, 2009). Here, with the presence of an acid, protonation and hence the polymerization of aniline increases. Accordingly, the electrical conductivity also increases (Ali Mohsin *et al*., 2020). It may be recalled that more presence of polymer in VPHTH aerogel was evident from TG analysis (see figure 5.5a). The combined effect of

the electrical transport characteristics of PANI and the extended nanowire network of V_2O_5 might be the reason for the high conductivity of the composite aerogel. The densities of aerogel samples are shown in figure 5.5f. Such high conductivities of VPHT and VPHTH at ultra-low densities of ~0.04 g/cm^3 can be ascribed to the well-interconnected nanowire network in the layers of composite aerogels.

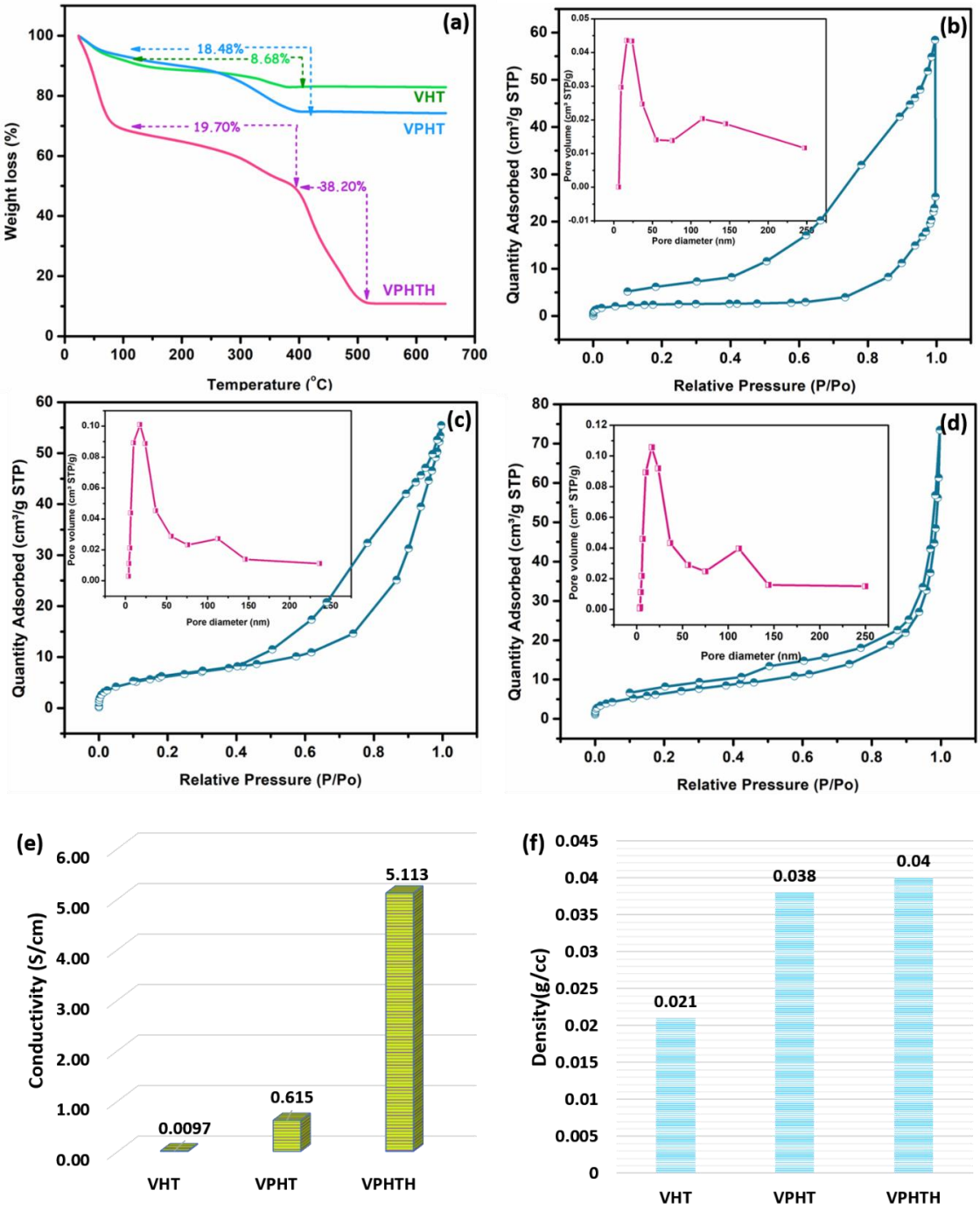

*Figure **5.5** (**a**) TGA of aerogels and N_2 adsorption-desorption isotherms and pore distribution curves of (**b**) VHT, (**c**) VPHT, and (**d**) VPHTH aerogels; (**e**) The electrical conductivity of various aerogels and (**f**) Density of aerogels.*

Finally, we conducted all the essential EMI shielding measurements in X, Ku, and K bands to assess aerogels' EM wave attenuation ability. As hinted before, aerogels with well-layered conductive network structures are expected to display promising shielding effectiveness. In the beginning, the total EMI SE of all the aerogels with a thickness of 3 mm was measured in the X band frequency range of 8.2-12.4 GHz, using the transmission waveguide method, and the results are shown in figure 5.6a. The unpolymerized aerogel VHT reveals only a feeble EMI shielding ability, less than the minimum practical requirement of 20 dB, primarily due to its insulating nature. After polymerization, the layered 3D network becomes more electrically conducting, resulting in a pronounced increase in EMI shielding efficiency. It is noteworthy that, for all the aerogels, the total EMI SE curves have only narrow fluctuations within the wide frequency range and thus provide an unperturbed shielding bandwidth. As expected, VPHTH aerogels show superior EMI shielding efficiency owing to their three-dimensional mesoporous network, large surface area, and highest electrical conductivity among the three categories of aerogels tested. A detailed picture of shielding ability was investigated to unveil the primary mechanism of shielding. Total SE was calculated as the overall sum of the contribution from three shielding mechanisms, absorption (SE_{Abs}), reflection (SE_{Ref}), and multiple internal reflections (SE_M).

Figures 5.6b-d depict the variation of aerogels' absorption, reflection, and total shielding ability within the X band frequency range. These results suggest that all these aerogel samples dissipate EM waves primarily by the absorption shielding mechanism. Clearly, the dominant part of the total shielding potential of VHT samples is absorption-type (~14 dB) due to their peculiarly layered and porous structure. The aerogels formed after incorporating conducting polymer show significantly enhanced shielding performance with absorption SE (>20 dB). In accordance with the SEM results, the robust and regular 3D network constructed within the VHT was well maintained even after the polymerization in VPHT and VPHTH aerogels. Compared to VHT, the absorption SE of VPHT was slightly improved, and that of VPHTH was significantly increased in the measured frequency span. This pronounced improvement of SE after polymerization is evident from the proportional relation between absorption factor (A) and electrical conductivity (σ) (Tong, 2008).

$$A = 131t\sqrt{f\mu\sigma} \tag{5.1}$$

where μ is the relative permeability and t is the thickness of shielding material.

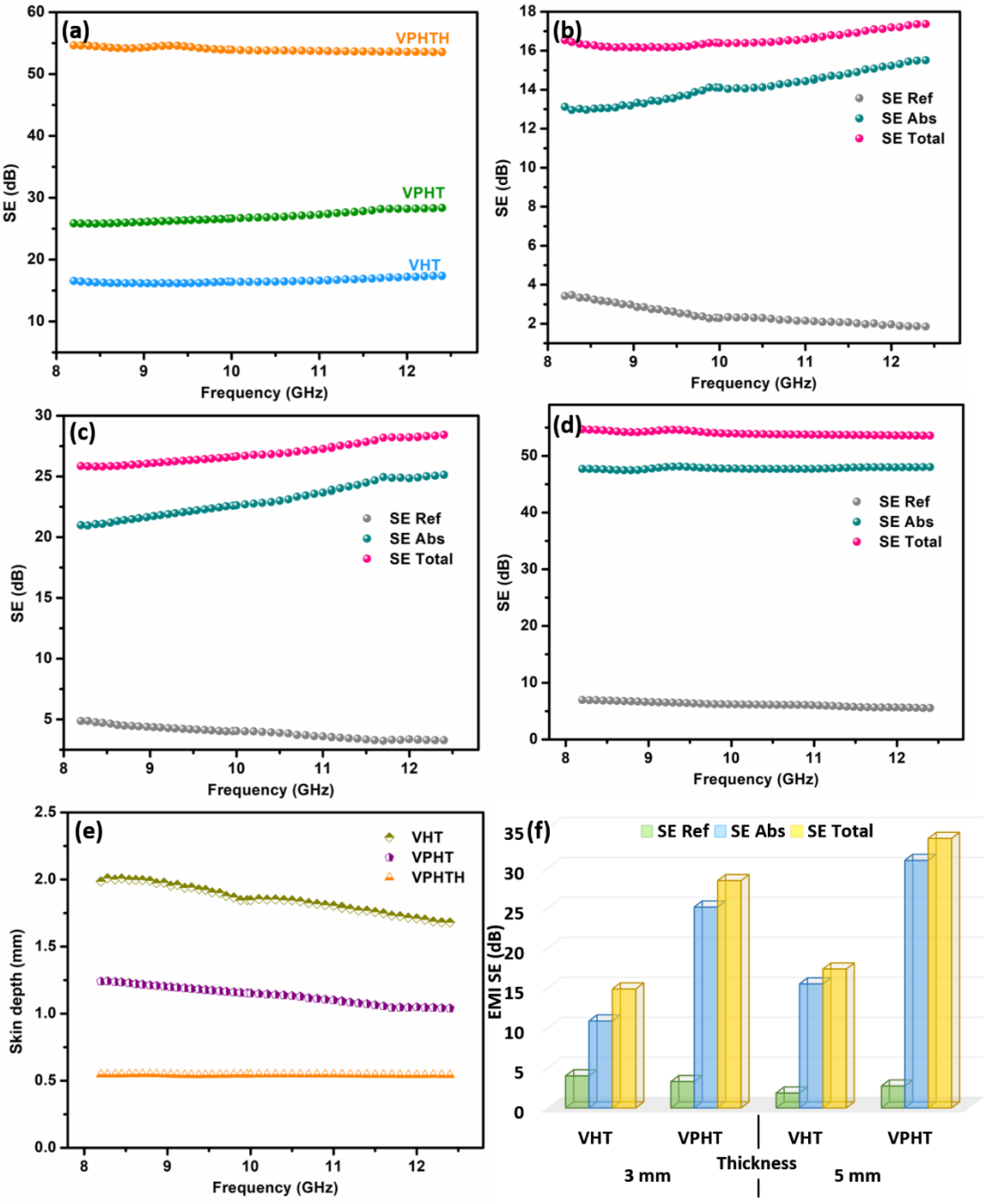

*Figure **5.6** (**a**) Frequency-dependent variation of total EMI shielding effectiveness of aerogels over X band. Frequency-dependent variation of total EMI shielding effectiveness (SE_{Total}), reflection shielding effectiveness (SE_{Ref}), and absorption shielding effectiveness (SE_{Abs}) of (**b**) VHT (**c**) VPHT, and (**d**) VPHTH over X band frequency range (8.2–12.4 GHz) and (**e**) frequency variation of skin depth of aerogels in X band; (**f**) Shielding efficiency of VHT and VPHT aerogels at two different thicknesses at 12.4 GHz*

Conductivity plays a major role in the absorption SE because the incident electromagnetic waves' micro-current generated inside the system will eventually attenuate the waves. The

observable increasing trend of absorption shielding efficiency with frequency is also elucidated by Equation 5.1. Furthermore, the slight increase in density of aerogels suggests a more compact packing of layers favoring EM absorption. It is well established that higher electron transport in HCl polymerized gels can supplement to the higher SE_R. Hence, reflection SE is marginally better for the acid polymerized composite aerogels, VPHTH. Usually, shields with high electrical conductivity show strong reflection when the differences in impedance aggravate. But luckily, here, the seemingly better impedance match between the incident wave and aerogels keeps the reflection SE values to stay less than 7 dB, thus contributing little to secondary pollution (Tong, 2008).

Skin depth (δ) is another important parameter of EMI shielding materials, defining the distance through which the EM intensity reduces to 1/e times the incident intensity. Skin depth is related to the absorption shielding efficiency of materials with a fixed thickness, *t* as follows (Zhan *et al*., 2019):

$$SE_{Abs} = 20\frac{t}{\delta} log\, e \tag{5.2}$$

Figure 5.6e shows the skin depth of aerogels in the X band frequency range. The average values in the 8.2–12.4 GHz frequency range are 1.9, 1.1, and 0.5 mm for VHT, VPHT, and VPHTH. The values of polymerized samples are much lower than the thickness of the aerogels (3 mm), suggesting they can efficiently shield the EM waves. The sharp decrease in skin depth of VPHTH once indirectly validates its outstanding shielding capability.

Well-known is the fact that highly conductive and porous materials dissipate electromagnetic waves more effectively. The polymerized VPHT gels show only ample shielding efficiency at 3 mm thickness. So next, we briefly investigated the dependence of shielding performance of VHT and VPHT aerogels as a function of thickness in the X band. Figure 5.6f shows the shielding efficiency of VHT and VPHT at two different thicknesses, 3 and 5 mm, at 12.4 GHz. It is evident that VHT samples exhibit mild shielding ability, less than the minimum practical requirement of 20 dB, even after increasing thickness. However, the VPHT aerogels showed strong EMI shielding potential that reaches up to 33.7 dB for a 5 mm sample (blocking above 99.9% of the incident waves). It must be notable that, although polymerization improves shielding efficiency much, there is only a slight variation in the reflection SE. This is because the aerogels preserve their structure and thereby support the concept of 'green shielding' by absorbing most incoming waves,

even after the polymerization (X. Wang *et al*., 2019). Further, the thickness variation of EMI SE of VPHT aerogels was also examined, and the results with total EMI SE at 8.2 and 12.4 GHz are shown in figure 5.7a. VPHT aerogels with thicknesses greater than 2 mm have potential shielding efficiency in the entire X band frequency region. Maximum SE reaches 51.27 dB at a sample thickness of 8 mm. Figure 5.7b shows the variation in the percentage of reflection and absorption shielding efficiency of VPHT with the thickness of the shield. The gradual increase in the rate of absorption SE with the thickness results from the layered morphology. From these results, we can infer that the homogeneous morphology of gels is not lost even while thinning down the shield, which plays a crucial role in determining EMI SE apart from conductivity.

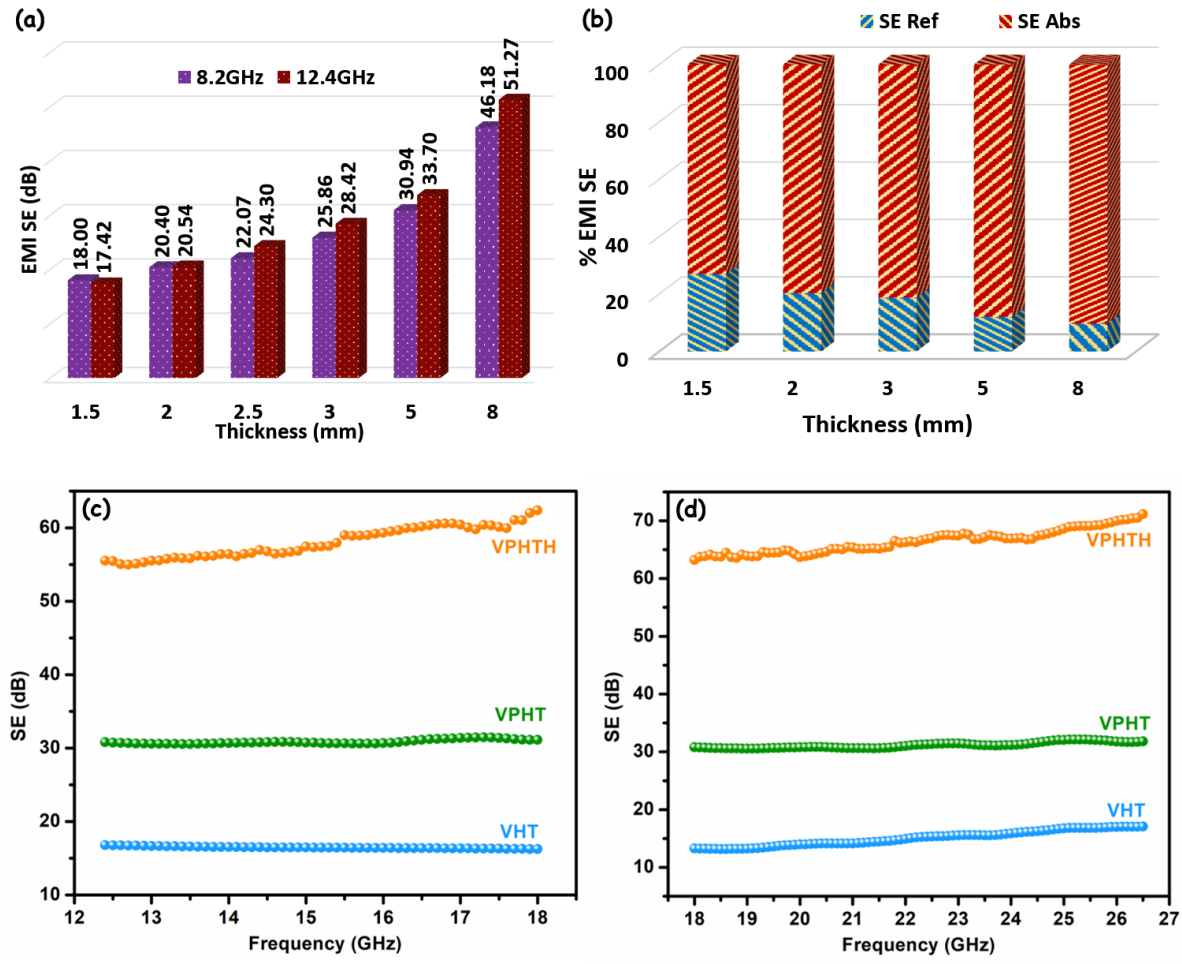

Figure ***5.7*** *(**a**) Variation of EMI SE of VPHT aerogels at different thicknesses at start and end frequencies of X band. (**b**) Percentage contribution of reflection and absorption shielding effectiveness of VPHT towards total shielding efficiency as a function of shield thickness at 8.2 GHz; Frequency-dependent variation of total EMI shielding effectiveness of aerogels over (**c**) Ku band and (**d**) K band.*

Further, the total shielding performance of aerogels with 3 mm thickness was studied in 12.4-18 GHz (Ku-band) and 18-26.5 GHz (K-band) (figure 5.7c&d). Polymerized gels exhibit EMI SE_{Total} values greater than 28 dB (equivalent to >99.84% of the incident waves are blocked by the shield) with a density of only ~0.04 g/cm^3 in the entire frequency span Ku and K band. They present exceptional EMI SE values of >55 dB in the Ku band frequency span and >63 dB in the K band. The highest shielding performance of 71.1 dB is achieved at 26.5 GHz, which indicates that a meager <0.0000078% of incident radiation power is transmitted through the shield, whereas the vast majority is shielded through absorption or reflection.

Figure 5.8 shows the detailed shielding performance of VPHT and VPHTH aerogels in Ku and K bands. Absorption shielding efficiency values of VPHT and VPHTH reach maxima of 28.5 and 66.0 dB, respectively, at the far end of the frequency span, 26.5 GHz. The declining and inclining trends of absorption and reflection SE with frequency are evident from the direct relationship between frequency and respective shielding efficiency in equations 4.1 and 4.2. Compared to VHT, the absorption SE of VPHT increased by ~2 times while that of VPHTH by ~5 times in the measured frequency span. On average, the percentage contribution of absorption SE to total SE for VPHT and VPHTH are ~95%, 93% in the Ku band, and 86%, 91% in the K band. Hence the aerogels preserve greenness by absorbing most of the EM waves in all three frequency bands, even after the polymerization. The principal driver for high absorbance is the porous morphology of gel inside which the EM wave is internally reflected multiple times and completely attenuated. Moreover, the interfacial polarization in the pore boundaries will improve the dielectric loss. Thus, most of the incident radiation will be infiltrated to aerogels' depth, resulting in increased SE_{Abs}.

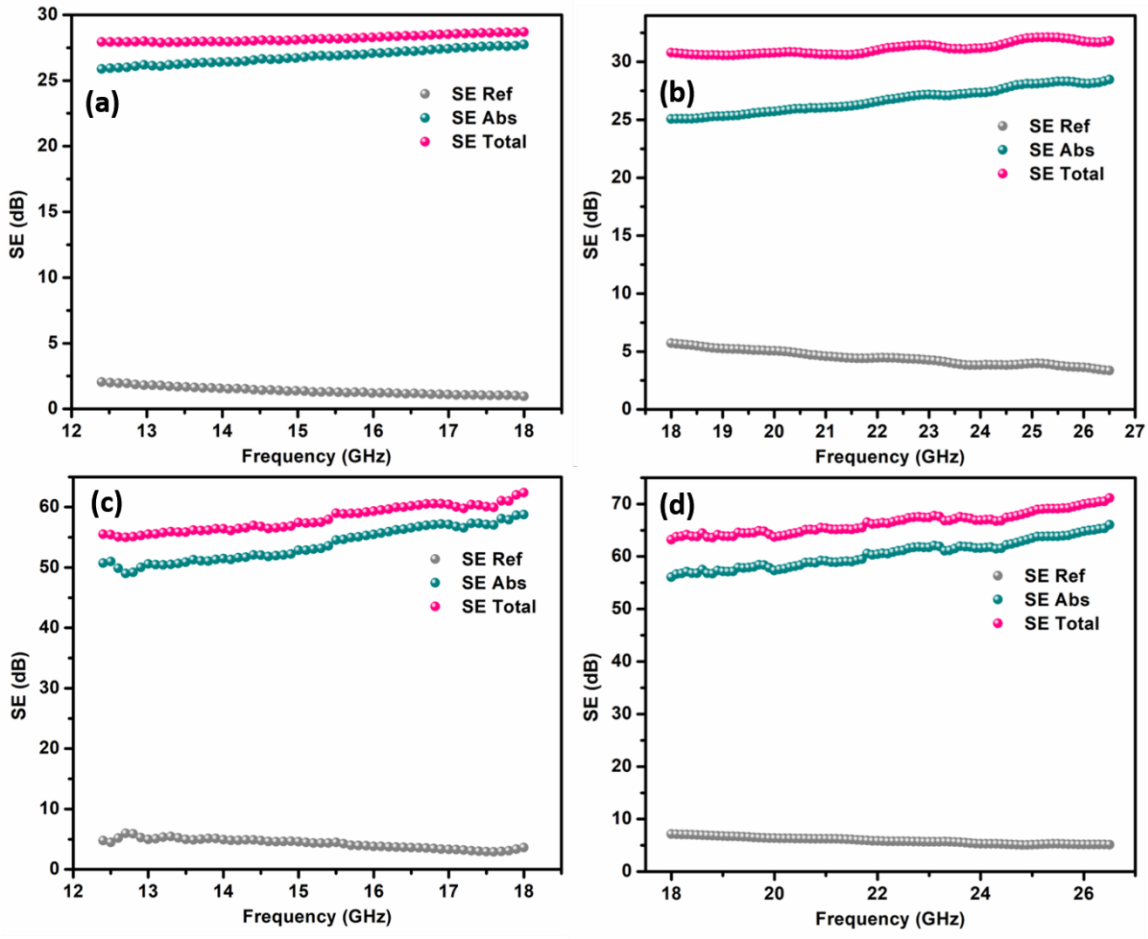

*Figure **5.8** Frequency-dependent variation of total EMI shielding effectiveness (SE_{Total}), reflection shielding effectiveness (SE_{Ref}), and absorption shielding effectiveness (SE_{Abs}) of (**a**) VPHT and (**b**) VPHTH over Ku band; (**c**) VPHT and (**d**) VPHTH over K band.*

Notably, the specific shielding effectiveness (SSE = Total SE/density) is a crucial term for low dense and porous shielding materials used in avionic applications. The bar diagram (figure 5.9a) shows the specific shielding performance and SSE/thickness of aerogels at the highest frequency of each X, Ku, and K band. SSE of VHT and VPHT comes around 800 dB cm^2/g, while that of VPHTH exceeds 1300 dB cm^2/g in the entire bandwidth. SSE/thickness of VPHTH increases from 4463 dB cm^2/g in the X band to 5929 dB cm^2/g in the K band. These values exceed most of the other reported SSEs of aerogels. Figure 5.9b compares the SSE of shielding materials reported in the literature, highlighting ultra-low-dense aerogels' excellent shielding nature. The corresponding shielding values are shown in Table 5.1. Other than the works displayed here, no other aerogels reported higher SSE without employing either carbonaceous or MXene fillers, to the best of our knowledge (Bian *et al*., 2019; Hu *et al*., 2020; Zeng *et al*., 2020). Nonetheless, the cost-

effective, straightforward and facile synthesis protocol makes our V_2O_5- PANI aerogels a promising candidate in the field of lightweight EMI shielding materials.

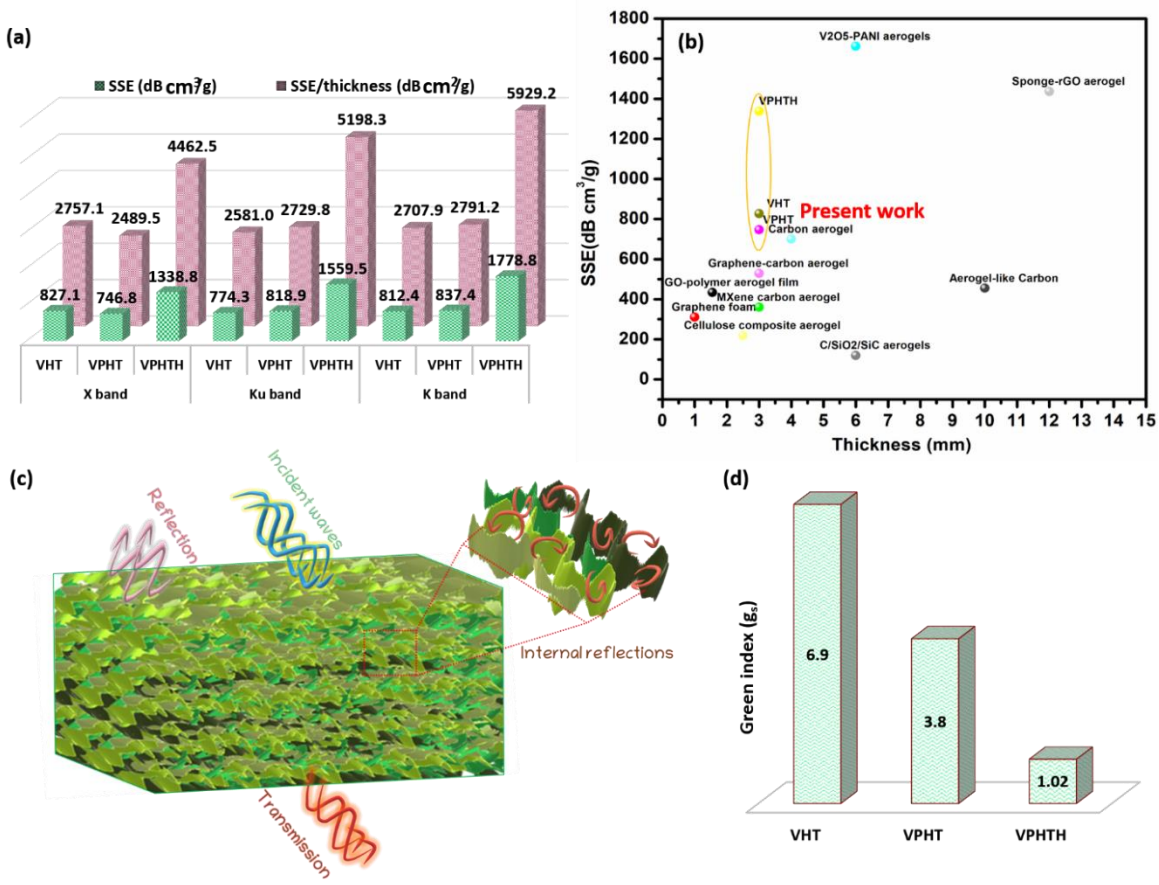

*Figure **5.9** (**a**) SE/density (SSE) and SSE/ thickness of VHT, VPHT, and VPHTH aerogels in X, Ku, and K bands; and (**b**) **c**omparison of EMI shielding performance of aerogels in X band with the reported porous materials. SSE versus the thickness of different materials. References in the graph are given in Table 5.1; (**c**) An illustration of a possible shielding mechanism and (**d**) the bar diagram showing the green index of aerogels at 10 GHz.*

The shielding mechanism of the present shield can be pictorially visualized as given in figure 5.9c. Macropores on the aerogel surface administer the incident EM waves entering the aerogel by partial reflection due to impedance mismatch at the surface and partial absorption. The unfiltered portion of the waves is trapped inside the macro and mesopores in the 3D skeleton of nanowires. Here, hierarchical porosity helps mitigate these EM waves by providing more surface area for scattering and long paths to maneuver the waves through multiple internal reflections. In other words, the folds and inner voids in the V_2O_5-PANI layers can multiply the propagation path length of electromagnetic waves and

enhance the interfacial polarization, thereby augmenting the EMI shielding performance. On top of this, the conducting skin formed by polymer on V_2O_5 nanowires further enhances the electron transfer channels and thus promotes charge transfer which decays EM energy. Also, the defects and dangling bonds inside the porous composite structure can induce charge asymmetric distribution, producing polarization centers that absorb electromagnetic energy. In short, the synergistic effects of porosity governed microstructure of PANI -V_2O_5 play a significant role in the overall shielding performance of composite aerogels.

*Table **5.1** A comparative analysis of specific shielding effectiveness values of porous materials measured in X-band.*

Sl No	**Sample name**	**EMI SE (dB)**	**Thick-ness (mm)**	**SSE (dB cm^3/g)**	**SSE/ thickness (dB cm^2/g)**	**Ref**
1	Aerogel-like Carbon	51	10	455	455.0	(Y. Q. Li *et al*., 2015)
2	Carbon aerogel	40	4	700	1750.0	(Vazhayal *et al*., 2020)
3	C/SiO_2/SiC aerogels	24	6	120	200.0	(An *et al*., 2019)
4	GO-polymer aerogel film	53	1.55	434	2800.0	(Han *et al*., 2016)
5	Sponge-supported rGO aerogel	27.3	12	1437	1197.5	(C. Liu *et al*., 2016)
6	MXene carbon aerogel	71.3	3	360	1200.0	(Liang *et al*., 2020)
7	Cellulose composite aerogel	20.8	2.5	219	876.0	(H. D. Huang *et al*., 2015)
8	Graphene foam	56	1	311.0	3110	(Xing *et al*., 2019)
9	CuNi-CNT foam	54.6	1.5	237.4	1582.7	(Ji *et al*., 2014)
10	Graphene-carbon aerogel	37	3	529	1763.3	(W. L. Song *et al*., 2015)

11	V_2O_5-PANI aerogels	34.7	6	1662.2	2770.3	(Puthiyedath Narayanan *et al*., 2021)
12	VPHT	28.4	3	746.8	2489.5	**Present work**
13	VPHTH	53.6	3	1338.8	4462.5	**Present work**
14	VHT	17.4	3	827.1	2757.1	**Present work**

Several publications report light and thin EMI shields, but few probe into high-performing shields with simultaneous environment friendliness, which is relevant in modern times. Previous chapters show that a 'green' EMI shield protects an intended system/area from unwanted radiations without sending hazardous secondary reflections back to the surrounding environment (X. Wang *et al*., 2019). We calculated the green index (g_s), the parameter portraying the ecological value of a shield and defined as:

$$g_s = \frac{1-{S_{12}}^2}{{S_{11}}^2} - 1 \tag{5.3}$$

A high green index needs more absorption loss with shallow reflection. High shielding demands good conducting properties, which causes more reflection. Hence, developing a pollution-free shield with excellent shielding property is arduous. Figure 5.9d depicts the green index of aerogels at 10 GHz. VHT and VPHT display high g_s >3 mainly due to their low conductivity and porous structure. Meanwhile, VPHTH has a lower but good green value of 1.02. A shield can be considered green and efficient if g_s>1 and EMI SE>30 dB (X. Wang *et al*., 2019). We can say that VPHTH has optimum EMI SE and green index values. The chemically engineered microstructure of aerogel is the main driver for bringing synergy between superior shielding and eco-friendliness. Also, good impedance matching between the aerogel and incident waves helps to absorb a significant portion of incoming waves and thus contributes to a high green index value. It is notable that, among the studied green EMI shielding aerogels, VPHTH shows exceptional shielding performance with >91% of absorption in the entire measured frequency band. The rare combination of outstanding SE, ultra-low density, and optimal green index of VPHTH make it a unique, carbon-less choice of lightweight shields, perfectly fitting for military, aerospace, and portable applications.

5.4 Conclusions

In summary, V_2O_5-PANI aerogels were successfully fabricated via a novel economic strategy wherein V_2O_5 hydrogel was initially synthesized by the simple one-pot hydrothermal method, which was subsequently reinforced by polyaniline, followed by the freeze-drying process to obtain vanadium pentoxide- polyaniline aerogels. The spectroscopic analyses revealed the effects of polymerization that reinforced the 3D architecture made of V_2O_5 nanowires. The microstructural analysis confirms that the aerogels display highly layered and porous architecture that can provide absorption dominant shielding performance. Thermogravimetric data suggests that the content of the polymer is highest in acid polymerized aerogel, which obviously can improve the conductivity. The electrical conductivity measurement supports this observation with the highest conductivity (~5.1 S/cm) among the three aerogels (VHT, VPHT, and VPHTH) for VPHTH. This is due to the higher protonation of polymer in the presence of the acid medium. Upon polymerization, the BET surface area was found to be three times that of VHT (~23 m^2 /g). V_2O_5-PANI aerogels polymerized in acid environment show maxima of 53.6 and 66.0 dB in X and Ku bands, respectively. The stunning electromagnetic performance of 71.2 dB at 26.5 GHz in the K band at a very low density of 0.04 g/cm^3, is really remarkable. This impressive show of microwave attenuation indicates that a meager <0.0000078% of incident radiation power is only transmitted through the shield, whereas the vast majority is shielded through either absorption or reflection. This systematic investigation suggests that the hydrothermally derived aerogels' high conductivity and porous architecture are mainly responsible for the shielding performance. The brilliantly engineered aerogels morphology brings together the rare combination of eco-friendliness and superior shielding ability. Moreover, the aerogels contain neither carbonaceous fillers nor metallic particles, making them hazardless shielding structures. The relatively facile synthesis protocol used in the present research provides vital hints to cost-effectively creating excellent green shields.

Chapter 6

Conclusions and future scope

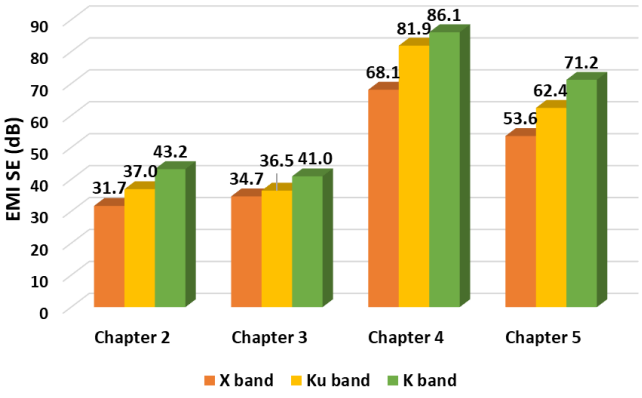

The chapter summarises the main research outcomes of the present doctoral investigation. It also includes the weaknesses in this study and future recommendations.

6.1 Summary

Owing to the complex synthetic procedures involved, realizing lightweight EMI shielding aerogels without employing carbonaceous materials as the chief filler component is highly challenging. Green electromagnetic interference shielding materials are the most promising among EM wave attenuating solutions by virtue of their less environmental burden resulting from efficiently attenuating spurious waves with minimal secondary reflection. Against this background, the present doctoral study tries to establish a few facile strategies for developing aerogels-based EM wave absorbers using V_2O_5 as the skeletal nanowire matrix. Herein, novel ultralight aerogels were prepared by innovative polycondensation and hydrothermal approaches. The resultant nanowire fortified architectures showed impressive shielding effectiveness, far greater than the commercial standard of 20 dB. The significant findings from each chapter are summarized below:

- Our earlier efforts were dedicated to synthesizing carbonized V_2O_5 aerogels through simple hydrothermal carbonization of V_2O_5 nanofibers, using a cheap carbon source, D-glucose. The highly porous aerogels with a density of 0.026 g/cm^3 exhibit high specific surface area (48.2 m^2/g) and good electrical conductivity (0.133 S/cm). The rigid three-dimensional (3D) conductive networks inside the aerogel simultaneously support EM wave dissipation through multiple internal reflections and reduce shield density. High shielding efficiency (SE) was achieved in X, Ku, and K bands with a maximum EMI SE of 43.24 dB at 26.5 GHz. Exceptional specific shielding efficiency of 1544 dB cm$^{3/}$g was achieved in the K band with a high green index of 1.58. These results explore the possibility of using a conducting polymer to reinforce the V_2O_5 nanowire skeleton instead of carbonization.
- With the intention of reducing the graphitic carbon content in the aerogels, conducting polymer polyaniline was carefully introduced into the V_2O_5 nanowire dispersion to impart electrical conductivity and structural reinforcement in the aerogel. The morphology of the pure V_2O_5 aerogel is precisely copied in the V_2O_5- PANI composite aerogel but with added mechanical strength. The mesoporous aerogel has a very low density of ~0.02 g/cm^3. A detailed investigation was carried out to understand the variation of shielding effectiveness with the aging of V_2O_5 nanofiber dispersion. The results show that aerogels made of ~30 days aged dispersion has the maximum EMI shielding efficiency of 34 dB in the X band, with an impressive specific shielding

efficiency of 1662.2 dB cm^3/g. The maximum EMI SE reaches ~41 dB in the K band with a 6 mm thick gel, and the corresponding SSE is 1950.5 dB cm^3/g. The green index (g_s) of V_2O_5-PANI aerogel is among the highest so far (~2.91), but the shielding efficiency can be further improved through a drastic modification of the polymerization conditions.

- As polymerization will be complete only in an intense acid atmosphere, V_2O_5-PANI@HCl composite aerogels were prepared, and remarkable differences in morphology as well as in shielding properties were observed. Herein, a meticulously designed 3-dimensional array of V_2O_5 nanofibers was reinforced by polyaniline (PANI) in the presence of hydrochloric acid and obtained a meso-macroporous structure. The aging of V_2O_5 dispersion and acid concentrations were optimized to get maximum shielding performance. The composite aerogel with ~35 days of aging showed exceptional shielding effectiveness of 68.1 dB in X-band, with a steady bandwidth. Even in the K band, a stunning shielding performance with a maximum of 86.1 dB was displayed, which can be translated to a specific shielding efficiency of 2777.4 dB cm^3/g. Having got high shielding parameters, our efforts are further directed to simplify the synthesis protocol.
- Fabricating the aerogels via several week-long procedures is sluggish and needs to be decluttered. Hence, in the final working chapter, we attempted to prepare a V_2O_5-PANI aerogel within a few days without compromising the shielding characteristics. V_2O_5 hydrogel was synthesized via a simple one-pot hydrothermal route, and the nanowire network inside this gel was polymerized by aniline. Aerogels obtained after freeze-drying exhibited improved mechanical properties and showed excellent shielding performance (71.2 dB in K band), superior specific shielding efficiency (1338.8 dB cm^3/g), and good green index (1.02). The porous structure of the materials and successful incorporation of polyaniline was confirmed by scanning electron microscopy and various spectroscopic analyses. This work opens the door to numerous facile pathways involving hydrothermal conditions through which robust, lightweight shielding solutions can be evolved.

Our research findings demonstrate that hierarchically porous three-dimensional (3D) architecture realized through meticulous control of synthesis conditions can lead to impressively high shielding performance. Few aerogels could show exceptional electromagnetic interference (EMI) shielding above 60 dB with broad bandwidth without employing costly metallic, carbonaceous, or MAX phase fillers. Noteworthy is the fact that

we could achieve this goal by using relatively budget-friendly layered oxide, V_2O_5. All the aerogels discussed in this work have ample mechanical strength and absorption dominant shielding efficiency in the entire X, Ku, and K band frequency ranges. Layered and porous morphology, the electrical conductivity of composites, and the synergistic effect of the constituents are the main reasons for the promising shielding capacity of aerogels. V_2O_5-based aerogels prepared through the hydrothermal synthesis route disgorged less chemical waste and exhibited a high green index. In a nutshell, this thesis proves that simple and cost-effective strategies can prepare light, eco-friendly aerogels with supreme shielding properties.

6.2 Scope for future research

- In the present thesis work, we tried only one conducting polymer, polyaniline, to impart conductivity in composite aerogels. V_2O_5- based aerogels with other conducting polymers (e.g., Polypyrrole) can also be prepared and tested for absorption dominant green shielding performance.
- Though the aerogels have good load-bearing capacity, improving their mechanical strength and machinability is desirable. In order to achieve better strength, synthetic strategy is to be modified- possibly using bio-materials (like reinforcement of materials like an eggshell membrane)- such that it does not damage the micro architecture of the aerogels.
- The effect of incorporating magnetic nanofillers, say ferrite or Ni nanostructures, in improving shielding efficiency through magnetic loss is a novel horizon to be explored.
- Temperature-dependent variation of shielding efficiency of the prepared aerogels is to be studied. This information is helpful for applications in the 5G communication regime.
- Knowing the electric and magnetic properties of the constituent components (V_2O_5 and PANI), the shielding effectiveness of the composite can be modelled using COMSOL Multiphysics software, and the results can be compared with the experimental values.
- Nowadays, multifunctional materials always have the upper hand in every commercial sector. For example, an EMI shield cum sensor, a shield with fire-retardancy, a shield with some switching properties, energy harvesting shields, etc.,

will be more interesting. Such possibilities can be explored using the high EMI shielding parameters of the present aerogels.

List of publications

1. Aerogels of V_2O_5 nanowires reinforced by polyaniline for electromagnetic interference shielding, **Aparna Puthiyedath Narayanan**, K.N. Narayanan Unni, Kuzhichalil Peethambharan Surendran. Chemical Engineering Journal 408C (2021) 127239. https://doi.org/10.1016/j.cej.2020.127239.

2. Acid Polymerized V_2O_5-PANI Aerogels with Outstanding Specific Shielding Effectiveness in X, Ku and K Bands. **Aparna Puthiyedath Narayanan**, Kuzhichalil Peethambharan Surendran. Journal of Industrial and Engineering Chemistry (2022). https://doi.org/10.1016/j.jiec.2022.08.039

3. Outstanding Electromagnetic Interference Shielding in Hydrothermally Derived Divanadium Pentoxide -Polyaniline Aerogels. **Aparna Puthiyedath Narayanan**, Kuzhichalil Peethambharan Surendran. J. Mater. Chem. C 10 (2022) 14754-14769. https://doi.org/10.1039/D2TC03168J

4. Carbonized V_2O_5 aerogels – green EMI solution with broad band width. **Aparna Puthiyedath Narayanan**, Kuzhichalil Peethambharan Surendran. (Under review)

5. GO - V_2O_5 aerogels with exceptional EMI shielding performance in X, Ku, and K bands. **Aparna Puthiyedath Narayanan**, Kuzhichalil Peethambharan Surendran. (To be communicated)

6. Light and thin copper aerogels with superior shielding efficiency. **Aparna Puthiyedath Narayanan**, Alan Mathew Antony, Kuzhichalil Peethambharan Surendran. (To be communicated)

7. Room-Temperature Ferromagnetic $Sr_3YCo_4O_{10+\delta}$ and Carbon Black- Reinforced Polyvinylidenefluoride Composites toward High- Performance Electromagnetic Interference Shielding, Vidhya Lalan, **Aparna Puthiyedath Narayanan**, Kuzhichalil Peethambharan Surendran, and Subodh Ganesanpotti. ACS Omega 4 (2019) 8196−8206. 10.1021/acsomega.9b00454.

List of papers presented in conferences

1. **Aparna Puthiyedath Narayanan**, Kuzhichalil Peethambharan Surendran, Lightweight aerogels for green electromagnetic interference shielding, **Poster** presentation in Third International Conference on Advanced Functional Materials (ICAFM 2019), organized by CSIR – National Institute for Interdisciplinary Science and Technology (NIIST), Thiruvananthapuram on 9^{th} and 10^{th} Decemer, 2019.
2. **Aparna Puthiyedath Narayanan**, Kuzhichalil Peethambharan Surendran, Conducting Polymer Composite Aerogel for Electromagnetic Interference Shielding, **Poster** presentation in International Conference on Physics of Materials and Nanotechnology (ICPN 2021), organized by Mangalore University Department of Physics on 28^{th} – 30^{th} October, 2021
3. **Aparna Puthiyedath Narayanan**, Kuzhichalil Peethambharan Surendran, Carbonized V_2O_5 Aerogels with Exceptional Specific EMI Shielding, **Oral** presentation in National Webinar on Recent Advances in the Physics of Materials (RAPM-2021), organized by CSIR – National Institute for Interdisciplinary Science and Technology (NIIST) on 9^{th} -10^{th} December, 2021.
4. **Aparna Puthiyedath Narayanan**, Kuzhichalil Peethambharan Surendran, Ultra-light Polymer Composite Aerogels with Exceptional Specific EMI Shielding, **Poster** presentation in National Conference on Materials Science and Technology (NCMST-2021), organized by Department of Chemistry, Indian Institute of Space Science and Technology, Thiruvananthapuram on 29^{th} – 30^{th} December 2021.
5. **Aparna Puthiyedath Narayanan**, Kuzhichalil Peethambharan Surendran, Ultra-light Polymer Composite Aerogels with Exceptional Specific EMI Shielding, **Oral** presentation in International Conference on Materials -Properties Measurements and Applications (ICMPMA- 2022), organized by Fatima Mata National College, Kollam on 9^{th} – 13^{th} May 2022

REFERENCES

Abbasi, H., Antunes, M., & Velasco, J. I. (2019). Recent advances in carbon-based polymer nanocomposites for electromagnetic interference shielding. *Progress in Materials Science*, *103*(February), 319–373. https://doi.org/10.1016/j.pmatsci.2019.02.003

Abd-alghafour, N. M., Ahmed, N. M., & Hassan, Z. (2016). Sensors and Actuators A : Physical Fabrication and characterization of V_2O_5 nanorods based metal – semiconductor – metal photodetector. *Sensors & Actuators: A. Physical*, *250*, 250–257. https://doi.org/10.1016/j.sna.2016.09.001

Abd-Alghafour, N. M., Naeem, G. A., & Mohammad, S. M. (2020). Dependence of V_2O_5 Nanorods Properties on Substrate Type Prepared by Simple Hydrothermal Method. *Journal of Physics: Conference Series*, *1535*(1), 012046. https://doi.org/10.1088/1742-6596/1535/1/012046

Abolghasemi Mahani, A., Motahari, S., & Nayyeri, V. (2018). Synthesis, characterization and dielectric properties of one-step pyrolyzed / activated resorcinol-formaldehyde based carbon aerogels for electromagnetic interference shielding applications. *Materials Chemistry and Physics*, *213*, 492–501. https://doi.org/10.1016/j.matchemphys.2018.04.047

Agnihotri, N., Chakrabarti, K., & De, A. (2015). Highly efficient electromagnetic interference shielding using graphite nanoplatelet/poly(3,4-ethylenedioxythiophene)-poly(styrenesulfonate) composites with enhanced thermal conductivity. *RSC Advances*, *5*(54), 43765–43771. https://doi.org/10.1039/c4ra15674a

Ahirrao, D. J., Mohanapriya, K., & Jha, N. (2018). Bulk to nanostructured vanadium pentaoxide-nanowires (V_2O_5-NWs) for high energy density supercapacitors. *AIP Conference Proceedings*, *1942*, 140066. https://doi.org/10.1063/1.5029197

Ahmad, B., Khan, G. R., & Asokan, K. (2015). Role of substrate effects on the morphological, structural, electrical and thermoelectrical properties of V_2O_5 thin films. *RSC Advances*, *65*(5), 52602–52611. https://doi.org/10.1039/C5RA07542D

Ali Mohsin, M. E., Shrivastava, N. K., Arsad, A., Basar, N., & Hassan, A. (2020). The Effect of pH on the Preparation of Electrically Conductive and Physically Stable PANI/Sago Blend Film via in situ Polymerization. *Frontiers in Materials*, *7*(February), 1–11. https://doi.org/10.3389/fmats.2020.00020

Ameli, A., Nofar, M., Wang, S., & Park, C. B. (2014). Lightweight polypropylene/stainless-steel fiber composite foams with low percolation for efficient electromagnetic interference shielding. *ACS Applied Materials and Interfaces*, *6*(14), 11091–11100. https://doi.org/10.1021/am500445g

An, Z., Ye, C., Zhang, R., & Qu, Q. (2019). Multifunctional C/SiO_2/SiC-based aerogels and composites for thermal insulators and electromagnetic interference shielding. *Journal of Sol-Gel Science and Technology*, *89*(3), 623–633. https://doi.org/10.1007/s10971-019-04916-5

Bass, A. (2017). *Understanding the importance of EMI shielding in medical devices*. Vanguard Products. https://www.vanguardproducts.com/

Batrakov, K., Kuzhir, P., Maksimenko, S., Volynets, N., Voronovich, S., Paddubskaya, A., Valusis, G., Kaplas, T., Svirko, Y., & Lambin, P. (2016). Enhanced microwave-to-terahertz absorption in graphene. *Applied Physics Letters*, *108*(12). https://doi.org/10.1063/1.4944531

Bhadra, S., Khastgir, D., K.Singha, N., & HeeLee, J. (2009). Progress in preparation, processing and applications of polyaniline. *Progress in Polymer Science*, *34*(8, August), 783–810. https://doi.org/https://doi.org/10.1016/j.progpolymsci.2009.04.003

Bian, R., He, G., Zhi, W., Xiang, S., Wang, T., & Cai, D. (2019). Ultralight MXene-based aerogels with high electromagnetic interference shielding performance. *Journal of Materials Chemistry C*, *7*(3), 474–478. https://doi.org/10.1039/c8tc04795b

Cao, S. Y., Chen, C. S., Ning, X. T., Zeng, B., Xie, X. D., Chen, X. H., Wei, S. S., Mei, Y. P., & Zhao, G. J. (2013). Preparation and photocatalytic property of graphene/TiO_2 composite powder. *Integrated Ferroelectrics*, *145*(1), 40–45. https://doi.org/10.1080/10584587.2013.788362

Celozzi, S., Araneo, R., & Lovat, G. (2008). Electromagnetic Shielding. In *Wiley-Interscience*. John Wiley & Sons, Inc. https://doi.org/10.1002/9780470268483

Chen, G.-C., Shan, X.-Q., Wang, Y.-S., Wen, B., Pei, Z.-G., Xie, Y.-N., Liu, T., & Pignatello, J. J. (2009). Adsorption of 2,4,6-trichlorophenol by multi-walled carbon nanotubes as affected by Cu(II). *Water Research*, *43*(9), 2409–2418. https://doi.org/10.1016/j.watres.2009.03.002

Chen, K., Zhang, G., Xiao, L., Li, P., Li, W., Xu, Q., & Xu, J. (2021). Polyaniline Encapsulated Amorphous V_2O_5 Nanowire-Modified Multi-Functional Separators for Lithium–Sulfur Batteries. *Small Methods*, *5*(3), 2001056. https://doi.org/10.1002/smtd.202001056

Chen, Y., Pötschke, P., Pionteck, J., Voit, B., & Qi, H. (2020). Multifunctional Cellulose/rGO/Fe_3O_4 Composite Aerogels for Electromagnetic Interference Shielding. *ACS Applied Materials and Interfaces*, *12*(19), 22088–22098. https://doi.org/10.1021/acsami.9b23052

Chen, Y., Zhang, L., Yang, Y., Pang, B., Xu, W., Duan, G., Jiang, S., & Zhang, K. (2021). Recent Progress on Nanocellulose Aerogels: Preparation, Modification, Composite Fabrication, Applications. *Advanced Materials*, *33*(11). https://doi.org/10.1002/adma.202005569

Chen, Z., Xu, C., Ma, C., Ren, W., & Cheng, H.-M. (2013). Lightweight and Flexible Graphene Foam Composites for High-Performance Electromagnetic Interference Shielding. *Advanced Materials*, *25*(9), 1296–1300. https://doi.org/10.1002/adma.201204196

Chu, J., Kong, Z., Lu, D., Zhang, W., Wang, X., Yu, Y., Li, S., Wang, X., Xiong, S., & Ma, J. (2016). Hydrothermal synthesis of vanadium oxide nanorods and their electrochromic performance. *Materials Letters*, *166*, 179–182. https://doi.org/10.1016/j.matlet.2015.12.067

Clarivate. (2022). *Document search - Web of Science Core Collection*. Web of Science. https://www.webofscience.com/wos/woscc/basic-search

Cruz-Pacheco, A. F., Paredes-Madrid, L., Orozco, J., Gómez-Cuaspud, J. A., Batista-Rodríguez, C. R., & Gómez, C. A. P. (2020). Assessing the influence of the sourcing voltage on polyaniline composites for stress sensing applications. *Polymers*, *12*(5), 1164. https://doi.org/10.3390/POLYM12051164

Cybershield. (2017). *Medical Device EMI Shielding*. Cybershield. https://www.cybershieldinc.com/

Dalmaschio, C. J., Ribeiro, C., & Leite, E. R. (2010). Impact of the colloidal state on the oriented attachment growth mechanism. *Nanoscale*, *2*(11), 2336–2345. https://doi.org/10.1039/c0nr00338g

Demir-Cakan, R., Baccile, N., Antonietti, M., & Titirici, M.-M. (2009). Carboxylate-Rich Carbonaceous Materials via One-Step Hydrothermal Carbonization of Glucose in the Presence of Acrylic Acid. *Chemistry of Materials*, *21*(3), 484–490. https://doi.org/10.1021/cm802141h

Derkaoui, I., Khenfouch, M., Elmokri, I., Mothudi, B. M., Dhlamini, M. S., Moloi, S. J., Zorkani, I., Jorio, A., & Maaza, M. (2017). Structural and optical properties of hydrothermally synthesized vanadium oxides nanobelts. *IOP Conference Series: Materials Science and Engineering*, *186*, 012007. https://doi.org/10.1088/1757-899X/16/1/012007

Detsri, E., & Dubas, S. T. (2009). Interfacial Polymerization of Water-Soluble Polyaniline and Its Assembly Using the Layer-By-Layer Technique. *Journal of Metals, Materials and Minerals*, *19*(1), 39–44. http://www.material.chula.ac.th/Journal/v19-1/39-44 DETSRI.pdf

Dhawan, S. K., Ohlan, A., & Singh, K. (2011). Designing of Nano Composites of Conducting Polymers for EMI Shielding. In *Advances in Nanocomposites - Synthesis, Characterization and Industrial Applications* (pp. 429–482). InTech. https://doi.org/10.5772/14752

Dhoundiyal, H., Das, P., & Bhatnagar, M. C. (2021). Electrical and magnetic properties of V_2O_5 microstructure formed by self-assembled nanorods. *Physica B: Condensed Matter*, *603*(July 2020), 412622. https://doi.org/10.1016/j.physb.2020.412622

Dijith, K. S., Aiswarya, R., Praveen, M., Pillai, S., & Surendran, K. P. (2018). Polyol derived Ni and NiFe alloys for effective shielding of electromagnetic interference. *Materials Chemistry Frontiers*, *2*(10), 1829–1841. https://doi.org/10.1039/C8QM00264A

Dong, Y., Niu, X., Song, W., Wang, D., Chen, L., Yuan, F., & Zhu, Y. (2016). Facile Synthesis of Vanadium Oxide/Reduced Graphene Oxide Composite Catalysts for Enhanced Hydroxylation of Benzene to Phenol. *Catalysts*, *6*(5), 74. https://doi.org/10.3390/catal6050074

Dragoman, M., Braniste, T., Iordanescu, S., Aldrigo, M., Raevschi, S., Shree, S., Adelung, R., & Tiginyanu, I. (2019). Electromagnetic interference shielding in X-band with aero-GaN. *Nanotechnology*, *30*. https://doi.org/10.1088/1361-6528/ab2023

Du, Y., Xu, J., Fang, J., Zhang, Y., Liu, X., Zuo, P., & Zhuang, Q. (2022). Ultralight, highly compressible, thermally stable MXene/aramid nanofiber anisotropic aerogels for electromagnetic interference shielding. *Journal of Materials Chemistry A*, *10*(12), 6690–6700. https://doi.org/10.1039/D1TA11025J

Dubal, D. P., Dhawale, D. S., More, A. M., & Lokhande, C. D. (2011). Synthesis and characterization of photosensitive TiO_2 nanorods by controlled precipitation route. *Journal of Materials Science*, *46*(7), 2288–2293. https://doi.org/10.1007/s10853-010-5070-7

Fosong, W., Jinsong, T., Lixiang, W., Hongfang, Z., & Zhishen, M. (1988). Study on the Crystallinity of Polyaniline. *Molecular Crystals and Liquid Crystals Incorporating Nonlinear Optics*, *160*(1), 175–184. https://doi.org/10.1080/15421408808083012

Gadea, G., Morata, A., & Tarancon, A. (2018). Semiconductor Nanowires for Thermoelectric Generation. In S. Mokkapati & C. Jagadish (Eds.), *Nanowires for Energy Applications* (pp. 321–407). https://doi.org/10.1016/bs.semsem.2018.01.001

Gao, Q., Qin, J., Guo, B., Fan, X., Wang, F., Zhang, Y., Xiao, R., Huang, F., Shi, X., & Zhang, G. (2021). High-performance electromagnetic interference shielding epoxy/Ag nanowire/thermal annealed graphene aerogel composite with bicontinuous three-dimensional conductive skeleton. *Composites Part A: Applied Science and*

Manufacturing, *151*, 106648. https://doi.org/10.1016/j.compositesa.2021.106648

Geetha, S., Kumar, K. K. S., Rao, C. R. K., Vijayan, M., & Trivedi, D. C. (2009). EMI Shielding: Methods and Materials—A Review. *Journal of Applied Polymer Science*, *112*(4), 2073–2086. https://doi.org/10.1002/app.29812

Ghosh, P., & Chakrabarti, A. (2000). Conducting carbon black filled EVA vulcanizates: Assessment of dependence of physical and mechanical properties and conducting character on variation of filler loading. *Journal of Polymer Materials*, *17*(3), 291–304.

Golba, S., Popczyk, M., Miga, S., Jurek-Suliga, J., Zubko, M., Kubisztal, J., & Balin, K. (2020). Impact of acidity profile on nascent polyaniline in the modified rapid mixing process—material electrical conductivity and morphological study. *Materials*, *13*(22), 1–15. https://doi.org/10.3390/ma13225108

Gonschorek, K.-H., & Vick, R. (2010). Skin Effect and Shielding Theory of Schelkunoff. In *Electromagnetic Compatibility for Device Design and System Integration* (pp. 377–392). Springer Berlin Heidelberg. https://doi.org/10.1007/978-3-642-03290-5_17

Gopakumar, D. A., Pai, A. R., Pottathara, Y. B., Pasquini, D., Carlos De Morais, L., Luke, M., Kalarikkal, N., Grohens, Y., & Thomas, S. (2018). Cellulose Nanofiber-Based Polyaniline Flexible Papers as Sustainable Microwave Absorbers in the X-Band. *ACS Applied Materials and Interfaces*, *10*(23), 20032–20043. https://doi.org/10.1021/acsami.8b04549

Gotić, M., Popović, S., Ivanda, M., & Musić, S. (2003). Sol-gel synthesis and characterization of V_2O_5 powders. *Materials Letters*, *57*(21), 3186–3192. https://doi.org/10.1016/S0167-577X(03)00022-3

Han, D., Zhao, Y. H., Bai, S. L., & Ching Ping, W. (2016). High shielding effectiveness of multilayer graphene oxide aerogel film/polymer composites. *RSC Advances*, *6*(95), 92168–92174. https://doi.org/10.1039/c6ra20976a

Hasan, M., Ansari, M. O., Cho, M. H., & Lee, M. (2015). Ammonia sensing and DC electrical conductivity studies of p-toluene sulfonic acid doped cetyltrimethylammonium bromide assisted V_2O_5@polyaniline composite nanofibers. *Journal of Industrial and Engineering Chemistry*, *22*, 147–152. https://doi.org/10.1016/j.jiec.2014.07.002

Hassan, S., Baker, A. G., & Jafaar, H. (2012). A.C Electrical Conductivity for Polyaniline Prepered in Different Acidic Medium. *International Journal of Basic and Applied Science*, *1*(2), 338–348. https://doi.org/10.17142/ijbas-2012.1.2.22

Hu, P., Lyu, J., Fu, C., Gong, W. Bin, Liao, J., Lu, W., Chen, Y., & Zhang, X. (2020). Multifunctional Aramid Nanofiber/Carbon Nanotube Hybrid Aerogel Films. *ACS*

Nano, *14*(1), 688–697. https://doi.org/10.1021/acsnano.9b07459

Huang, H.-D., Liu, C.-Y., Zhou, D., Jiang, X., Zhong, G.-J., Yan, D.-X., & Li, Z.-M. (2015). Cellulose composite aerogel for highly efficient electromagnetic interference shielding. *Journal of Materials Chemistry A*, *3*(9), 4983–4991. https://doi.org/10.1039/C4TA05998K

Huang, H. D., Liu, C. Y., Zhou, D., Jiang, X., Zhong, G. J., Yan, D. X., & Li, Z. M. (2015). Cellulose composite aerogel for highly efficient electromagnetic interference shielding. *Journal of Materials Chemistry A*, *3*(9), 4983–4991. https://doi.org/10.1039/c4ta05998k

Huang, W., Humphrey, B. D., & Macdiarmid, A. G. (1986). Polyaniline , a Novel Conducting Polymer. *J. Chem. SOC., Faraday Trans.*, *82*, 2385–2400.

Huangfu, Y., Ruan, K., Qiu, H., Lu, Y., Liang, C., Kong, J., & Gu, J. (2019). Fabrication and investigation on the PANI/MWCNT/thermally annealed graphene aerogel/epoxy electromagnetic interference shielding nanocomposites. *Composites Part A: Applied Science and Manufacturing*, *121*(March), 265–272. https://doi.org/10.1016/j.compositesa.2019.03.041

Huguenin, F., Gambardella, M. T. do P., Torresi, R. M., Córdoba de Torresi, S. I., & Buttry, D. A. (2000). Chemical and Electrochemical Characterization of a Novel Nanocomposite Formed from V_2O_5 and Poly(N-propane sulfonic acid aniline), a Self-Doped Polyaniline. *Journal of The Electrochemical Society*, *147*(7), 2437. https://doi.org/10.1149/1.1393550

Huo, J., Wang, L., & Yu, H. (2009). Polymeric nanocomposites for electromagnetic wave absorption. *Journal of Materials Science*, *44*(15), 3917–3927. https://doi.org/10.1007/s10853-009-3561-1

Ibris, N., Salvi, A. M., Liberalore, M., Decker, F., & Surca, A. (2005). XPS study of the Li intercalation process in sol-gel-produced v 2O5 thin film: Influence of substrate and film synthesis modification. *Surface and Interface Analysis*, *37*(12), 1092–1104. https://doi.org/10.1002/sia.2084

Ji, K., Zhao, H., Zhang, J., Chen, J., & Dai, Z. (2014). Fabrication and electromagnetic interference shielding performance of open-cell foam of a Cu-Ni alloy integrated with CNTs. *Applied Surface Science*, *311*, 351–356. https://doi.org/10.1016/j.apsusc.2014.05.067

Jiang, H., Wei, Z., Cai, X., Lai, L., Ma, J., & Huang, W. (2019). A cathode for Li-ion batteries made of vanadium oxide on vertically aligned carbon nanotube arrays/graphene foam. *Chemical Engineering Journal*, *359*(October), 1668–1676. https://doi.org/10.1016/j.cej.2018.10.223

Jiao, Y., Wan, C., Zhang, W., Bao, W., & Li, J. (2019). Carbon fibers encapsulated with nano-copper: A core–shell structured composite for antibacterial and electromagnetic interference shielding applications. *Nanomaterials*, *9*(3). https://doi.org/10.3390/nano9030460

Jin, L., Jiang, Y., Zhang, M., Li, H., Xiao, L., Li, M., & Ao, Y. (2018). Oriented Polyaniline Nanowire Arrays Grown on Dendrimer (PAMAM) Functionalized Multiwalled Carbon Nanotubes as Supercapacitor Electrode Materials. *Scientific Reports*, *8*(1), 1–10. https://doi.org/10.1038/s41598-018-24265-7

John, A., Mahadeva, S. K., & Kim, J. (2010). The preparation, characterization and actuation behavior of polyaniline and cellulose blended electro-active paper. *Smart Materials and Structures*, *19*(4), 045011. https://doi.org/10.1088/0964-1726/19/4/045011

Joseph, N., Varghese, J., & Sebastian, M. T. (2015). Self assembled polyaniline nanofibers with enhanced electromagnetic shielding properties. *RSC Advances*, *5*(26), 20459–20466. https://doi.org/10.1039/C5RA02113H

Joseph, N., Varghese, J., & Sebastian, M. T. (2016). A facile formulation and excellent electromagnetic absorption of room temperature curable polyaniline nanofiber based inks. *Journal of Materials Chemistry C*, *4*(5), 999–1008. https://doi.org/10.1039/C5TC03080C

Karatchevtseva, I., Zhang, Z., Hanna, J., & Luca, V. (2006). Electrosynthesis of Macroporous Polyaniline - V_2O_5 Nanocomposites and Their Unusual Magnetic Properties. *Chem. Mater.*, *18*(4), 4908–4916. https://doi.org/10.1021/cm052821e

Koo, C. M., Sambyal, P., Iqbal, A., Shahzad, F., & Hong, J. (2021). EMI Shielding Mechanism and Conversion Techniques. In *Two-Dimensional Materials for Electromagnetic Shielding* (1st ed., pp. 25–48). Wiley. https://doi.org/10.1002/9783527829828.ch2

Krumeich, F., Muhr, H.-J., Niederberger, M., Bieri, F., Schnyder, B., & Nesper, R. (1999). Morphology and Topochemical Reactions of Novel Vanadium Oxide Nanotubes. *Journal of the American Chemical Society*, *121*(36), 8324–8331. https://doi.org/10.1021/ja991085a

Kumar, R., Sharma, A., Pandey, A., Chaudhary, A., Dwivedi, N., Shafeeq M, M., Mondal, D. P., & Srivastava, A. K. (2020). Lightweight carbon-red mud hybrid foam toward fire-resistant and efficient shield against electromagnetic interference. *Scientific Reports*, *10*(1), 1–12. https://doi.org/10.1038/s41598-020-66929-3

Kundu, S., Satpati, B., Kar, T., & Pradhan, S. K. (2017). Microstructure characterization of hydrothermally synthesized PANI/$V_2O_5{\cdot}nH_2O$ heterojunction photocatalyst for

visible light induced photodegradation of organic pollutants and non-absorbing colorless molecules. *Journal of Hazardous Materials*, *339*(June), 161–173. https://doi.org/10.1016/j.jhazmat.2017.06.034

Lalan, V., & Ganesanpotti, S. (2022). The smallest anions, induced porosity and graphene interfaces in C12A7:e- electrides: a paradigm shift in electromagnetic absorbers and shielding materials. *Journal of Materials Chemistry C*, *10*(3), 969–982. https://doi.org/10.1039/D1TC03762E

Lalan, V., Puthiyedath Narayanan, A., Surendran, K. P., & Ganesanpotti, S. (2019). Room-Temperature Ferromagnetic $Sr_3YCo_4O_{10+\delta}$ and Carbon Black-Reinforced Polyvinylidenefluoride Composites toward High-Performance Electromagnetic Interference Shielding. *ACS Omega*, *4*(5), 8196–8206. https://doi.org/10.1021/acsomega.9b00454

Lewczuk, B., Redlarski, G., Zak, A., Ziółkowska, N., Przybylska-Gornowicz, B., & Krawczuk, M. (2014). Influence of electric, magnetic, and electromagnetic fields on the circadian system: Current stage of knowledge. *BioMed Research International*, *2014*, 13. https://doi.org/10.1155/2014/169459

Li, C. B., Li, Y. J., Zhao, Q., Luo, Y., Yang, G. Y., Hu, Y., & Jiang, J. J. (2020). Electromagnetic Interference Shielding of Graphene Aerogel with Layered Microstructure Fabricated via Mechanical Compression. *ACS Applied Materials and Interfaces*, *12*(27), 30686–30694. https://doi.org/10.1021/acsami.0c05688

Li, G. P., & Luo, Y. J. (2007). Hydrothermal preparation of ZnS nanowires. *Chinese Journal of Inorganic Chemistry*, *23*(11), 1864–1868.

Li, M., Han, F., Jiang, S., Zhang, M., Xu, Q., Zhu, J., Ge, A., & Liu, L. (2021). Lightweight Cellulose Nanofibril/Reduced Graphene Oxide Aerogels with Unidirectional Pores for Efficient Electromagnetic Interference Shielding. *Advanced Materials Interfaces*, *8*(24), 1–11. https://doi.org/10.1002/admi.202101437

Li, M., Kong, F., Wang, H., & Li, G. (2011). Synthesis of vanadium pentoxide (V_2O_5) ultralong nanobelts via an oriented attachment growth mechanism. *CrystEngComm*, *13*, 5317–5320. https://doi.org/10.1039/c1ce05477e

Li, M., Li, W., & Liu, S. (2011). Hydrothermal synthesis, characterization, and KOH activation of carbon spheres from glucose. *Carbohydrate Research*, *346*(8), 999–1004. https://doi.org/10.1016/j.carres.2011.03.020

Li, D. Sen, Wang, S. J., Zhou, Y., & Jiang, L. (2022). Lightweight and hydrophobic Ni/GO/PVA composite aerogels for ultrahigh performance electromagnetic interference shielding. *Nanotechnology Reviews*, *11*(1), 1722–1732. https://doi.org/10.1515/ntrev-2022-0088

Li, X. H., Li, X., Liao, K. N., Min, P., Liu, T., Dasari, A., & Yu, Z. Z. (2016). Thermally Annealed Anisotropic Graphene Aerogels and Their Electrically Conductive Epoxy Composites with Excellent Electromagnetic Interference Shielding Efficiencies. *ACS Applied Materials and Interfaces*, *8*(48), 33230–33239. https://doi.org/10.1021/acsami.6b12295

Li, Y., Chen, Y., He, X., Xiang, Z., Heinze, T., & Qi, H. (2022). Lignocellulose nanofibril/gelatin/MXene composite aerogel with fire-warning properties for enhanced electromagnetic interference shielding performance. *Chemical Engineering Journal*, *431*(P1), 133907. https://doi.org/10.1016/j.cej.2021.133907

Li, Y., Li, C., Zhao, S., Cui, J., Zhang, G., Gao, A., & Yan, Y. (2019). Facile fabrication of highly conductive and robust three-dimensional graphene/silver nanowires bicontinuous skeletons for electromagnetic interference shielding silicone rubber nanocomposites. *Composites Part A: Applied Science and Manufacturing*, 101–110. https://doi.org/10.1016/j.compositesa.2019.01.025

Li, Y. Q., Samad, Y. A., Polychronopoulou, K., & Liao, K. (2015). Lightweight and Highly Conductive Aerogel-like Carbon from Sugarcane with Superior Mechanical and EMI Shielding Properties. *ACS Sustainable Chemistry and Engineering*, *3*(7), 1419–1427. https://doi.org/10.1021/acssuschemeng.5b00340

Liang, C., Qiu, H., Han, Y., Gu, H., Song, P., Wang, L., Kong, J., Cao, D., & Gu, J. (2019). Superior electromagnetic interference shielding 3D graphene nanoplatelets/reduced graphene oxide foam/epoxy nanocomposites with high thermal conductivity. *Journal of Materials Chemistry C*, *7*(9), 2725–2733. https://doi.org/10.1039/C8TC05955A

Liang, C., Qiu, H., Song, P., Shi, X., Kong, J., & Gu, J. (2020). Ultra-light MXene aerogel/wood-derived porous carbon composites with wall-like "mortar/brick" structures for electromagnetic interference shielding. *Science Bulletin*, *65*(8), 616–622. https://doi.org/10.1016/j.scib.2020.02.009

Liao, D., Guan, Y., He, Y., Li, S., Wang, Y., Liu, H., Zhou, L., Wei, C., Yu, C., & Chen, Y. (2021). Pickering emulsion strategy for high compressive carbon aerogel as lightweight electromagnetic interference shielding material and flexible pressure sensor. *Ceramics International*, *47*(16), 23433–23443. https://doi.org/10.1016/j.ceramint.2021.05.059

Ling, J., Zhai, W., Feng, W., Shen, B., Zhang, J., & Zheng, W. G. (2013). Facile preparation of lightweight microcellular polyetherimide/graphene composite foams for electromagnetic interference shielding. *ACS Applied Materials and Interfaces*, *5*(7), 2677–2684. https://doi.org/10.1021/am303289m

Liu, C., Ye, S., & Jiachun Feng. (2016). The Preparation of Compressible and Fire-Resistant Sponge-Supported Re- duced Graphene Oxide Aerogel for Electromagnetic

Interference Shielding. *Chem. Asian J.*, *11*(18), 2586–2593. https://doi.org/http://dx.doi.org/10.1002/asia.201600905 A

Liu, J., Duan, Y., Song, L., Hu, J., & Zeng, Y. (2019). Heterogeneous nucleation promoting formation and enhancing microwave absorption properties in hierarchical sandwich-like polyaniline/graphene oxide induced by mechanical agitation. *Composites Science and Technology*, *182*(May), 107780. https://doi.org/10.1016/j.compscitech.2019.107780

Liu, X., Li, Y., Sun, X., Tang, W., Deng, G., Liu, Y., Song, Z., Yu, Y., Yu, R., Dai, L., & Shui, J. (2021). Off/on switchable smart electromagnetic interference shielding aerogel. *Matter*, *4*(5), 1735–1747. https://doi.org/10.1016/j.matt.2021.02.022

Londoño-Calderón, C. L., Vargas-Hernández, C., & Jurado, J. F. (2010). Desorption influence of water on structural, electrical properties and molecular order of vanadium pentoxide xerogel films. *Revista Mexicana de Fisica*, *56*(5), 411–415.

Lu, Z., Jia, F., Zhuo, L., Ning, D., Gao, K., & Xie, F. (2021). Micro-porous MXene/Aramid nanofibers hybrid aerogel with reversible compression and efficient EMI shielding performance. *Composites Part B: Engineering*, *217*(January), 108853. https://doi.org/10.1016/j.compositesb.2021.108853

Majid, I. (2018). EMI Effects in Flight Control Systems and Their Mitigations. *Handbook of Aerospace Electromagnetic Compatibility*, 537–602. https://doi.org/10.1002/9781119082880.ch10

Margoni, M. M., Mathuri, S., Ramamurthi, K., Babu, R. R., & Sethuraman, K. (2017). Sprayed vanadium pentoxide thin films: Influence of substrate temperature and role of HNO_3 on the structural, optical, morphological and electrical properties. *Applied Surface Science*, *418*, 280–290. https://doi.org/10.1016/j.apsusc.2017.02.039

Morávková, Z., & Dmitrieva, E. (2017). Structural changes in polyaniline near the middle oxidation peak studied by in situ Raman spectroelectrochemistry. *Journal of Raman Spectroscopy*, *48*(9), 1229–1234. https://doi.org/10.1002/jrs.5197

Mostafaei, A., & Zolriasatein, A. (2012). Synthesis and characterization of conducting polyaniline nanocomposites containing ZnO nanorods. *Progress in Natural Science: Materials International*, *22*(4), 273–280. https://doi.org/10.1016/j.pnsc.2012.07.002

Mukhtar, S., Liu, M., Han, J., & Gao, W. (2017). Removal of rhodamine B from aqueous solutions using vanadium pentoxide/titanium butyl oxide hybrid xerogels. *Chinese Physics B*, *26*(5), 058202. https://doi.org/10.1088/1674-1056/26/5/058202

Pandey, R., Tekumalla, S., & Gupta, M. (2019). Enhanced (X-band) microwave shielding properties of pure magnesium by addition of diamagnetic titanium micro-particulates.

Journal of Alloys and Compounds, *770*, 473–482. https://doi.org/10.1016/j.jallcom.2018.08.147

Pandit, B., Dubal, D. P., Gómez-Romero, P., Kale, B. B., & Sankapal, B. R. (2017). V_2O_5 encapsulated MWCNTs in 2D surface architecture: Complete solid-state bendable highly stabilized energy efficient supercapacitor device. *Scientific Reports*, *7*. https://doi.org/10.1038/srep43430

Paperman, W. D., David, Y., & Hibbetts, J. (2004). Electromagnetic interference in the hospital. In *Clinical Engineering Handbook*. Elsevier Inc. https://doi.org/10.1016/B978-012226570-9/50069-7

Park, K., Song, H., Kim, Y., Mho, S., Cho, W. Il, & Yeo, I. (2010). Electrochemical preparation and characterization of V_2O_5/polyaniline composite film cathodes for Li battery. *Electrochimica Acta*, *55*(27), 8023–8029. https://doi.org/10.1016/j.electacta.2009.12.047

Patil, S. H., Gaikwad, A. P., Sathaye, S. D., & Patil, K. R. (2018). To form layer by layer composite film in view of its application as supercapacitor electrode by exploiting the techniques of thin films formation just around the corner. *Electrochimica Acta*, *265*(March), 556–568. https://doi.org/10.1016/j.electacta.2018.01.165

Philipse, A. P., & Wierenga, A. M. (1998). On the density and structure formation in gels and clusters of colloidal rods and fibers. *Langmuir*, *14*(1), 49–54. https://doi.org/10.1021/la9703757

Powders, S. T. N., Ravikumar, R. V. S. S. N., Sundeep, D., Krishna, A. G., & Ephraim, S. D. (2016). Spectral Investigation of Structural and Optical Properties of Mechanically Synthesized TiO_2 -V_2O_5 Nanocomposite Powders. *Materials Today: Proceedings*, *3*(December), 31–38. https://doi.org/10.1016/j.matpr.2016.01.114

Purushothaman, K. K., Saravanakumar, B., Muralidharan, G., & Dhanashankar, M. (2017). Design of additive free 3D floral shaped V_2O_5@ Ni foam for high performance supercapacitors. *Materials Technology*, *32*(9), 584–590. https://doi.org/10.1080/10667857.2017.1311526

Puthiyedath Narayanan, A., Narayanan Unni, K. N., & Peethambharan Surendran, K. (2021). Aerogels of V_2O_5 nanowires reinforced by polyaniline for electromagnetic interference shielding. *Chemical Engineering Journal*, *408*(September 2020), 127239. https://doi.org/10.1016/j.cej.2020.127239

Rohom, A. B., Londhe, P. U., Mahapatra, S. K., Kulkarni, S. K., & Chaure, N. B. (2014). Electropolymerization of polyaniline thin films. *High Performance Polymers*, *26*(6), 641–646. https://doi.org/10.1177/0954008314538081

Ronquillo, M. L. T., Jacinto, P. S., Ovalle, P., Vázquez, L. R., Martínez, E. C., Marinero, E., & Garibay, V. (2016). Synthesis and Structural Characterization of Monocrystalline α-V_2O_5 Nanowires. *Materials Sciences and Applications*, *07*(09), 484–495. https://doi.org/10.4236/msa.2016.79042

Ryu, J., Suh, Y. W., Suh, D. J., & Ahn, D. J. (2010). Hydrothermal preparation of carbon microspheres from mono-saccharides and phenolic compounds. *Carbon*, *48*(7), 1990–1998. https://doi.org/10.1016/j.carbon.2010.02.006

Sacanna, S., & Pine, D. J. (2011). Shape-anisotropic colloids: Building blocks for complex assemblies. *Current Opinion in Colloid and Interface Science*, *16*(2), 96–105. https://doi.org/10.1016/j.cocis.2011.01.003

Sambyal, P., Iqbal, A., Hong, J., Kim, H., Kim, M. K., Hong, S. M., Han, M., Gogotsi, Y., & Koo, C. M. (2019). Ultralight and Mechanically Robust $Ti_3C_2T_x$ Hybrid Aerogel Reinforced by Carbon Nanotubes for Electromagnetic Interference Shielding. *ACS Applied Materials and Interfaces*, *11*(41), 38046–38054. https://doi.org/10.1021/acsami.9b12550

Sevilla, M., & Fuertes, A. B. (2009). The production of carbon materials by hydrothermal carbonization of cellulose. *Carbon*, *47*(9), 2281–2289. https://doi.org/10.1016/j.carbon.2009.04.026

Shen, B., Zhai, W., Tao, M., Ling, J., & Zheng, W. (2013). Lightweight, multifunctional polyetherimide/graphene@Fe_3O_4 composite foams for shielding of electromagnetic pollution. *ACS Applied Materials and Interfaces*, *5*(21), 11383–11391. https://doi.org/10.1021/am4036527

Singh, A. K., Shishkin, A., Koppel, T., & Gupta, N. (2018). A review of porous lightweight composite materials for electromagnetic interference shielding. *Composites Part B*, *149*, 188–197. https://doi.org/10.1016/j.compositesb.2018.05.027

Singh, A. K., Yadav, A. N., Srivastava, A., Haldar, K. K., Tomar, M., Alaferdov, A. V., Moshkalev, S. A., Gupta, V., & Singh, K. (2019). CdSe/V_2O_5 core/shell quantum dots decorated reduced graphene oxide nanocomposite for high-performance electromagnetic interference shielding application. *Nanotechnology*, *30*(50). https://doi.org/10.1088/1361-6528/ab4290

Song, P., Ma, Z., Qiu, H., Ru, Y., & Gu, J. (2022). High-Efficiency Electromagnetic Interference Shielding of rGO@FeNi/Epoxy Composites with Regular Honeycomb Structures. *Nano-Micro Letters*, *14*(1), 51. https://doi.org/10.1007/s40820-022-00798-5

Song, W. L., Guan, X. T., Fan, L. Z., Cao, W. Q., Wang, C. Y., & Cao, M. S. (2015). Tuning three-dimensional textures with graphene aerogels for ultra-light flexible

graphene/texture composites of effective electromagnetic shielding. *Carbon*, *93*, 151–160. https://doi.org/10.1016/j.carbon.2015.05.033

Stejskal, J., Prokeš, J., & Trchová, M. (2008). Reprotonation of polyaniline: A route to various conducting polymer materials. *Reactive and Functional Polymers*, *68*(9), 1355–1361. https://doi.org/10.1016/j.reactfunctpolym.2008.06.012

Stejskal, J., Trchová, M., Bober, P., Humpolíček, P., Kašpárková, V., Sapurina, I., Shishov, M. A., & Varga, M. (2015). Conducting Polymers: Polyaniline. In *Encyclopedia of Polymer Science and Technology* (Issue June, pp. 1–44). John Wiley & Sons, Inc. https://doi.org/10.1002/0471440264.pst640

Sun, W., Gao, G., Du, Y., Zhang, K., & Wu, G. (2018). A facile strategy for fabricating hierarchical nanocomposites of V_2O_5 nanowire arrays on a three-dimensional N-doped graphene aerogel with a synergistic effect for supercapacitors. *Journal of Materials Chemistry A*, *6*(21), 9938–9947. https://doi.org/10.1039/c8ta01448e

Sun, X., & Li, Y. (2004). Colloidal Carbon Spheres and Their Core/Shell Structures with Noble-Metal Nanoparticles. *Angewandte Chemie International Edition*, *43*(5), 597–601. https://doi.org/10.1002/anie.200352386

Sun, Y., Ma, L., Song, Y., Phule, A. D., Li, L., & Zhang, Z. X. (2021). Efficient natural rubber latex foam coated by rGO modified high density polyethylene for oil-water separation and electromagnetic shielding performance. *European Polymer Journal*, *147*(February), 110288. https://doi.org/10.1016/j.eurpolymj.2021.110288

Tan, K., & Hinberg, I. (2004). Electromagnetic Interference with Medical Devices: In Vitro Laboratory Studies and Electromagnetic Compatibility Standards. In *Clinical Engineering Handbook* (Issue Icd, pp. 254–262). Elsevier. https://doi.org/10.1016/B978-012226570-9/50068-5

Tong, X. C. (2008). *Advanced Materials and Design for Electromagnetic Interference Shielding* (1st ed.). CRC Press. https://doi.org/10.1201/9781420073591

Vanguard Products. (2022). *Why EMI Shielding Techniques Are Important for Smart Car Vehicles*. Vanguard Products Corporation. https://www.vanguardproducts.com

Vazhayal, L., Wilson, P., & Prabhakaran, K. (2020). Waste to wealth: Lightweight, mechanically strong and conductive carbon aerogels from waste tissue paper for electromagnetic shielding and CO_2 adsorption. *Chemical Engineering Journal*, *381*, 122628. https://doi.org/10.1016/j.cej.2019.122628

Waghmode, B. J., Soni, R., Patil, K. R., & Malkhede, D. D. (2017). Calixarene based nanocomposite materials for high-performance supercapacitor electrode. *New Journal of Chemistry*, *41*(18), 9752–9761. https://doi.org/10.1039/c7nj01125c

Wan, C., Jiao, Y., & Li, J. (2016). Influence of pre-gelation temperature on mechanical properties of cellulose aerogels based on a green NaOH/PEG solution—a comparative study. *Colloid and Polymer Science*, *294*(8), 1281–1287. https://doi.org/10.1007/s00396-016-3887-6

Wan, C., Jiao, Y., Li, X., Tian, W., Li, J., & Wu, Y. (2020). A multi-dimensional and level-by-level assembly strategy for constructing flexible and sandwich-type nanoheterostructures for high-performance electromagnetic interference shielding. *Nanoscale*, *12*(5), 3308–3316. https://doi.org/10.1039/c9nr09087h

Wan, C., & Li, J. (2016). Graphene oxide/cellulose aerogels nanocomposite: Preparation, pyrolysis, and application for electromagnetic interference shielding. *Carbohydrate Polymers*, *150*, 172–179. https://doi.org/10.1016/j.carbpol.2016.05.051

Wan, Y.-J., Zhu, P.-L., Yu, S.-H., Sun, R., Wong, C.-P., & Liao, W.-H. (2017). Ultralight, super-elastic and volume-preserving cellulose fiber/graphene aerogel for high-performance electromagnetic interference shielding. *Carbon*, *115*, 629–639. https://doi.org/10.1016/j.carbon.2017.01.054

Wan, Y.-J., Zhu, P.-L., Yu, S.-H., Sun, R., Wong, C.-P., & Liao, W.-H. (2018). Anticorrosive, Ultralight, and Flexible Carbon-Wrapped Metallic Nanowire Hybrid Sponges for Highly Efficient Electromagnetic Interference Shielding. *Small*, *14*(27), 1800534. https://doi.org/10.1002/smll.201800534

Wan, Y. J., Zhu, P. L., Yu, S. H., Sun, R., Wong, C. P., & Liao, W. H. (2017). Ultralight, super-elastic and volume-preserving cellulose fiber/graphene aerogel for high-performance electromagnetic interference shielding. *Carbon*, *115*, 629–639. https://doi.org/10.1016/j.carbon.2017.01.054

Wang, L., Ma, Z., Zhang, Y., Chen, L., Cao, D., & Gu, J. (2021). Polymer-based EMI shielding composites with 3D conductive networks: A mini-review. *SusMat*, *1*(3), 413–431. https://doi.org/10.1002/sus2.21

Wang, L., Ma, Z., Zhang, Y., Qiu, H., Ruan, K., & Gu, J. (2022). Mechanically strong and folding-endurance Ti3C2Tx MXene/PBO nanofiber films for efficient electromagnetic interference shielding and thermal management. *Carbon Energy*, *4*(2), 200–210. https://doi.org/10.1002/cey2.174

Wang, M., Tang, X. H., Cai, J. H., Wu, H., Shen, J. Bin, & Guo, S. Y. (2021). Construction, mechanism and prospective of conductive polymer composites with multiple interfaces for electromagnetic interference shielding: A review. *Carbon*, *177*, 377–402. https://doi.org/10.1016/j.carbon.2021.02.047

Wang, N., Zhang, Y., Hu, T., Zhao, Y., & Meng, C. (2015). Facile hydrothermal synthesis of ultrahigh-aspect-ratio V_2O_5 nanowires for high-performance

supercapacitors. *Current Applied Physics*, *15*(4), 493–498. https://doi.org/10.1016/j.cap.2015.01.026

Wang, X., Shu, J., Cao, W., Zhang, M., Yuan, J., & Cao, M. (2019). Eco-mimetic nanoarchitecture for green EMI shielding. *Chemical Engineering Journal*, *369*(December 2018), 1068–1077. https://doi.org/10.1016/j.cej.2019.03.164

Wang, Y., & Cao, G. (2006). Synthesis and enhanced intercalation properties of nanostructured vanadium oxides. *Chemistry of Materials*, *18*(12), 2787–2804. https://doi.org/10.1021/cm052765h

Wang, Y., Gao, X., Fu, Y., Wu, X., Wang, Q., Zhang, W., & Luo, C. (2019). Enhanced microwave absorption performances of polyaniline/graphene aerogel by covalent bonding. *Composites Part B: Engineering*, *169*(April), 221–228. https://doi.org/10.1016/j.compositesb.2019.04.008

Wang, Y., & Jing, X. (2005). Intrinsically conducting polymers for electromagnetic interference shielding. *Polymers for Advanced Technologies*, *16*(4), 344–351. https://doi.org/10.1002/pat.589

Wang, Y., Yang, C., Xin, Z., Luo, Y., Wang, B., Feng, X., Mao, Z., & Sui, X. (2022). Poly(lactic acid)/carbon nanotube composites with enhanced electrical conductivity via a two-step dispersion strategy. *Composites Communications*, *30*, 101087. https://doi.org/10.1016/j.coco.2022.101087

Wei, B., Zhang, L., & Yang, S. (2021). Polymer composites with expanded graphite network with superior thermal conductivity and electromagnetic interference shielding performance. *Chemical Engineering Journal*, *404*, 126437. https://doi.org/10.1016/j.cej.2020.126437

Wei, Q., Liu, J., Feng, W., Sheng, J., Tian, X., He, L., An, Q., & Mai, L. (2015). Hydrated vanadium pentoxide with superior sodium storage capacity. *Journal of Materials Chemistry A*, *3*(15), 8070–8075. https://doi.org/10.1039/c5ta00502g

Wu, C. G., DeGroot, D. C., Marcy, H. O., Schindler, J. L., Kannewurf, C. R., Liu, Y. J., Hirpo, W., & Kanatzidis, M. G. (1996). Redox intercalative polymerization of aniline in V_2O_5 xerogel. The postintercalative intralamellar polymer growth in polyaniline/metal oxide nanocomposites is facilitated by molecular oxygen. *Chemistry of Materials*, *8*(8), 1992–2004. https://doi.org/10.1021/cm9600236

Wu, X., Lyu, J., Hong, G., Liu, X. C., & Zhang, X. (2018). Inner Surface-Functionalized Graphene Aerogel Microgranules with Static Microwave Attenuation and Dynamic Infrared Shielding. *Langmuir*, *34*(30), 9004–9014. https://doi.org/10.1021/acs.langmuir.8b01410

Wu, X., Tao, Y., Dong, L., & Hong, J. (2003). Synthesis and characterization of self-assembling $(NH_4)_{0.5}V_2O_5$ nanowires. *Journal of Material Chemistry*, *14*, 901–904.

Xin, W., Ma, M. G., & Chen, F. (2021). Silicone-Coated MXene/Cellulose Nanofiber Aerogel Films with Photothermal and Joule Heating Performances for Electromagnetic Interference Shielding. *ACS Applied Nano Materials*, *4*(7), 7234–7243. https://doi.org/10.1021/acsanm.1c01185

Xing, C., Zhu, S., Ullah, Z., Pan, X., Wu, F., Zuo, X., Liu, J., Chen, M., Li, W., Li, Q., & Liu, L. (2019). Ultralight and flexible graphene foam coated with Bacillus subtilis as a highly efficient electromagnetic interference shielding film. *Applied Surface Science*, *491*(June), 616–623. https://doi.org/10.1016/j.apsusc.2019.06.107

Xiong, C., Aliev, A. E., Gnade, B., & Balkus, K. J. (2008). Fabrication of silver vanadium oxide and V_2O_5 nanowires for electrochromics. *ACS Nano*, *2*(2), 293–301. https://doi.org/10.1021/nn700261c

Yang, W., Shao, B., Liu, T., Zhang, Y., Huang, R., Chen, F., & Fu, Q. (2018). Robust and Mechanically and Electrically Self-Healing Hydrogel for Efficient Electromagnetic Interference Shielding. *ACS Applied Materials and Interfaces*, *10*(9), 8245–8257. https://doi.org/10.1021/acsami.7b18700

Yang, X., Fan, S., Li, Y., Guo, Y., Li, Y., Ruan, K., Zhang, S., Zhang, J., Kong, J., & Gu, J. (2020). Synchronously improved electromagnetic interference shielding and thermal conductivity for epoxy nanocomposites by constructing 3D copper nanowires/thermally annealed graphene aerogel framework. *Composites Part A: Applied Science and Manufacturing*, *128*, 105670. https://doi.org/10.1016/j.compositesa.2019.105670

Yang, Y., & Gupta, M. C. (2005). Novel Carbon Nanotube−Polystyrene Foam Composites for Electromagnetic Interference Shielding. *Nano Letters*, *5*(11), 2131–2134. https://doi.org/10.1021/nl051375r

Yang, Z. C., Wang, M., Yong, A. M., Wong, S. Y., Zhang, X. H., Tan, H., Chang, A. Y., Li, X., & Wang, J. (2011). Intrinsically fluorescent carbon dots with tunable emission derived from hydrothermal treatment of glucose in the presence of monopotassium phosphate. *Chemical Communications*, *47*(42), 11615–11617. https://doi.org/10.1039/c1cc14860e

Yu, W., Wang, T., Zhang, G., Wang, Z., Yin, H., Yan, D., Xu, J., & Li, Z. (2018). Largely enhanced mechanical property of segregated carbon nanotube/poly(vinylidene fluoride) composites with high electromagnetic interference shielding performance. *Composites Science and Technology*. https://doi.org/10.1016/j.compscitech.2018.08.013

Yu, Z., Dai, T., Yuan, S., Zou, H., & Liu, P. (2020). Electromagnetic Interference Shielding Performance of Anisotropic Polyimide/Graphene Composite Aerogels. *ACS Applied Materials & Interfaces*, *12*, 30990–31001. https://doi.org/10.1021/acsami.0c07122

Zeng, Z., Jin, H., Chen, M., Li, W., Zhou, L., & Zhang, Z. (2016). Lightweight and Anisotropic Porous MWCNT/WPU Composites for Ultrahigh Performance Electromagnetic Interference Shielding. *Advanced Functional Materials*, *26*(2), 303–310. https://doi.org/10.1002/adfm.201503579

Zeng, Z., Wang, C., Zhang, Y., Wang, P., Seyed Shahabadi, S. I., Pei, Y., Chen, M., & Lu, X. (2018). Ultralight and Highly Elastic Graphene/Lignin-Derived Carbon Nanocomposite Aerogels with Ultrahigh Electromagnetic Interference Shielding Performance. *ACS Applied Materials and Interfaces*, *10*(9), 8205–8213. https://doi.org/10.1021/acsami.7b19427

Zeng, Z., Wu, T., Han, D., Ren, Q., Siqueira, G., & Nyström, G. (2020). Ultralight, Flexible, and Biomimetic Nanocellulose/Silver Nanowire Aerogels for Electromagnetic Interference Shielding. *ACS Nano*, *14*(3), 2927–2938. https://doi.org/10.1021/acsnano.9b07452

Zhan, Y., Oliviero, M., Wang, J., Sorrentino, A., Buonocore, G. G., Sorrentino, L., Lavorgna, M., Xia, H., & Iannace, S. (2019). Enhancing the EMI shielding of natural rubber-based supercritical CO_2 foams by exploiting their porous morphology and CNT segregated networks. *Nanoscale*, *11*(3), 1011–1020. https://doi.org/10.1039/c8nr07351a

Zhang, H. Bin, Yan, Q., Zheng, W. G., He, Z., & Yu, Z. Z. (2011). Tough graphene-polymer microcellular foams for electromagnetic interference shielding. *ACS Applied Materials and Interfaces*, *3*(3), 918–924. https://doi.org/10.1021/am200021v

Zhang, D., Liu, T., Shu, J., Liang, S., Wang, X., Cheng, J., Wang, H., & Cao, M. (2019). Self-Assembly Construction of WS_2−rGO Architecture with Green EMI Shielding. *ACS Applied Materials & Interfaces*, *11*, 26807–26816. https://doi.org/10.1021/acsami.9b06509

Zhang, L., Liu, M., Roy, S., Chu, E. K., See, K. Y., & Hu, X. (2016). Phthalonitrile-Based Carbon Foam with High Specific Mechanical Strength and Superior Electromagnetic Interference Shielding Performance. *ACS Applied Materials and Interfaces*, *8*(11), 7422–7430. https://doi.org/10.1021/acsami.5b12072

Zhang, T., Zeng, S., Jiang, H., Li, Z., Bai, D., Li, Y., & Li, J. (2021). Leather Solid Waste/Poly(vinyl alcohol)/Polyaniline Aerogel with Mechanical Robustness, Flame Retardancy, and Enhanced Electromagnetic Interference Shielding. *ACS Applied Materials and Interfaces*, *13*(9), 11332–11343.

https://doi.org/10.1021/acsami.1c00880

Zhang, Y., Wen, G., Fan, S., Tang, X., Wang, D., & Ding, C. (2018). Partially reduced and nitrogen-doped graphene oxides with phenylethylamine for high-performance supercapacitors. *Journal of Materials Science*, *53*(16), 11715–11727. https://doi.org/10.1007/s10853-018-2471-5

Zhang, Y., Yu, J., Lu, J., Zhu, C., & Qi, D. (2021). Facile construction of 2D MXene ($Ti_3C_2T_x$) based aerogels with effective fire-resistance and electromagnetic interference shielding performance. *Journal of Alloys and Compounds*, *870*, 159442. https://doi.org/10.1016/j.jallcom.2021.159442

Zhang, Y., Zheng, J., Wang, Q., Zhang, S., Hu, T., & Meng, C. (2017). One-step hydrothermal preparation of $(NH_4)_2V_3O_8$ /carbon composites and conversion to porous V_2O_5 nanoparticles as supercapacitor electrode with excellent pseudocapacitive capability. *Applied Surface Science*, *423*, 728–742. https://doi.org/10.1016/j.apsusc.2017.06.249

Zhao, H. B., Yuan, L., Fu, Z. B., Wang, C. Y., Yang, X., Zhu, J. Y., Qu, J., Chen, H. B., & Schiraldi, D. A. (2016). Biomass-Based Mechanically Strong and Electrically Conductive Polymer Aerogels and Their Application for Supercapacitors. *ACS Applied Materials and Interfaces*, *8*(15), 9917–9924. https://doi.org/10.1021/acsami.6b00510

Zhao, H., Hou, L., Bi, S., & Lu, Y. (2017). Enhanced X - Band Electromagnetic-Interference Shielding Performance of Layer-Structured Fabric-Supported Polyaniline / Cobalt − Nickel Coatings. *ACS Appl. Mater. Interfaces*, *9*, 33059−33070. https://doi.org/10.1021/acsami.7b07941

Zhou, B., Han, G., Zhang, Z., Li, Z., Feng, Y., Ma, J., Liu, C., & Shen, C. (2021). Aramid nanofiber-derived carbon aerogel film with skin-core structure for high electromagnetic interference shielding and solar-thermal conversion. *Carbon*, *184*, 562–570. https://doi.org/10.1016/j.carbon.2021.08.067

Zhou, K., He, Y., Xu, Q., Lu, Z., Yang, L., Jiang, Y., Ge, D., Liu, X. Y., & Bai, H. (2018). A Hydrogel of Ultrathin Pure Polyaniline Nano fibers: Oxidant-Templating Preparation and Supercapacitor Application. *ACS Nano*, *12*(6), 5888–5894. https://doi.org/10.1021/acsnano.8b02055

Zhou, X., Wu, G., Wu, J., Yang, H., Wang, J., Gao, G., Cai, R., & Yan, Q. (2013). Multiwalled carbon nanotubes-V_2O_5 integrated composite with nanosized architecture as a cathode material for high performance lithium ion batteries. *Journal of Materials Chemistry A*, *1*(48), 15459–15468. https://doi.org/10.1039/c3ta13143b

Zhou, Z., Liu, J., Zhang, X., Tian, D., Zhan, Z., & Lu, C. (2019). Ultrathin

MXene/Calcium Alginate Aerogel Film for High-Performance Electromagnetic Interference Shielding. *Advanced Materials Interfaces*, *6*(6), 1–9. https://doi.org/10.1002/admi.201802040

Zhu, M., Yan, X., Xu, H., Xu, Y., & Kong, L. (2021). Ultralight, compressible, and anisotropic MXene@Wood nanocomposite aerogel with excellent electromagnetic wave shielding and absorbing properties at different directions. *Carbon*, *182*, 806–814. https://doi.org/10.1016/j.carbon.2021.06.054